SPRAY VISUALIZATION AND CHARACTERIZATION OF A MULTI VARIABLE CIRCULAR ORIFICE (MVCO) INJECTOR COUPLED WITH A SWIRL ADAPTER FOR DIESEL REFORMER APPLICATIONS

BY

KARTHIK NITHYANANDAN

THESIS

Submitted in partial fulfillment of the requirements
for the degree of Master of Science in Mechanical Engineering
in the Graduate College of the
University of Illinois at Urbana-Champaign, 2012

Urbana, Illinois

Adviser:

Professor Chia-Fon Lee

Abstract

The fuel spray generated by the injector is of primary importance to mixing and hence, combustion efficiency, due to the extremely short time scale of the combustion event inside an internal combustion engine. In this respect, the aim of the fuel injection system is to atomize the fuel droplets as fine as possible in order to provide a homogeneous mixture before combustion initiates.

Spray visualization and characterization of a Micro-Variable Circular-Orifice (MVCO) fuel injector coupled with a swirl-producing adapter was studied. The spray characteristics such as spray penetration length, spray velocity etc. and the atomization performance were evaluated. The measurement was conducted on an engine facility where diesel fuel was delivered by a high pressure pump coupled with a common rail. Various injection pressures ranging from 300 bar to 700 bar were tested while the back pressure was kept at 1 bar. Compressed air at pressures of 30 psi and 60 psi were supplied to the swirl adapter. High speed Mie scattering images were recorded using a High speed camera to document the spray evolution. Images were acquired from both the front view and the bottom view. Phase Doppler Anemometry (PDA) measurement was conducted at different locations in the spray for the acquisition of droplets size and velocity distribution. Difficulties in measurements were encountered for high pressure injection, especially in the central part of the spray jet and near the nozzle exit region owing to the strong attenuation of the incident laser beams and the scattered light.

Unlike traditional injectors which normally inject six fuel jets, the MVCO fuel injector presented a unique spray pattern by injecting more than twenty jets in an approximately axi-symmetric fashion. Due to the interaction between the spray jets, the breakup was much

enhanced relative to conventional injectors, causing shorter spray tip penetration, finer droplet size and wider fuel droplets distribution. It is seen that distributions peaks lie at about 5-10 μm mainly due to the more violent breakup induced by the unique spray pattern of the MVCO. No apparent trend of the droplet size against injection pressure is observed which is desirable for engine optimization according to engine load. Note that the injection duration was kept constant, thus the injection pressure can be viewed as a reasonable representative of the engine load. At low load condition, the spray is characterized by a relatively narrow spray angle and shorter penetration so as to prevent wall wetting while at high load, the spray was widened to suit for higher power output.

High speed images obtained for the MVCO injector coupled with the swirl adapter showed that the adapter caused the fuel spray to become wider. A higher degree of atomization was also achieved. PDA results displayed a clear rotational motion indicating a strong swirl being imparted to the fuel spray by the adapter. Such swirl flow can only further improve the mixing process for the MVCO as the turbulent kinetic energy delivered by the intake flow will induce the more violent breakup leading to finer droplets. Therefore a highly atomized spray with high level of mixing (swirl) was obtained which could potentially increase diesel reformer efficiency.

Acknowledgements

First and foremost, I want to thank my research advisor/ mentor, Professor Chia-Fon Lee, for giving me this wonderful opportunity to pursue research under his guidance. I came to the University of Illinois with a dream to work with him, and I thank him for making that dream a reality. His continuous encouragement and relentless support in this research project was invaluable. His constructive advice and insightful guidance have been of tremendous help to my study at the University. I would also like to thank Prof. Alan C. Hansen for all his help and guidance during the course of my Masters.

Special thanks goes to Ming Huo, who helped me set up the experiment, taught me the proper ways of conducting experiments and continued to offer me help even when he was busy with his own research. He has been an inspiration to me to excel in research, and also a very good friend.

Hearty appreciation is given to my friends Hari Raghavendra and Manasa Harini Arcot. They have always been there for me when things weren't going too well. They made my life outside the lab very enjoyable.

Finally, I want to thank my parents, Mr. R. Nithyanandan and Mrs. Jayanthi Nithyanandan for their unquestioning support in my study. I also wish to thank my sisters Kavitha Nithyanandan and Pallavi Nithyanandan for always looking out for my best interests. Without my family, I would not be where I am.

Table of Contents

Page

List of Tables

List of Figures

Chapter 1

Introduction

Fuel cell based auxiliary power units (APUs) have been developed to combat the adverse impacts of fuel consumption, emissions, and noise pollution during idling of vehicles. A commercially viable fuel cell APU system would require the use of existing infrastructure fuels, such as gasoline or diesel; therefore a fuel cell integrated with a fuel processor is an attractive alternative to a pure hydrogen system. For low-temperature PEM fuel cell systems, costly purification technology must be employed to remove CO from the hydrogen feed stream. And solid oxide fuel cells face challenges associated with thermal cycles and startup time requirements. The quicker response, the shorter start-up time, along with the higher stability of cell material and lower cost of the PEFC unit, compared to SOFC, are believed to be winning features making it a more attractive solution for a FC-APU utility onboard heavy-duty diesel trucks. The fuel reformer can be described as the "heart" of the FC-APU.

Diesel fuel is widely distributed and has high energy density, which makes diesel reforming an attractive option for hydrogen production on-board vehicles. Diesel reforming has received increasing attentions recently because on one hand, hydrogen fed fuel cell power unit as external power supply offers a promising alternative to compression engines to reduce idling emissions, on the other hand, intake air mixed with syngas is postulated to enhance the gas and diesel combustion efficiency and reduce emission.

The main work in diesel reforming is done through heterogeneous reactions which involve reactions between gaseous diesel and solid catalysts with the aim to produce a hydrogen-rich gas. Hence, in a diesel PEFC-APU system, the injection system is critical to the atomization and

vaporization of the liquid fuel in order to facilitate the heterogeneous reactions. In diesel reforming, different reforming technologies can be employed in which diesel is blended with air, pure oxygen or steam as main reactant. The gas mixture has to be well-blended to avoid local variations, e.g. air/fuel ratios, in order to prevent hot-spots that can cause undesired side reactions such as carbon formation and damage the catalyst.

The MVCO injector coupled with the swirl adapter would inject fuel at relatively high pressures close to 300 bar, but yet have a much lower jet penetration compared to the traditional injectors, and hence solve the problem of wall-wetting. Also, the MVCO injector produces a mist-like spray with an SMD that is nearly half that of the traditional injector at half the axial distance.

Chapter 2

Literature Review & Theory

2.1 U.S.A Transport Sector – Idling Issues

The entire transport sector of the US is more than 97% dependent on petroleum-based fuels and consumes approximately two-thirds of the nation's oil demand. Largely due to the popularity of vans, trucks, and sport utility vehicles, the average fleet efficiency for new cars and trucks has been declining since 1987. This situation, coupled with increases in population, in the number of vehicles used, and in per-capita miles driven, has propelled US petroleum consumption upward. The US now consumes more petroleum for highway transport purposes than is produced domestically; the gap is expected to grow significantly over the next 20 years. In 1997, about 51% of the total US petroleum consumption by all sectors was met by imports, contributing US$69 billion (38%) of the nation's merchandise trade deficit. The Energy Information Agency (EIA) forecasts that by 2020, imported petroleum will account for 73% of the total domestic petroleum consumption by all sectors at a cost to the nation of nearly US$95 billion. There is also continuing concern by many in the US health and environmental sectors about the poor air quality in metropolitan areas and the increasing levels of greenhouse gases in the atmosphere. In 1998, the United States Environmental Protection Agency (EPA) estimated that in the US over 113 million people lived in areas not meeting National Ambient Air Quality Standards. The transport sector contributes heavily to non-attainment in many of these areas. Additionally, increasing levels of carbon dioxide (CO) and other greenhouse gas emissions are becoming a global issue. Atmospheric concentrations of CO are now 32% higher than they were 150 years ago at the onset of the Industrial Revolution (circa 1850). In the US, the transport

sector account for one-third of CO emissions, and over the next 20 years is projected to become the leading carbon emitter. Clearly, to meet these energy and environmental challenges, breakthroughs in transport technologies are required [1].

It is believed that fuel cells will be one of the main energy conversion systems of the future. Fuel cells have higher energy conversion efficiencies and lower amounts of emission gases than internal combustion engines. Hydrogen can be converted at a very high electrochemical efficiency and emits only water as a by-product. However, there is, at present, lack of a hydrogen production infrastructure. There are two main ways to produce hydrogen: one is by the electrolysis of water, the other is by reforming of fossil fuels, such as natural gas, gasoline and diesel. It has been suggested that fuel reforming is the more practical method due to its high-energy efficiency. Diesel has been chosen as the reformate fuel because of its high gravimetric and volumetric hydrogen density and a well-established delivery infrastructure [2].

Drivers of long-haul trucks regularly rest in their truck cabs and idle their engines when doing so. The truck cabs, equipped with climate control devices and a wide assortment of accessories, serve as functional homes for drivers for most of the year. To power in-cab electric appliances and maintain cab climate in seasonal weather, a truck's main propulsion engine is utilized. These large engines are designed for highway freight-hauling situations. They operate very inefficiently when idling. The implications of this truck idling are significant. Analysis of the US Department of Commerce's Vehicle Inventory and Use Survey indicates that approximately 400,000 long-haul Class 7 and 8 trucks routinely travel over 500 miles from their home base, consuming approximately 685 million gallons of diesel fuel per year during overnight idling [3]. Assuming a higher vehicle population of 500,000 long-haul vehicles, emissions during overnight idling have been estimated to be 10.9 million tons of carbon dioxide

(CO2) and 190,000 tons of oxides of nitrogen annually [4]. Many regional air quality agencies around the United States have already begun to regulate idling, and the Bush Administration's national energy program has targeted heavy-duty truck idling. Heavy-duty truck idling is not just an energy and environmental concern, though. Vehicle idling also represents a fuel cost to operators and accelerates engine wear and tear, shortening engine life and increasing maintenance costs. In cases where idling interferes with driver rest, it presents a safety concern.

Several technical solutions to supplant idling are currently available, and others are in development. Add-on diesel-fired heaters, cooling systems, diesel auxiliary power units (APUs), and generators are commercially available. However, the market penetration of these technologies has been limited. An increasing number of new trucks are being manufactured to be compatible with electrification (or ''shore power''), in which trucks at truck stops and rest areas are connected to the electric grid and sometimes to other services, such as the Internet. This technology is receiving a great deal of attention in part because it is commercially available and relatively straightforward to fund, given that it generates benefits in a specific state or region. However, only a portion of idling is conducted at truck stops, and the vehicles that idle the most are likely to idle in diverse locations. A third option, fuel cell APUs, which we investigate here, are portable power sources similar to the current diesel-powered APUs and generators. These APUs would likely be targeted at the large market segment that does not stop exclusively at truck stops and other places with electrical power. Fuel cell APUs supply on-board power to replace the idling of the main engine. These fuel cells can most readily be made to operate on reformed diesel fuel. With modest economic incentives from government and continuing fuel cell technology improvements, APUs might be economically feasible for up to 15% of the long-haul truck population (60,000 trucks) in the United States in the 2015 time

frame, resulting in a 30% reduction of heavy-duty truck fuel use during overnight idling and a 40% reduction in oxides of nitrogen (NOx) produced during idling [5].

2.2 Syngas

The combustion of synthesis gas will play an important role in advanced power systems based on the gasification of fuel feedstocks and combined cycle power production. While the most commonly discussed option is to burn syngas in gas turbine engines, another possibility is to burn the syngas in stationary reciprocating engines. Whether spark ignited or compression ignited, syngas could serve to power large bore stationary engines, such as those presently operated on natural gas. One area that has received attention is dual-fueled diesel combustion, using a combination of diesel pilot injection and syngas fumigation in the intake air

Advanced power systems that are projected to achieve high efficiency and low emissions, such as those envisioned in the ‘‘Vision 21’’ [4, 5] and ‘‘FutureGen’’ programs of the U.S. Department of Energy, rely on synthesis gas as a key intermediate energy carrier. In such systems, coal or other fuels are converted to synthesis gas (composed mostly of hydrogen and carbon monoxide) via gasification and/or partial oxidation. Because of their role in distributed energy (DE) production and their combination of high efficiency and low cost, advanced reciprocating engines are another potential means of converting synthesis gas into power. Mixtures of hydrogen and carbon monoxide have high anti-knock behavior and therefore could serve as spark ignition (SI) fuels and as HCCI fuels [6]. However, addition of hydrogen to carbon monoxide or to methane tends to increase combustion temperatures and increases NO emissions under stoichiometric SI combustion. So, such mixtures may be more appropriate in lean burn applications where combustion temperatures are moderated by excess air. Such

mixtures could also serve in ‘‘dual-fuel’’ engines that operate under compression ignition using a pilot injection of diesel fuel. Although there is little published work on the use of synthesis gas as a fuel for internal combustion engines, there has been a substantial effort by Le Corre and co-workers [6] on the use of various gaseous fuels, including synthesis gas, in dual-fuel compression ignition engines. This work is one example of the large body of activity on pilot-ignited dual-fuel diesel engines that operate on a combination of diesel fuel and natural gas. In the work by McMillian and Lawson [6, 7], a spark ignited engine was operated at equivalence ratios from 1.3 to 1.6 and was shown to yield H2 concentrations as high as 11 vol.% in a spark ignition mode. They estimated that hydrogen concentrations as high as 20 vol.% could be achievable by operating in a homogeneous charge compression ignition (HCCI) operating mode.

Dual-fuel engines have been employed in a wide range of applications to utilize gaseous fuels. They are most commonly modified diesel engines and can achieve very low emission levels, particularly smoke and particulate. Benefits with the dual-fuel conversion include smoother and quieter operation, significantly longer engine life between overhauls, fuel savings and enhanced safety. The gaseous fuel, which is called the primary fuel, provides most of the energy input. This is inducted along with air and compressed. At full load around 80% of the total energy could be contributed by the primary fuel. The pilot fuel is usually diesel, and in fact, is used to ignite the gaseous fuel-air charge. The injection of the pilot fuel takes place near TDC (Top Dead Center) like in the diesel engine. The pilot fuel self-ignites and forms multiple ignition centers from which primary fuel combustion is initiated. Finally, the gaseous fuel and the pilot fuel burn together in the combustion chamber. The combustion process in a dual-fuel engine tends to display a combination of features of both diesel and spark ignition engines. For compression ignition (CI) engines, the ignition of the primary fuel (i.e., which is typically the

gaseous fuel in dual-fuel CI combustion) is activated by the in-cylinder conditions. Some fuels do not have good enough ignition quality to enable ignition. Therefore, two fuels must be used. First a pilot fuel, which could be for example diesel fuel, is injected, resulting in ignition and a rise of the temperature in the combustion chamber. Then, the second fuel, which could be for example syngas, is injected and ignites as the pilot fuel temperature increases. In dual-fuel engines, the energy released by combustion comes about partly from the combustion of gaseous alternative fuel, while the diesel fuel continues to provide, through timed cylinder injection, the remaining part of the energy released.

Ideally, in relation to the gaseous alternative supplied to the engine, there is a need to determine the optimum diesel fuel quantity at a particular engine operating condition, so as to provide the best performance over the desired load range. The main aim is to minimize the use of diesel fuel due to environmental considerations and maximize its substitution by alternative fuels throughout the load and speed range. The dual-fuel engine is an ideal multi-fuel engine that can operate effectively on a wide range of fuels with the flexibility of operating as a conventional diesel engine. The typical combustion process in a dual-fuel engine consists of four stages, an ignition delay period, premixed combustion of the pilot fuel, premixed combustion of the gaseous fuel and diffusion combustion of the gaseous fuel together with the combustion of the remaining pilot fuel. Of interest is the determination of the ignition delay, which is the time delay between injection of the pilot fuel and the initiation of chemical heat release, and correlation of the ignition delay for various fuel combinations. During this ignition delay period, complex chemical reactions take place.

Syngas addition (i.e., substitution of syngas for diesel fuel) tends to shorten the ignition delay and shorten the duration of combustion in dual-fuel operation. Syngas addition tends to increase

NOx emissions, presumably from the increase of adiabatic flame temperature due to the hydrogen in the syngas. Based upon observations of hydrogen assisted CI combustion, modest amounts of syngas addition in combination with advanced injection timing of the diesel pilot can lead to effective low temperature ‘‘PCCI’’ combustion, yielding both reduced PM and reduced NOx [6].

Automobiles have become the major source of air pollution in large cities. Even the best car manufacturers have not yet achieved satisfactory specific fuel rate and exhaust gas toxicity levels. This leads to constantly toughening environmental norms on hazardous emissions and hence stimulates work on the improvement of spark internal combustion engines or the development of gaseous fuels. Hazardous release is traditionally reduced by mounting expensive three-way catalytic converters based on platinides in the exhaust system of vehicles.

The converters provide the afterburning of carbon monoxide and hydrocarbon residue and reduce the nitrogen oxide concentrations to the standard norms in the exhaust gases. The problem of reducing CO2 emissions, however, is not solved, while the cost of the car increases and the engine efficiency decreases. In other words, the conventional approach to the reduction of hazardous exhaust is aimed at controlling the consequences of the disadvantages of fuel combustion in engines. As is known, the automotive ICE operates for a long time at low and medium load with fuel over-burning and a considerable release of toxic combustion products under urban conditions. For a car with a power rating of 50–100 kW, the mean power used under urban conditions is up to 10 kW, and the real efficiency of the engine is no more than 15% instead of 30% at power rating. Using a lean fuel mixture in the urban cycle of driving can thus considerably save the hydrocarbon fuel and hence reduce the carbon dioxide release, simultaneously improving the environmental characteristics of ICE. The major challenge is then

to ensure stable engine operation without a substantial loss in power. A highly reactive hydrogen additive to lean fuel mixtures in ICE could provide a solution and the most reasonable approach to the problem of raising the efficiency of ICEs with spark ignition. Direct use of cylinder hydrogen in popular vehicles, however, is limited by the lack of necessary infrastructure for hydrogen refueling, in addition to the obvious inconvenience of using two types of fuel on board a vehicle. It is more practicable, therefore, to obtain a hydrogen-containing gas from the main fuel directly on board a car during operation of the engine. The simplest way of doing this is obtaining syngas (a hydrogen–carbon monoxide mixture) by catalytic conversion of some part of main fuel. An on-board generator of a hydrogen-containing gas offers all advantages of using hydrogen during the combustion of lean fuel mixtures and simultaneously reduces the hydrogen explosion risk. The idea of using hydrogen additives to fuel mixtures is not new. Extensive studies were carried out on hydrogen ICEs in the Soviet Union in the 1980s. It was concluded that using hydrogen combined with conventional motor fuels in car engines was a promising approach. The disadvantages were found to be hydrogen storage problems, safety while handling hydrogen, and problems in mixing hydrogen with main fuel. These problems remained unsolved and annihilated the plans for using hydrogen as a component of fuel for ICEs. Chevrolet tests in the United States in 1973–1975 (the operating volume of engine 5.75 l, the engine additionally equipped with a syngas generator) showed the possibility of a 26% reduction in gasoline consumption in driving under the conditions of the CVS-3 Federal driving cycle. This development, however, was not used nationwide because of the low resource of used catalysts for syngas production, prolonged startover of the on-board generator, and high NO*x* concentration during fuel combustion with large amounts of hydrogen additive. More recently, studies were intermittently undertaken on different versions of hydrogen use as an additive to

main fuel for ICEs. The results showed that hydrogen additions, e.g., to the natural gas in amounts of up to 20 vol %, reduced the CO, CH, and NO*x* emissions in the exhaust gases of spark ICEs, but simultaneously decreased the thermal efficiency of the engine because of the lower energy bulk density of hydrogen. An increase in hydrogen additions leads to increased formation of nitrogen oxides and gives rise to critical phenomena like backfire of hydrogen-containing fuel, which can be suppressed by recycling the exhaust gases. It became evident that using lean fuel mixtures with a variable composition in spark ICEs demands optimization of combustion processes, which is a rather complex problem in itself, demanding new technological approaches. These problems obviously daunted these promising studies, which halted at the stage of laboratory and bench tests. Effective use of hydrogen-containing gas as an additive to main fuel in ICEs is thus directly related to a set of scientific and technological problems. These primarily include the development of new types of monolith structured catalysts for the conversion of hydrocarbon fuels to syngas; development of compact on-board syngas generators mounted under the motor hood and providing the minimum generator startover time; development of a on-board syngas generator control system adapted to the engine control system; solving the technological problems of implementation of optimum syngas generator and ICE control; performing the complete set of necessary laboratory, bench, and driving tests; and assessing prospects for the use of the given technology for creating energy effective and ecologically clean internal combustion engines.

Kirilliv et. al. [7] showed that using syngas additives to both gasoline and natural gas ensures highly economic operation of ICEs with spark ignition when lean fuel mixtures are used, including those with recycling of exhaust gases. This leads to fuel saving and a considerable reduction of toxic exhaust. Using on-board generators of hydrogen-containing gases allows one

to avoid the creation of hydrogen refueling and a multitude of expenses for the creation of the widely debated infrastructure of centralized production, storage, and transportation of hydrogen.

Furthermore, using on-board SGGs will radically improve the situation with safety of hydrogen-consuming vehicles, because hydrogen is produced in small amounts directly at the site of its consumption and is used without intermediate accumulation and storage. The ICE startover conditions in winter time are considerably improved due to the preliminary startover of the on-board SGG and subsequent integrated action of warmed heat carrier and hydrogen-containing fuel. The possibility of producing syngas from diesel and biodiesel fuels, bioethanol, and other types of biofuel (obtained from plant biomass) opens up new possibilities for using the given technology for ICEs as additives to fuel and reducing media generator required for neutralization of nitrogen oxides in the ICE exhaust [7].

2.3 Diesel Reforming

Diesel and jet fuel are potential candidates as hydrogen carriers for fuel cells in these auxiliary power units (APUs). The high energy density and existing infrastructure of the fuels make them a viable energy source for APUs. Catalytic onboard reforming technologies are considered feasible alternatives for supplying APUs with hydrogen. Auto-thermal reforming (ATR) has received much attention lately as one of the most promising methods for generating hydrogen from heavy hydrocarbon fuels.

ATR, a thermo-neutral process (Eq. (1)), which uses air and water vapor as reactants, has several benefits in onboard reforming for mobile fuel cell applications. This is due to its high thermal efficiency (~60–75%) and dynamics during transient operation as well as the low system complexity it offers; e.g. after start-up no external heating or cooling is needed on the

ATR reactor to sustain the thermo-neutral process during operation [13]. A general reaction formula for ATR, assuming that the products (reformate) are only CO2 and H2, can be expressed as follows:

$$C_nH_m + x\,(O_2 + 3.76N_2) + (2n - 2x)\,H_2O \rightarrow nCO_2 + (2n - 2x + m/2)\,H_2 + x3.76N_2 \quad \text{(Eq. 1)}$$

For ATR, the reforming reactor design and the reforming catalyst employed are two critical factors that can determine the product gas distribution. On one hand, the proper selection of catalyst can significantly affect the hydrogen conversion rate, reformer life and cost, etc., and on the other hand, the optimal reactor design, i.e. the injection system design, is essential to ensure complete fuel conversion, maximum hydrogen selectivity, and low amounts of carbon monoxide.

Diesel reforming poses several technical challenges. First of all, diesel fuel is prone to pyrolysis upon vaporization; meanwhile, the atomization of the diesel fuel from direct fuel injection can also be crucial as poor atomization could cause slow reforming kinetics as well as catalyst deactivation. Secondly, unconverted hydrocarbons and high amounts of CO are generally not desirable in APU systems as the molecules can contaminate gas purification devices and also lead to performance losses on the fuel cells, particularly for low-temperature polymer electrolyte fuel cells (PEFCs) [13]. Lastly, water availability for transportation APU is limited though the content of which could significantly affect the carbon formation. Among these issues, the fuel atomization is the main focus of this study as in a diesel reformer, the mixing of fuel with air and steam should be as thorough, uniform as possible prior to reaching the catalyst bed in order to minimize the hot spot and coke formation. Reformer catalysts suffer degradation due to the build-up of carbon deposits and inadequate feed mixing and vaporization, which cause

non-uniform temperature distributions within the reformer reactor. A fuel injector system that fully vaporizes and mixes the reactants, thus resulting in a uniform flow field impinging upon the catalytic bed, is critical to achieve optimal reforming performance.

There are great differences between diesel employment for compression engines and diesel usage in fuel reforming. In the case of the compression engine, the fuel is injected at high pressures, ~2 000 bar, blended with air and compressed to ignite in order to make use of the chemical energy for vehicle propulsion. The main work in the compression engine is done mechanically using a piston. In diesel reforming, no mechanical work is carried out. Instead, the main work is done through heterogeneous reactions which involve reactions between gaseous diesel and solid catalysts with the aim to produce a hydrogen-rich gas. Hence, in a diesel PEFC-APU system, the injection system is critical to the atomization and vaporization of the liquid fuel in order to facilitate the formation of a homogeneous mixture.

In diesel reformer, the fuel is usually injected at low pressures of around 7-10 bar [14]. According to Karatzas, too high pressures may result in large build-ups of unconverted liquid fuel on the catalyst surface which can cause mechanical damages to the catalyst, disturbance in the flow pattern and reactor plugging. Too low pressure causes incomplete reaction with the catalyst and hence the formation of soot and coke deposits. Hence, finding fuel injectors suitable for diesel reforming with excellent fuel dispersion capabilities that operate at low pressures and volumetric flows can be tricky. In addition, the mixture preparation is a crucial step in reforming. In diesel reforming, different reforming technologies can be employed in which diesel is blended with air, pure oxygen or steam as main reactant. The gas mixture has to be well-blended to avoid local variations, e.g. air/fuel ratios, in order to prevent hot-spots that can cause undesired side reactions such as carbon formation and damage the catalyst.

2.4 Micro-Variable Circular Orifice (MVCO)

Automakers are facing significant challenges to meet stringent government regulations for emissions and fuel efficiency. While low temperature combustion and/or premixed charge compression ignition (PCCI) combustion reduces engine-out NOx and soot simultaneously, the conventional multi-hole injector limits operation ranges of PCCI. One major reason is due to the fixed injection spray angle which may cause wall wetting for early injections. Currently PCCI can only operate in low to medium loads, conventional fixed-spray-angle nozzles have to be compromised for low load PCCI and high load conventional combustion. A larger spray angle for high loads will bring severe wall wetting and oil dilution for early and late injections. A fixed narrow spray angle optimized for low load PCCI usually generates more soot for high load combustion. Fixed spray angle is hard to be adaptive for the moving combustion chamber geometry at different injection timings. The successful development of MVCO technology will provide much needed flexibility for mixed-mode combustion. An illustration of MVCO nozzle is shown in Figure 2.1.

The micro-variable circular orifice (MVCO) fuel injector provides variable spray angles, variable orifice areas, and variable spray patterns. The MVCO provides optimized spray patterns to minimize combustion chamber surface-wetting, oil dilution and emissions. Designed with a concise structure, MVCO can significantly extend the operation maps of high efficiency early HCCI/PCCI combustion, and enable optimization of a dual-mode HCCI/PCCI and Accelerated Diffusion Combustion (ADC) over full engine operating maps [9].

The new MVCO can significantly reduce emissions and enhance engine efficiency through following means:

(1) Providing flexible spray angles and spray patterns to match moving combustion chamber geometry and in-cylinder conditions at different injection timings, simultaneously reduce soot, NOx, HC and CO;

(2) Provide variable orifice exit areas for different engine loads and injection timings;

(3) Enabling low temperature premixed combustion with homogeneous atomization;

(4) Enabling dual-mode early PCCI-ADC combustion through adaptive spray patterns.

The MVCO injector thus has a great potential to be used for diesel reformer applications due to its unique spray characteristics. High pressures may be used in this injector which will greatly help in atomizing and vaporizing the diesel fuel and prevent wetting of the catalyst. The MVCO injector coupled with the swirl adapter would inject fuel at relatively high pressures close to 300 bar, but yet have a much lower jet penetration compared to the traditional injectors, and hence solve the problem of wall-wetting. Also, the MVCO injector produces a mist-like spray with an SMD that is nearly half that of the traditional injector at half the axial distance.

2.5 Swirl Flow For Air/Fuel Mixing

It is a well-known fact that the efficiency of combustion relies heavily on the quality of air/fuel mixture and greatly influences overall engine performance as well as pollutant emission. The ideal situation would be to ensure that all the injected fuel is in contact with the maximum amount of available oxygen, resulting in complete combustion of the hydrocarbons, and avoiding high local fuel concentrations. It can consequently be stated that the main objective of injection is for the spray to come into contact with as much fresh air as possible. This means that through its own turbulence the spray should entrain as much air as possible and the droplets should be as

small as possible in order to maximize the contact surface between fuel and air and thus promote evaporation. Throughout the literature, numerous studies can be found that have achieved theoretical predictions of the main defining parameters of the spray: tip penetration, cone angle, and droplet size [22]. However, the results vary between different injection systems and conditions, and the conclusions that can be drawn are rather qualitative, although it can be argued that the laws of penetration are quite well understood at present. It is generally acknowledged that the flow turbulence inside the orifice is one of the main factors that enhance the spray to break up into droplets, as well as increase the interaction between the spray and its ambient surroundings. The flow characteristics are in turn, influenced by the injection pressure, and consequently its variations during the injection process, as well as the injector geometry [23].

Swirl flow is commonly used in high-pressure common rail fuel injection equipment, and premixed charged compression ignition type systems as a potential means of promoting mixing efficiency [17]. For instance, small high-speed DI diesel engines often have a lack of time for the fuel to be adequately mixed with air in the combustion chamber. The insufficient mixing time gives rise to an increase in poisonous emissions (e.g., soot). Although a reduction in size and increasing speed are highly desirable for improving engine power, an increase in harmful particulate matter (PM) emissions is not acceptable.

Swirling flows can also improve and control the mixing process between fuel and oxidizer streams to achieve flame stabilization and heat release rate enhancement. The key to attain homogeneity of fuel/air mixture and consequently low NOx emission, is chiefly dependent on the swirling flow field which governs the main flow structure and its matchup with fuel distribution. Multiple swirlers with distributed fuel injection system characterize modern gas

turbine combustors. The rotating direction of multiple swirlers has a large effect on the size, shape and strength of recirculation zone and turbulence intensity, and hence it has significant effects on the mixing process, temperature pattern and exhaust gas emission. Merkle et al.[18] showed experimentally that the counter-rotating swirl brings up larger area of near-stoichiometric mixture of fuel and air, resulting in higher temperature field distribution within the stabilization zone compared with the co-rotating swirl case.

In the diesel reformer application, swirl flow is effectively controlled by a swirl control valve (SCV), a device typically employed in small diesel engines. This swirl facilitates combustion and improves engine power. AVL incorporation verified that the usage of the SCV leads to a reduction in soot and NO*x* emissions under low engine speeds and load driving conditions. In addition, a combination of vertical swirl (i.e., tumble) and swirl created by other types of SCVs is found to promote flame development in the early stages of the combustion well with the air. Thus, a failure of synchronizing the injection timing at the moment that the swirl flow has an optimal effect on the fuel spray affects combustion efficiency. The swirl helps the flame to spread wider in the chamber and decreases the momentum of the injected fuel, so that the flame could distribute and stay for a long time in the center area of the chamber, where the flame used to extinct earlier without the swirl flow. Datta [12] also reported that imparting swirl to the dilution air can help in mixing and in the improvement of the exit pattern factor. According to Karatzas [13], mixing of fuel with the air and water vapor is of high importance in a diesel reformer before the fuel impacts the catalyst and causes wetting. Proper mixing promotes effective hydrogenation and thus, higher reformation efficiency.

The prime challenge in designing a diesel reformer is creating a perfect mixture of fuel and oxidant before contact with the catalysts, while preventing auto-ignition of the mixture. The

establishment of a homogeneous mixture of vaporized fuel and oxidants before contact with the catalyst is essential for the complete reformation of diesel and the protection of the catalysts from rapid thermal stress and degradation [21]. In recent years, several methods, such as cool flame or direct evaporation in preheated steam, have been proposed to resolve this problem. These methods have however been shown to produce large amounts of soot or unstable reformers with high risk for auto-ignition due to prolonged residence times in the reactor. In order to avoid the characteristic soot formation, associated with rich diesel oxidation at elevated temperatures, system must be designed so that the evaporated mass is mixed rapidly to homogeneity avoiding rich zones.

To summarize, the MVCO injector coupled with the swirl-producing adapter, is expected to ensure a completely homogeneous mixture of diesel fuel, air and water, which has been the biggest challenge in the design of a diesel reformer. The motivation of the study is to experimentally evaluate the atomization performance with the combination of above technologies.

2.6 Weber Number

The Weber number is important in discerning the droplet breakup regime. There are three breakup regimes. Bag breakup of droplets commences at about We ~ 12. Transition to 'shear-type' breakup occurs at higher Weber numbers (We > 80) and 'multimode' breakup (combined bag- and shear-type) occurs in the intermediate Weber number range (Wu et al. 1993). 'Catastrophic' breakup occurs at about We ~ 450.

The drop breakup process occurs in two stages. During the first stage, under the action of aerodynamic pressure, the drop distorts from its undisturbed spherical shape and becomes

flattened, or disk shaped, normal to the air flow direction. This feature exists in all three drop breakup regimes. During the second stage of the drop breakup process, the three drop breakup regimes display different breakup features. In the bag breakup regime the appearance and growth of holes on the bag sheet blown out of the center of the flattened drop is the dominant reason for the breakup; in the so-called shear or boundary-layer stripping breakup regime the results indicate that bending of the flattened drop's edge under the action of aerodynamic pressure, followed by production of folds on the bent sheet results in production of ligaments aligned in the direction of the air flow; and in the 'catastrophic' breakup regime the growth of capillary waves on the flattened drop surfaces, combined with the bending and folding of the sheet edge makes the breakup process demonstrate 'catastrophic' breakup characteristics. In addition, the experimental results confirm that for drops with different sizes, the same breakup regimes appear when the Weber number is held constant, and the Reynolds number does not play a dominant role. Some criteria for predicting drop breakup regime transitions in steady high-speed gas flows have been presented in [50].

2.7 Existing Technologies

Numerous studies have reported macro properties of the spray such as the spray tip penetration, cone angle and micro characteristics such as droplet size/velocities of a certain type of injector using various laser diagnostic techniques [32, 42-49]. Kostas et al [32] investigated the diesel fuel spray injected from a common rail injector with different injection and ambient pressure for duration of 0.5 ms from the start of injection using high speed digital imaging. They reported the spray penetration of 30-35 mm with a spray velocity of about 200 m/s at an ambient pressure of 1 atm. Moon et al. [43] investigated gas entrainment characteristics of diesel fuel injected by a group of closely-spaced two-orifices (group-hole nozzle) using LIF-PIV technique.

They showed that the group-hole nozzle displayed a spray penetration of about 53 mm at 1 ms after start of injection. The group-hole nozzle had higher spray penetration and spray velocities compared to the conventional single-hole nozzle spray, along with a higher fuel evaporation ratio as well. Park et al. [44] compared spray characteristics of diesel fuel and DME at high fuel temperatures and under various ambient conditions from a diesel injector with six holes, using a high-speed camera. They illustrated that diesel fuel has a long narrow spray shape while DME has a short wide spray shape. They reported spray penetration of about 70 mm and tip velocity of about 120 m/s at an ambient pressure of 0.1 MPa and ambient temperature of 293 K for the diesel fuel. Mitroglou et al. [45] investigated sprays from high-pressure multi-hole nozzle injected into a constant volume chamber. They reported a maximum penetration length of about 50 mm at 200 bar injection pressure and 1 bar back pressure, the tip velocity reaches 120 m/s in the axial direction and the droplet size falls in the range around 10 to 20 μm. In another study, Douwel et. al [46] studied macroscopic diesel spray shadowgraphy using high speed digital imaging in a high pressure cell. Diesel fuel sprays produced by a modern, heavy duty common rail injector were studied in a newly developed high pressure, high temperature cell, using digital high speed shadowgraphy at 4500 frames per second. They developed a general and consistent method to determine the macroscopic spray geometry characteristics such as the spray cone angle and penetration length using lateral cross-section of the spray shadow as a function of time. Using this method, the maximum jet penetration observed was about 90 mm at a common rail pressure of 150 MPa. Based on the results, they further suggested that the spray propagation is governed by competition of fuel injection delivering momentum to the spray. Table 1 tabulated the results of the previous studies.

To summarize, the velocity of fuel jet produced by a modern common rail injector can reach well above 100 m/s with tip penetration typically longer than 30 mm, meanwhile, multi-hole nozzle injector usually present more desirable features such as smaller droplet size compared with single-hole injector. These injector studies are summarized in Table 2.1.

Xanthas Karatzas et. al [14] used a a single fluid pressurized-swirl nozzle to inject liquid fuel as a fine hollow cone spray into the mixing zone for evaporation and blending with a mixture of superheated air and steam (300 °C) that enters the reformer from perpendicularly arranged injection holes about 40 mm downstream (Figure 2.2). Fuel was injected at about 10 bar. They developed it to further atomize and disperse the fuel into fine micro-sized droplets (<10μm). The air-steam injection holes were repositioned further upstream in the mixing zone to improve the reactant mixing with the fuel and to prevent the occurrence of stagnant zones.

C. Mao et. al [37] surveyed and modeled a few fuel delivery systems for diesel reformer applications (Figure 2.3). Fuel was injected at 50-145 psig inlet pressure. He studied various injectors like the multipoint impingement injector, gas-assisted simplex injector and mixing, and a high energy piezoelectric simplex injector. Regarding the multipoint impingement injector, he found that the overall signal strength for diesel fuel is lower than Jet fuel due to different physical properties. Jet fuel distribution also appears to be both more uniform and more repeatable. Mixing devices do not appear to provide any noticeable benefit to the multipoint impingement injector concept. Species distribution appears to be more scattered as steam/carbon ratio decreases when using mixing devices.

The gas-assisted simplex injector (Figure 2.3) has a simple, more robust design and less prone to internal coking. It is easily adaptable to a different reformer. It has a narrow spray angle to minimize carbon deposition on the chamber wall and provides good atomization when

there is adequate gas inlet pressure, however mixing devices are required for uniform mixture distribution. Both the above injectors had SMDs in the range of 10-30 um (3 inches downstream from injector). As far as the piezoelectric simplex injector is concerned, it has excellent atomization for low flow rate applications. However the power consumption needs to be minimized. It also showed a drift of operating frequency and spray quality due to changes of temperature and flow rate. It has great potential for pulse modulated injection.

J. M. Meacham and M. J. Varady et. al [38] showed the visualization of droplet formation and ejection from a micro-machined ultrasonic droplet generator. Visualization and scaling of drop-on-demand and continuous-jet fluid atomization of water were presented to elucidate the fluid physics of the ejection process and characterize the modes of operation of a novel micro-machined ultrasonic droplet generator. The device comprises a fluid reservoir that is formed between a bulk ceramic piezoelectric transducer and an array of liquid horn structures wet etched into (100) silicon. At resonance, the transducer generates a standing ultrasonic pressure wave within the cavity and the wave is focused at the tip of the nozzle by the horn structure. Device operation has been demonstrated by water droplet ejection from 5 to 10 um orifices at multiple resonant frequencies between 1 and 5 MHz. The intimate interactions between focused ultrasonic pressure waves and capillary waves formed at the liquid–air interface located at the nozzle tip are found to govern the ejection dynamics, leading to different ejection modalities ranging from individual droplets to continuous jet. Specifically, they reported the results of high-resolution stroboscopic optical imaging of the liquid–air interface evolution during acoustic pumping to elucidate the role of capillary waves in the droplet formation and ejection process. Although the above droplet generator was used for water, it might have interesting applications in fuel processing as well.

C. Ayrault et. al [39] conducted an experimental investigation to study diesel fuel reforming by a Recirculation type Electro-Hydro-Dynamic Atomization system (REHDA) (Figure 2.4). The fuel in the Electro-Gydro-Dynamic (EHD) atomization system was injected through a hollow tube electrode that was powered using a high voltage pulse power supply. A hollow ring on the ceramic holder for the hollow tube served as the ground electrode. Experiments were performed for diesel fuel with a flow rate of 4 mL/min. The fuel was recirculated through the EHD atomization system 1 to 5 times. The maximum applied voltage varied from 0 to 26 kV at a pulse repetition rate of 200 Hz. The liquid by-products from the REHDA system were analyzed using a GC. The results showed the REHDA could achieve significant cracking of the large CxHy components to the decane level.

The diesel fuel reforming by an EHD atomization system was characterized for three different flow regimes. The flow regimes for pulse high voltage operation of the EHD atomization system changed from the lower voltage droplet flow (regime I) to a jet with EHD reduced volume droplet flow or partial EHD atomization (regime II) with increasing applied voltage. Full EHD atomization (regime III) was observed at the highest voltages. The optimum diesel fuel cracking was observed between regimes II and III. Diesel fuel cracking by the REHDA system operated under pulse high voltage driven mode shows significant cracking of larger CxHy components in the liquid by-products to the decane level. There was evidence of some cracked liquid by-products smaller than decane but the change in these by-products was much smaller than observed for decane. This was attributed to the small CxHy components in the liquid are converted to gas-phase products by the EHDA generated plasma. The cracking efficiency depended on the location of the air injection from the RCDRS device with locations

closer to EHD atomization producing significantly higher cracking to the decane level. The cracking increased with the circulation of the diesel fuel up to five times.

Kang et. al [40] devised an ultrasonic injector (UI) for effective diesel delivery (Figure 2.5). The UI can atomize diesel into droplets (~40um) by using a piezoelectric transducer and consumes much less power than a heating-type vaporizer. In addition, reforming efficiencies increased by as much as 20% compared with a non-UI reformer under the same operation conditions. They confirmed that effective fuel delivery was linked to the reforming kinetics on the catalyst surface. A 100-We, self-sustaining, diesel auto-thermal reformer using the UI was designed. In addition, the deactivation process of the catalyst, by carbon deposition, was investigated in detail.

The UI is located at the top of the reactor to deliver the diesel. A water line for vaporization is in contact with the reactor wall like a coiled spring. Air is injected through an ultrasonic device (separate from the fuel line). The air is not only an oxidant but also acts as a shield, which can prevent atomized diesel from attaching to the reactor wall. In addition, it cools down the piezoelectric transducer. The reforming efficiency increased by about 20% in the micro-reactor when the UI was used. They attributed this improvement to the inhibition of the reactions that occur at high temperatures in the non-catalytic mixing zone that is located before the catalyst bed. Poorly mixed fuel and oxidant lead to gas phase reactions, such as combustion at high fuel/air ratios in the non-catalytic mixing zone. During oxygen rich or lean combustion (or partial oxidation), the aromatic and olefin components may cause the reforming kinetics to slow down. The biggest drawback was found to be lack of proper mixing and also it was found that carbon deposition progressed very quickly in the reformer and deactivated the reforming catalyst after just 15 min.

Mark J. Varady and Andrei G. Fedorov [41] demonstrated spraying of a finely atomized liquid directly onto a hot catalyst (Figure 2.6). This work focused on developing a fundamental understanding of this approach and optimizing it by utilizing a droplet generator array with precise control over the droplet spacing, diameter, velocity, and trajectory, thus providing ultimate control over the reactor performance. The regular nature of the droplet generator array also enables modeling on a reactor-unit-cell basis with minimal empiricism, which can be used to optimize the reactor performance. The steady-state unit-cell model developed in this work accounts for the transport and evaporation of the droplet stream, impingement and subsequent film accumulation and vaporization, and gas-phase transport and reaction. The key components of the model were validated using relevant results from the literature to establish confidence in applying the complete model to predict reactor performance. Further, a reactor prototype mimicking the reactor unit cell used in the simulations was constructed and used to experimentally validate the comprehensive transport reaction model for the specific case of methanol steam reforming. The key idea is that the DDIR can be conceptualized as an array of identical unit cells, each of which contributes equally to the reactor output. This is a simple layered reactor design consisting of a droplet generator array and a catalyst layer separated by a space in which droplets travel while being heated and partially vaporized. Their experimental data from steam reforming of methanol matched well with their model data.

NASA Glenn Research Center (GRC) [16] has designed and built a facility to test reformer concepts having the capability of providing 10 kWe power. A special feature of this facility is an optically-accessible test section that affords the opportunity to obtain the desired flow measurements using a wide spectrum of optical diagnostic methods. These ports are on opposite sides of the housing and have a fixed offset from each other so that tangential swirl is generated

upstream of the diffuser/mixing chamber. Feed steam is supplied by a saturated steam line and is further superheated in an electrical super-heater to a maximum temperature of 700 K (800°F) before being metered and fed to the injector (Figure 2.7). The facility air supply is at 862 kPa (125 psig) and is heated electrically to a maximum temperature of 922 K (1200°F). Steam line heaters and electric jacket heaters for the injector assembly have been installed to minimize heat loss and provide a near isothermal profile to the test section. The injector rig is operated at near atmospheric conditions with the effluent valve at 100% open to discharge the cooled combustor effluent to the outside.

To date, further research is still needed in order to make a diesel PEFC-APU system a practical and feasible option for commercialization. A higher efficiency of the fuel processor can be achieved by smarter reactor designs, better integration of each segment and better understanding of the overall process. One key segment where smarter, less expensive catalyst and reactor designs as well as process assessment are still needed is the fuel reformer, which forms the 'heart' of the system. Poor reformer performance can result in a negative "domino effect" causing degeneration and deactivation of the other components in the subsequent segments. A good fuel reformer design could enhance the reforming efficiency and hydrogen production greatly. Hence, extensive research is needed in this area which is the scope of this thesis.

Chapter 3

Experimental Facility and Methodology

3.1 MVCO Injector and Swirl Adapter

The Micro-Variable Circular-Orifice (MVCO) injector provides adaptive spray penetration, variable spray angles, variable spray patterns and SMD, is flexible for different modes of combustion and operating conditions. The moving needle and nozzle body generate a micro-variable circular orifice, which is coupled with micro-channels, is equivalent to a 7~50 variable micro-hole nozzle with hole-diameters less than 0.10mm, with minimum goes to 0.05mm. It can generate a conical spray only or mixed-mode conical-multi-jet spray patterns to meet the needs of different engine operating conditions. The equivalent flow rate of the hollow conical spray can be defined as 50% of that of a 7X0.185mm multi-hole nozzle. Figure 3.1 shows the dimensions of the MVCO injector.

The swirl-producing adapter is fit on the tip of the injector by means of two O-rings. This adapter, with an outer diameter of 76.2 mm, is designed to be exactly fitted on the injector. It has two sets of concentric holes for the supply of air and water, which promote swirl. The outer set of holes produce a counter-clockwise swirl and the inner set produces a clockwise swirl, which vastly enhances mixing of the fuel with air and water. This is expected to enhance the mixing of air, fuel and water to a complete homogeneous mixture. A picture indicating these holes is shown in Figures 3.2 and 3.3.

3.2 Air and Fuel Circuit

The experiment was carried out on an optical engine facility, where only the fuel injection system is used as shown schematically in Figure 3.4. The injector was supplied with high pressure fuel from a common rail connected to a Bosch high pressure automotive diesel pump. A 3 kW 3-phase electric motor controlled the pump speed via a 3-phase inverter/controller. A low pressure diesel fuel pump supplied fuel from the fuel tank to the high pressure pump. A bypass and return fuel line arrangement through the injector and high pressure components returned surplus fuel to the fuel tank via a heat exchanger. Cooling water flow through the heat exchanger maintained the fuel in the tank at a constant temperature of 40 °C. Further downstream, the fuel is injected into atmosphere and collected effectively through a locally built exhaust collection system.

The high pressure pump also came with a pressure regulator which is controlled by the LabView program. The control is made possible through a custom-designed circuit which supplies the necessary voltage to the pressure regulator in order to vary the fuel pressure.

Once the fuel entered the common rail, an Omega pressure transducer is installed to monitor the fuel pressure inside rail using Labview program. The injection system is controlled by a locally-made injector driver, which provides the required current to lift the needle inside injector at a given timing. The returned fuel from both the injector and the high pressure pump were cooled through an air-cooled heat exchanger before recollected in the fuel tank so that the whole injection system would not be overheated.

Although the pressure in the common rail is quite high, the MVCO injector's orifice can be used to reduce the pressure to a desirable value, such that it can be implemented for automotive applications.

Shop air was supplied at the necessary inlet pressure (30 psi and 60 psi) through a rotary pump. From the pump, it was supplied to the swirl adapter inlets through plastic tubing.
PDA data acquisition needs a lot of fuel to be injected, compared to the imaging data, and hence, a fuel collection system was built as shown in Figure 3.5. Two flexible drain pipes were used to suck the fuel vapor through a blower and passed onto the room exhaust.

3.3 Laser Diagnostics

3.3.1 High Speed Imaging

High speed images for both the front and bottom views of the spray were obtained with a non-intensified high speed digital camera (Phantom V7.1). The light source is supplied by a copper vapor laser (Oxford Lasers LS20-50) which can be externally controlled to run up to a maximum frequency of 50 kHz with pulse duration of 25 ns. The high-speed camera and the copper-vapor laser were synchronized at two different speeds. For the front view measurement, the camera and the laser were synchronized to 15,037 frames per second to produce time resolved measurement at a spatial resolution of 512×256 pixels. For the bottom view measurement, we increased the spatial resolution to 512×512 pixels to cover a larger field of view and consequently the camera speed was reduced to 8,200 fps. For both measurements, a Nikkor 105 mm focal length lens was used for the high-speed imaging and an exposure time of 3 μs was used. The short camera exposure and laser pulse duration assured suitable capture of the image

during the image acquisition. As pointed in previous studies [32], synchronization of the camera, laser and fuel injection was of critical importance, as a time deviation of as little as 100μs could result in a complete mismatch of the start of injection (SOI); two signal generators in conjunction with a custom made delay generator were employed to coordinate the signals so that the SOI was captured accurately.

The spray penetration S_p as a function of time is obtained directly from the acquired time resolved spray images. Calibration of the tip penetration measurement was first performed by analyzing digitally generated images of a target whose precise displacement was known. Unlike previous studies of single-hole injectors, where the spray penetration is usually determined from the displacement of the spray edge from the injector orifice along the nozzle axis, the penetration determination of the current study is more complicated due to the unique spray pattern generated by the MVCO. The technique for the penetration determination will be illustrated in detail as follows. As can be seen from the bottom view spray images, the spray contains more than twenty single jets and they are distributed almost evenly around the tip, which implies an axisymmetric cone-shape spray. With such a spray pattern, one way to determine the penetration geometrically is to measure the displacement from the orifice (in the center) to the edge of each individual jet from the bottom view. The averaged displacement should be further divided by $cos(\theta/2)$, where θ is the cone angle measured from the front view (see Figure 3.6). It should be noted that θ here is the maximum angle projected on a view plane among two individual jets rather than the cone angle of an individual jet. The most challenging part of this method is to design an algorithm to identify the individual fuel jet from the bottom view images; even assuming a correct value is obtained, the final determination of the penetration will still be affected by the error in the θ measurement.

Another way to acquire the penetration length, which was applied in this study, is directly from the front view measurement, based on the displacement between the orifice and the furthest tip point, or geometrically the hypotenuse of the triangle as illustrated in Figure 3.6. It should be mentioned first that the acquired spray image is the line of sight accumulation of the signals scattered by the liquid spray jet, yet the image lets us consider an imaginary "view plane" on which all the collected signals are imposed. Then the "hypotenuse" in the front view image should be interpreted as the projection of the actual penetration length on the view plane. A major assumption of this method is that there exists one individual fuel jet whose axis is exactly located on the front view "hypotenuse" which is hard to validate, as the rotational orientation of the injector is completely random; however considering that the number of jets generated are well above twenty, depending on the injection pressure, the angle φ between the left-most fuel jet axis in the front view image and the view plane is really within 10 degrees, leading to a difference between the projected penetration length and actual length to be within 3 % as illustrated in Figure 3.7. Therefore, it is reasonable to determine the spray penetration using this method. Detection of the "hypotenuse" of the spray is, similar to a number of previous studies, based upon an intensity threshold criterion to be met to distinguish the spray edge from the background.

3.3.2 PDA Measurement

A 2D Dantec PDA system with a BSA P60 processor coupled with a 58N70 detector unit was used for the measurement of the droplet velocities and diameters. The transmitting and receiving optics were installed on a three dimensional traverse so that the measuring position can be

precisely controlled. An argon-ion laser with a maximum power of 8.5 W was used and the output was aligned with the fiber optic unit. This unit was responsible for splitting the laser beam into two pairs of different wavelengths; each pair delivering two beams with equal intensity after proper alignment with the manipulators. The first pair consisted of green beams with a wavelength of 514.5 nm, responsible for the axial velocity component, while the second pair consisted of blue beams with a wavelength of 488 nm, responsible for the radial velocity component. A Bragg cell unit is positioned inside this fiber optical unit to provide a 40 MHz frequency shift between two the beams within each pair. Light scattered by the droplets was collected by a 310 mm focal length lens positioned at 30 degrees to the plane of the two incident green beams to ensure that refraction dominated the scattered light as can be seen in Figure 3.8

The signal from the photomultipliers was transmitted to the processor unit where all the data processing was carried out. The processor was connected to a desktop computer via an ethernet adapter where all the acquired data was saved for further analysis. The measurements, similar to the high speed images, were synchronized with the injection signal, and a time window of 10 ms after SOI was used as the limit for each injection event.

The impact of the signal to noise ratio (SNR), signal gain, record length, applied photomultiplier voltage has been discussed in [42]; a proper configuration of these parameters was chosen according to different testing cases to ensure a reasonably good data rate (above 200 samples/second) and validation rate (above 80%). Difficulties in measurements were encountered for high pressure injection, especially in the central part of the spray jet and near the nozzle exit region owing to the strong attenuation of the incident laser beams and the scattered light. The PDA experimental setup is shown in Figure 3.9. A detailed summary of the PDA

settings is shown in Table 3.1. The direction of the axes is shown in Figure 3.10. Table 3.2 shows the positions at which PDA measurements were carried out.

There are several validation criteria for the LDA and PDA. First, there is the burst detector which is triggered by a signal that exceeds a certain threshold. Then we check to see that the frequency of the signal found via FFT is at least 4X higher than the next highest peak in the spectrum. If not, the signal is rejected. Another rejection criteria is based on bandwidth – i.e. if the particle velocity is 10 m/s but the range is limited to a lower value (say 8 m/s) so the resulting histogram is cut off, the higher speed particles will of course not be validated. As far as the PDA, there are additional validations such as the so called spherical validation which requires consistent phases between detectors U1/U2 and U1/U3. Tolerance for this is set at about 10%. Further rejections occur if the particles are out of range on the low or high side.

Chapter 4

Experimental Results and Discussion

4.1 MVCO Injector without Swirl Adapter

4.1.1 Spray Visualization

The spray evolution of an individual injection event from the front view and bottom view is shown in Figure 4.1 and Figure 4.2 respectively. Each figure contains three rows representing three different injection pressures, namely 300 bar, 500 bar and 700 bar from left to right respectively while the injection duration was set at 0.5 ms. The images displayed are chosen in particular to show the beginning stages of the injection event. The unique spray pattern characterized by MVCO (compared to the conventional injector) can be observed. The most apparent difference is the multiple fine jet plumes produced by the MVCO injector, which manifests an "umbrella" shape, while for the conventional multi-jet injectors, the individual jet plumes usually can be clearly observed. Considering the same amount of fuel injected, the conical spray coming from a single annular micro ring from MVCO was more uniformly distributed on the periphery or circular direction compared to the other conventional multi-hole fuel injector, which is desirable for early injections in premixed combustion. On the other hand, it is true that the conventional multi-hole injection may also achieve reasonably uniform circumferential distribution with the proper design of the intake port to generate intake swirl, i.e. the air motion sweeps the spray such that the fuel droplets from one jet comes into contact with the neighboring one. Such swirl flow can only further improve the mixing process for the

MVCO as the turbulent kinetic energy delivered by the intake flow will induce the more violent breakup leading to finer droplets.

30 fuel jets on the periphery are observed from the images, which is a substantially higher number of jets compared to 6 jets from the conventional injector. Therefore the MVCO injector provides a much greater volumetric coverage for the same amount of fuel injected, which in turn will provide a more homogeneous mixture, compared to the conventional diesel injector. The front view images of the spray observed at 500 and 700 bar show a slightly "bumped" spray in the radial direction about halfway between the injector tip and the end of the spray jet, which is likely caused by the vigorous interaction between the fuel jets at higher injection pressure, leading to a slight accumulation of fuel inside the main jet body. The same phenomenon is not observed at 300 bar due to lesser number of fuel jets as well as less violent aerodynamically induced breakup. Such differences among various injection pressures provided the flexibility to optimize the injection according to the engine load. Note that the injection duration was kept constant, thus the injection pressure can be viewed as a reasonable representative of the engine load. At low load condition, the spray is characterized by a relatively narrow spray angle and shorter penetration so as to prevent wall wetting while at high load, the spray was widened to suit for higher power output. The bottom view (Figure 4.2) also shows the hollow cone feature of the spray, which is of crucial importance for air entrainment. As the closely spaced fuel jets interact with each other as the spray develops, there remains a major concern that insufficient air entrainment would be caused. The hollow cone shape provides a path from inside for air/fuel contact which should ameliorate the issue, yet such speculation should be further confirmed in future combustion studies.

Figure 4.3 quantifies the spray penetration calculated using the method aforementioned. It is seen that it increases along with time and reaches a quasi-steady state after about 1 ms. The quasi-steady state penetration length observed is about 20 mm, 24 mm and 26 mm for the three injection pressure cases respectively. It can be observed that the spray penetration value of the MVCO injector for a given injection pressure is lower compared to some previously studied conventional diesel injectors [5-10], due to the simple fact that the total injected volume was divided into more jets, resulting in a lower penetration for each individual jet, which will be beneficial in avoiding wall wetting especially under low load conditions. The quantified spray cone angle for different injection pressures is also summarized in Table 4.1. Spray cone angle increases with increasing injection pressure which is in agreement with the observation from the spray images as discussed above.

4.1.2 Droplet Size and Spray Velocity

The challenging aspect of the PDA measurement is the fact that the jet plume is hard to detect with the naked eye, and therefore it was difficult to determine the measurement location. To overcome this difficulty, the measuring position around the jet plumes was moved with a space resolution of 1mm until the highest velocity was detected, after which several close positions were picked up for comparison.

The mean droplet diameter and Sauter Mean Diameter (SMD) along both the radial and axial directions is illustrated in Figure 4.4 and Figure 4.5 respectively. In both directions, the variation of the droplet size is minimal indicating a uniform drops size distribution. No apparent trend of the droplet size against injection pressure is observed which is desirable for engine

optimization according to engine load. Figure 4.4 (b) also shows increasing mean diameter as we move higher up in the radial direction. This can be explained by the fact that at around 40-45 mm radial position, we are almost exactly on the jet where the droplets are yet to undergo breakup. However the lighter, already dispersed droplets move away from the jet towards the centre, displaying a smaller mean diameter.

The following paragraphs discuss droplet size and velocity data, including a Weber Number analysis at position C. Although measurements were made at other positions, position C offered the highest data rate for tests without the swirl adapter. Hence only position C is discussed below. In Section 4.2, results with the swirl adapter are explained where measurements at all other positions are discussed with a special focus on position B.

The droplet size probability density function at different injection pressures are shown in Figure 4.6 where the normalized counts of all samples are plotted against their size in a 0.5 μm bin. It is seen that distributions peaks lie at about 9-12 μm mainly due to the more violent breakup induced by the unique spray pattern of the MVCO. The narrow bandwidth of the distribution also indicated more uniform and finer droplet size distributions than conventional multi-hole injectors under similar injection pressures and back pressures.

Figure 4.7 displays the SMD distribution at an axial position of 22 mm. It is observed that the SMD value is somewhat uniform for each injection pressure. Comparing the distributions at the different injection pressures, we see that the 300 bar and 500 bar cases yield drops which show smaller SMD compared to the 700 bar case. It is important to note that the spray cone angle changes with injection pressure and hence the exact position of the spray jet will also change radially, with changing injection pressure. This might explain the different distribution

of SMD values for different injection pressures. With the 300 bar and 500 bar cases, we see that the the lowest SMD value obtained is about 20 μm. However, the 700 bar case displays the most uniform SMD distribution, albeit with higher values.

Figure 4.8 illustrates the droplet velocity in both axial and radial directions at position C, without the swirl adapter. At 300 bar, the peak axial velocity measured was nearly 99 m/s. At 500 bar, the axial velocity detected is about 80 m/s. As injection pressure goes up to 700 bar, the highest axial velocity decreased slightly to 70 m/s. Again, as discussed in the previous section, the total samples collected in this case are limited due to the laser attenuation caused by the dense spray cloud. The measured velocity corresponds to a spray cone angle of about 110^0~120^0, which is in agreement with the image results. Contrary to some previously studied injectors, the measured velocity for this new MVCO injector is lower than most of the injectors and swirl atomizers found in the literature survey [32, 42-49], where a maximum velocity of around 100-140 m/s is detected. Both the radial and axial velocities of the MVCO conical spray are much lower than a conventional multi-jet from a conventional multi-hole diesel injector, where the jet velocity is generally above 150 m/s under similar injection pressure and back pressure. The lower velocity profile of the conical spray of MVCO is favorable for earlier injections for PCCI combustion, where the back pressure is low and no piston or cylinder liner wetting is desired. The lower velocity profile for early injection is also favorable for highly downsized small cylinder engine.

Figure 4.9 shows Weber number and Reynolds' number against time and droplet size for Position C. The Weber Number and Reynolds Number are representative of velocity, and hence these plots give us an idea of the trend of velocity with respect to drop size. The Weber number gives an indication of the breakup regime of the droplets, and also gives us some idea of the

ability/tendency of the droplets to spread out and form a thin film over a surface upon impingement. This is desirable in diesel reformer applications, as it is better if the fuel forms a thin film over the catalyst. Higher Weber number also indicates a 'catastrophic' breakup of droplets, which will provide much higher atomization and better mixing. Apart from this, Reynolds number was plotted against droplet size to identify the turbulence of the spray. The formulae used are shown below.

$$\text{Weber Number, } We = \frac{\rho v^2 l}{\sigma} \quad \ldots \text{(Eq.2)}$$

where

- ρ is the density of the fluid (kg/m^3).
- ν is its velocity (m/s).
- *l* is its characteristic length, typically the droplet diameter (m).
- σ is the surface tension (N/m).

$$\text{Reynolds Number, Re} = \frac{\rho v D}{\mu} \ldots \text{(Eq.3)}$$

where

- ρ is the density of the fluid (kg/m^3).
- ν is its velocity (m/s).
- *D* is its characteristic length, typically the droplet diameter (m).
- μ is the dynamic viscosity of the fluid (Pa·s).

The properties of diesel fuel were calculated at ambient temperature (25° C) and pressure (1 atm). This is a valid estimation, since fuel was injected into the atmosphere.

From Figure 4.9, it is seen that at about 1 ms (close to the end of fuel injection), a large amount of particles reach Weber numbers close to 1000. It is important to note that there in a PDA measurement, there will be a large number of points which show zero velocity, and that is why there is an accumulation of points at We=0. However, In the Weber number vs diameter plot, we see that particles in the diameter range of 5-20 μm (the mean diameter) show a heavy accumulation at a Weber number of 500. This indicates that the droplets are in the 'catastrophic' breakup regime, ensuring a higher degree of atomization and hence, enhanced mixing. Again, with lower data rate, the accumulation goes down.

4.2 MVCO Injector with Swirl Adapter

4.2.1 Spray Visualization

Figures 4.10 – 4.12 show the spray evolution (side view) of the MVCO injector coupled with the swirl adapter, at the three different injection pressures, with different inlet air pressures. It can be seen clearly that the spray becomes much wider with the use of the adapter. At around 1ms ASOI, the fuel jets are no longer distinguishable, and only a highly dense fuel-air mist is observed. The liquid jet penetration also becomes slightly shorter.

Figures 4.13 – 4.15 show the same spray evolution from the bottom view. The outline of the adapter is visible in these images. At 0.72 ms, there is a noticeable difference between the spray without the adapter and that with the adapter. The jets are no longer distinguishable due to

the swirling air motion. Also, from 0.72 ms – 0.97 ms, the inward (circular) motion of the air can be seen. Therefore, a clear swirling motion is observed. This is validated by the results obtained from the PDA measurements.

4.2.2 Droplet Size and Spray Velocity

The following paragraphs discuss droplet size and velocity data, including a Weber Number analysis at position B. As mentioned earlier, although measurements were made at other positions, position B offered the highest data rate for tests with the swirl adapter. After a detailed discussion of results obtained at position B, a summary of results obtained from all other positions is presented.

For each position, at least two runs were carried out to assure the repeatability of the experiment. Figures 4.16 (a), 4.16 (b) and 4.16 (c) shows the PDF distribution of droplet size at injection pressures of 300 bar, 500 bar and 700 bar respectively at three different inlet air pressures (0 psi – No air, 30 psi and 60 psi). It can be seen that the peak of the PDF gets shifted to the right at higher inlet air pressure, indicating an increase in mean droplet size with an increase in inlet air pressure. This is due to the fact that the the fuel droplets entrain the air, which causes a thin layer of air to surround the fuel droplets, resulting in an increased droplet size measurement.

Figure 4.17 shows the droplet velocity at position B at an injection pressure of 300 bar with different inlet air pressures. The radial velocity component observed was lower than that obtained without the swirl adapter. Figures 4.18 and 4.19 show velocity distribution at 500 bar and 700 bar injection pressure with air supply from the swirl adapter. It can be seen that the data

rate is slightly lower at these injection pressures compared to the 300 bar case, due to the dense fuel-air mist formed, which caused slight laser attenuation. Also note from the images that at 300 bar injection pressure, the individual fuel jets were easy to detect, while at 500 bar 700 bar, the spray cloud was formed and the interaction between the jets was so strong that the individual jets became difficult to capture. Again the velocity observed at higher injection pressures was lower than that without air supply.

The velocity data seen in Figures 4.17 – 4.19 shows a clear distribution of points below 0 (indicating movement in the opposite direction), extending up to 20 m/s at 60 psi air pressure. This indicates a rotational swirl motion with a velocity component found in the direction opposite to that of primary spray jet direction. Increasing the air pressure enhances this effect. This swirl is expected to greatly enhance the air/fuel mixing before the mixture reaches the catalyst in a real diesel reformer. It is important to note that the fuel is injected at relatively very high pressures compared to the air pressure, and hence the jet would just tear through the air mist formed. Even so, at comparatively lower air pressures of 30 and 60 psi, we see a strong swirling effect. The intensity of the swirl with higher air inlet pressures and its impact would be an interesting topic for future study.

Also note that all the velocity data shows the axial component of velocity. From the spray, it can be seen that there are three velocity components, and even 2-D PDA would not give us the complete velocity information. However, the axial component is the dominant one, and it gives a good idea of the spray velocity. Some other planar measuring technique, such as Particle Image Velocimety (PIV) for velocity measurement and Planar Droplet Sizing (PDS) for droplet velocity measurements should be considered in future studies.

Figures 4.20 – 4.22 shows Weber Number (shown by blue dots) and Reynolds Number (shown by red dots) at Position B at 300 bar, 500 bar and 700 bar fuel injection pressures with different air inlet pressures. Similar to Figure 9, we see quite a large number of points with We ~ 500. Although the swirl adapter reduces the velocity of the spray jet and imparts a rotational motion to the jet, the accumulation of droplets at We ~ 500 is still the highest. Peak values of Weber number are seen to go up with higher air pressure in the 500 bar case, indicating that the air flow enhances the 'catastrophic' breakup of the droplets. It is to be pointed out that the number of non-zero Weber number droplets is strongly affected by the data rate. The lower data rate causes the accumulation of droplets at higher Weber numbers to go down. This effect is seen in the 700 bar case.

Figures 4.23 and 4.24 show the axial and radial variation of the mean diameter and SMD respectively at different injection pressures with different air inlet pressures, with the plots in these figures having three curves showing three air pressures for each fuel injection pressure, showing the air impact variation with varying axial and radial positions. From Figures 4.23 (a), 4.23 (b) and 4.23 (c) it is observed that the axial trend (at radial position of 40 mm) all three injection pressures show quite similar trends, with an increase in mean diameter with increasing air pressure (due to air layer around the fuel droplet). However, there is no variation of mean diameter with varying axial position. The SMD values are seen to drop slightly as we move further downstream axially in the 500 bar and 700 bar injection pressure cases.

However, a very interesting observation is made by varying the radial position (at axial position of 22 mm) (Figure 24). All three injection pressures show that the mean diameter values are less affected by increasing air pressure, as we move up radially. At 25 mm radial

position, the mean diameters without and with air are furthest apart. But as we go higher up, they approach each other, and at 45 mm radial position, all three values converge at a single point. This shows that the air has least impact at the jet position itself, but has maximum effect towards the centre of the spray (hollow cone). Entrainment of the fuel droplets onto the air flow is seen to occur mostly towards the centre of the spray cone. This makes sense as the lighter dispersed particles which have undergone breakup are found towards the centre and are more likely to be affected by the swirling air motion. Therefore, as breakup occurs, particles would move towards the centre and have a swirl motion imparted to them as they approach the inner portion of the hollow cone. Looking at the radial trend in the SMD values, we see that the SMD values are slightly lower closer to the jet position (45 mm radial position) compared to the hollow cone region (25 mm radial position).

Figures 4.25 and 4.26 show the axial and radial variation of the mean diameter and SMD respectively at different injection pressures with different air inlet pressures, with the plots in these figures having three curves showing three fuel injection pressures for each air inlet pressure, showing the fuel injection pressure variation with varying axial and radial positions. Figure 4.25 shows that the mean diameter and SMD do not display any specific for varying injection pressures at all air pressure cases, again indicating the uniform atomization characteristics of the MVCO injector at different loads.

The radial variation (Figure 4.26) shows some interesting effects on mean diameter and SMD at different injection pressures. From Figure 4.26 (a) we see that the mean diameter for all injection pressures (no air) increases with moving up radially. This validates the earlier observation of lighter, smaller droplets towards the centre and relatively larger droplets closer to

the jet (periphery). However, it is seen from Figures 4.26 (b) and 4.26 (c) that this variation with radial position is eliminated with the introduction of air. This shows how the swirl brought in by the air enhances the mixing of fuel and air. This mixed fuel-air mist displays a uniform mean diameter distribution with changing radial position. The SMD trends do not show any noticeable effects due to air, but they do display the SMD peaking at different positions for different injection pressures, indicating the varying position of the jet at various injection pressures, due to the variation in the spray cone angle as discussed earlier.

Figure 4.27 shows the SMD distribution at an axial position of 22 mm with various air pressures at injection pressures of (a) 300 bar, (b) 500 bar and (c) 700 bar. The common trend observed among all injection pressures is that SMD shows a slight increase with the supply of air. The increase in SMD is pronounced towards the centre (where higher entrainment of fuel droplets onto air occurs). The amount of increase is highest with the 300 bar case, lower with the 500 bar case and is lowest at the 700 bar case. In Figure 4.27 (b), among the three air pressure cases for 500 bar, the 30 psi case shows the most uniform SMD distribution with the highest difference among SMDS being ~3 μm. For the 700 bar case in Figure 4.27 (c), the 60 psi case appears to be the most uniform. This may be justified by a theory that different injection pressures have an optimum air pressure at which the SMD is lowest and most uniform. However, this theory needs to be further explored by further experiments.

Figures 4.28 – 4.34 show velocity and drop size PDF distributions for different injection pressures and air pressures at all other measurement positions (excluding position B discussed above). It is seen that the data rate is maximum for different cases at different positions. For example, the 300 bar – no air case is seen best at position C, however, position H shows a high

data rate for 500 bar and 700 bar cases with air supply. The data rate is maximum at positions close to the jet, and lower around the jet. Position B discussed above provides the best results for all cases together and adequately represents the trends observed in all the other positions.

Chapter 5

Conclusions and Future Work

Spray visualization and characterization of an MVCO injector coupled with a swirl adapter has been performed using High-speed imaging and PDA. There are a few major conclusions that can be made from the experimental results.

The MVCO injector produces a very unique 'umbrella'-shaped spray pattern consisting of nearly 24 individual fuel jets, compared to 6 jets from the conventional diesel injector. The spray penetration is relatively much shorter, and the spray velocity reached upto 90 m/s at 300 bar injection pressure. The spray is also featured with adaptive spray cone angle according to different engine load. To this extent, the unique spray and atomization characteristics by MVCO can potentially enable adaptive in-cylinder combustion strategies which are impossible with conventional fixed-spray-angle multi-hole injectors. The PDA results also suggest finer and more uniform drop size distribution produced by MVCO. The conical spray of the MVCO injector also has a lower velocity profile comparing to conventional diesel injector under similar injection and back pressure conditions, which is favorable for down-sized small cylinder engine for highly premixed combustion.

When coupled with the swirl adapter, the spray pattern obtained is much wider, with a shorter spray penetration, caused by suppression of the radial component to the swirling air motion. A clear swirling motion is observed in both the spray images and the PDA results. The velocity measured showed a negative velocity component (previously unseen in measurements made without the swirl adapter), indicating a rotational motion due to swirl. The jet position was

also shifted in the radial direction due to the air motion. The mean droplet diameter was found to increase slightly with an increase in inlet air pressure through the swirl adapter, indicating fuel droplets entraining the air thus enhancing mixing. These effects were more pronounced towards the centre of the spray (hollow cone) and lesser towards the periphery. These characteristics are quite favorable in diesel reforming. The data rate obtained at higher injection pressures and inlet air pressures was slightly lower due to severe laser attenuation due to the dense fuel-air cloud. However, different positions provided optimum data rates for different measurement conditions, indicating the load-adaptive nature of the MVCO injector and the movement of the fuel particles due to swirl motion.

Some ideas for future work include conducting the experiment with air at higher inlet pressures (note that currently, the air inlet pressure is quite low relative to the fuel injection pressure), which would likely increase the intensity of swirl. Another idea would be to supply heated air and water (or water vapor) through the swirl adapter (the actual components injected in a diesel reformer). This would greatly enhance mixing and produce varied swirl characteristics, which would greatly enhance reforming efficiency. Studying species concentration by supplying the above mixture in to an actual diesel reformer would give the hydrogen concentration, through which reforming efficiency can be obtained, and further work could be done towards optimization.

Other ideas include performing spray visualization and measuring spray characteristics with planar velocity measurement techniques such as PIV, which would indicate the location and intensity of swirl more accurately. It would also be very interesting to study the combustion process in a diesel engine using the MVCO injector.

Tables

Authors	Type of fuel injector	Injection Pressure (bar)	Spray Penetration (mm)	Spray Velocity (m/s)	Droplet Diameter (μm)
Kostas et al.[6]	Common rail diesel injector	500	35	200	-
Moon et al.[7]	Group-hole Nozzle	1200	53	-	-
Park et al.[8]	Six-hole diesel Injector (Diesel and DME)	600	70	120	~ 10
Mitroglou et al.[9]	High-pressure Multi-hole nozzle injector	200	50	120	~ 8 - 10
Douwel et al.[10]	Heavy-duty Common Rail Injector	1500	90	-	-

Table 2.1 Summary of the Literature

PDA Receiver Properties	
Type	Fiber PDA
Scattering Angle	30 degrees
Focal Length	310 mm
Scattering Mode	Refraction
Beam Expansion	1
Beam Parameters	
Wavelength	514.5 nm
Beam Diameter	1.35 mm
Focal Legnth	400 mm
Beam Spacing	38 mm
Measurement Settings	
Center Frequency	-50 m/s
Bandwidth	162.66 m/s
Record Length	32 (Auto-Adaptive)
High Voltage Level	1200 V
Signal gain	28 dB
Max. Samples	25000
Max. acquistion time	60 s
Filter method	Overlapped
Spherical Validation	ON

Table 3.1 PDA Settings

Position	X (mm)	Y (mm)	Z (mm)	Diagrammatic Representation
A	18	0	40	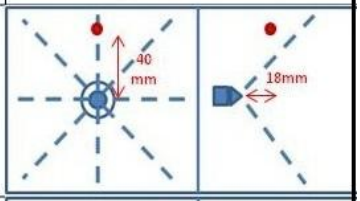
B	20	0	40	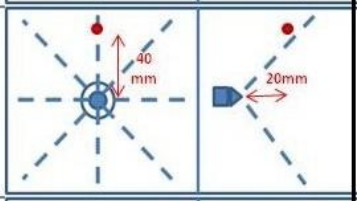
C	22	0	40	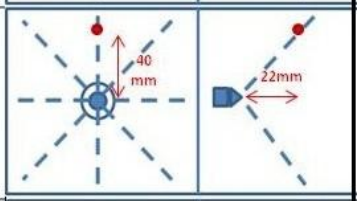
D	24	0	40	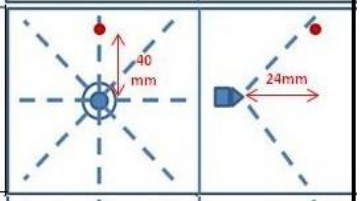
E	26	0	40	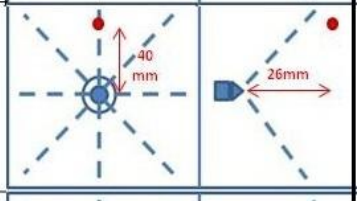
F	22	0	30	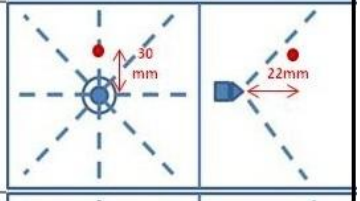
G	22	0	35	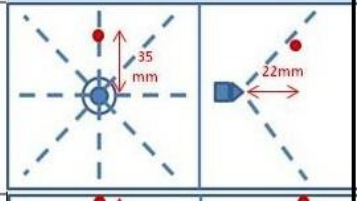
H	22	0	45	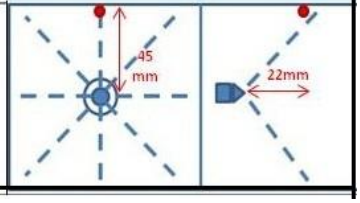

Table 3.2 PDA Measurement Positions

Injection Pressure (bar)	Spray Cone Angle θ (degrees)
300	118 ± 1
500	127 ± 1
700	130 ± 1

Table 4.1 Spray cone angles at different injection pressures

Figures

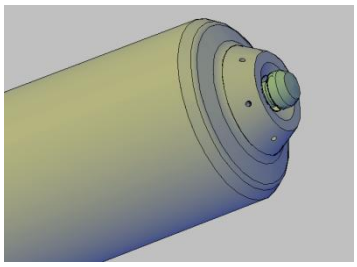

Figure 2.1 Illustration of MVCO conical-multi hole design

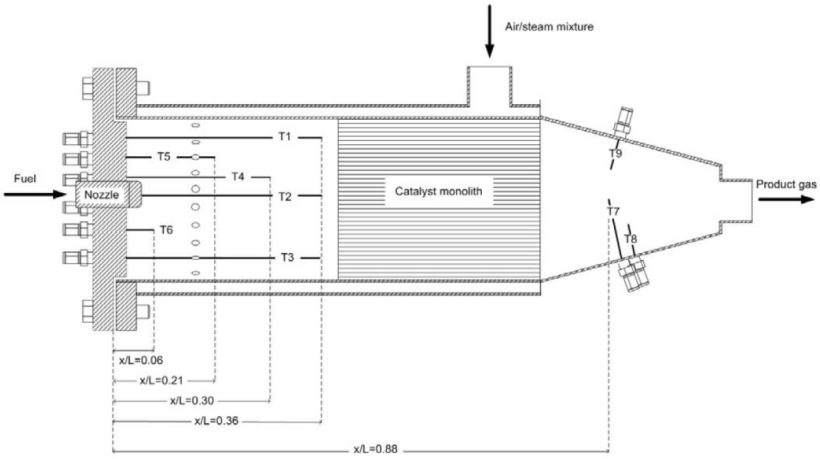

Figure 2.2 – Karatzas et. al's Reformer Setup [14]

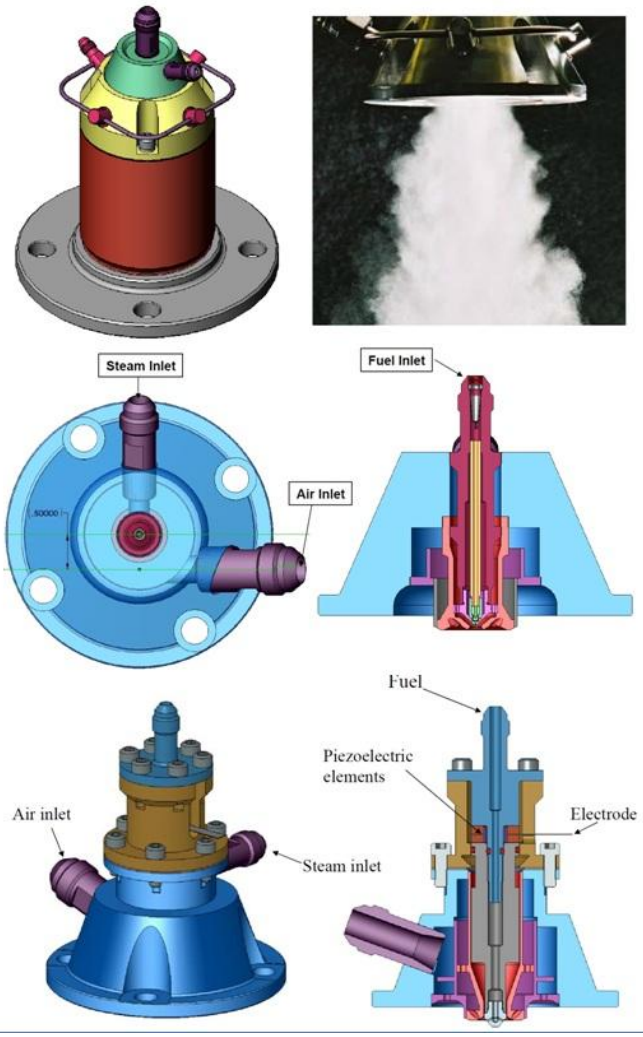

Figure 2.3 – Mulipoint Impingement Injector (top); Gas-assisted Simplex injector (middle); Piezoelectric Simplex injector(bottom) [Mao's study] [37]

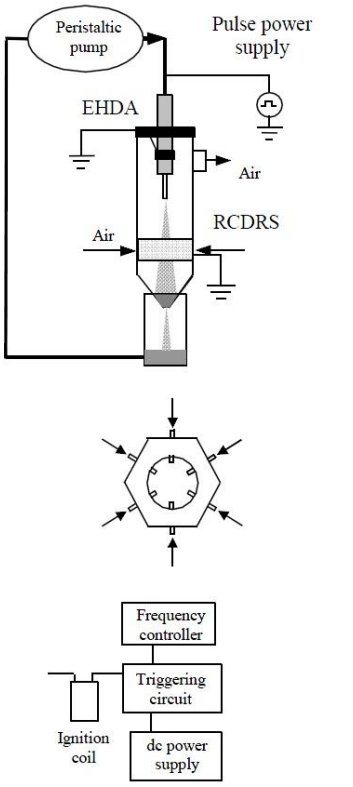

Figure 2.4 – Ayrault et. al's Recirculation type Electrohydrodynamic Atomization setup [39]

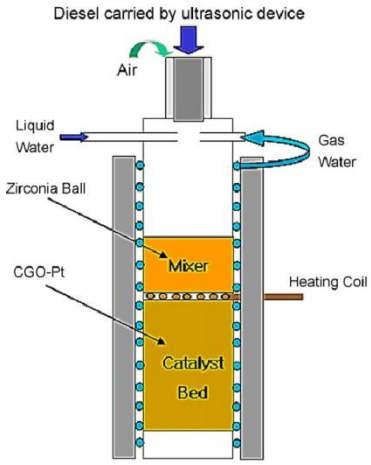

Figure 2.5 – Kang et. al's Ultrasonic Injector setup [40]

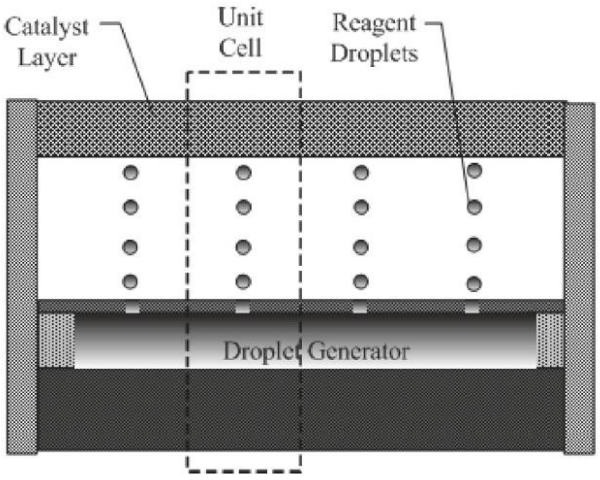

Figure 2.6 – Varady et. al's Direct Droplet Impingement Reactor [41]

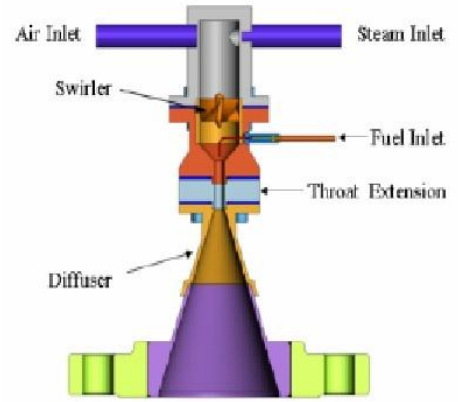

Figure 2.7 – Yolanda et. al's Swirl venture mixer [16]

Figure 3.1MVCO Injector Dimensions

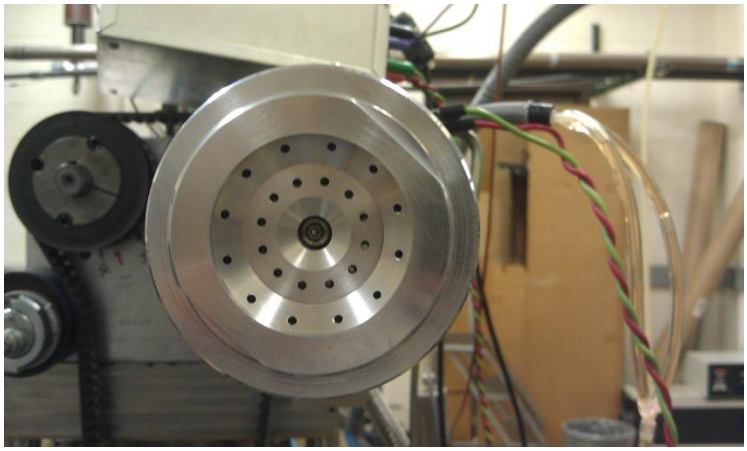

Figure 3.2 Front view of the swirl-producing adapter; the outer set of holes produce a counter-clockwise swirl and the inner set produces a clockwise swirl.

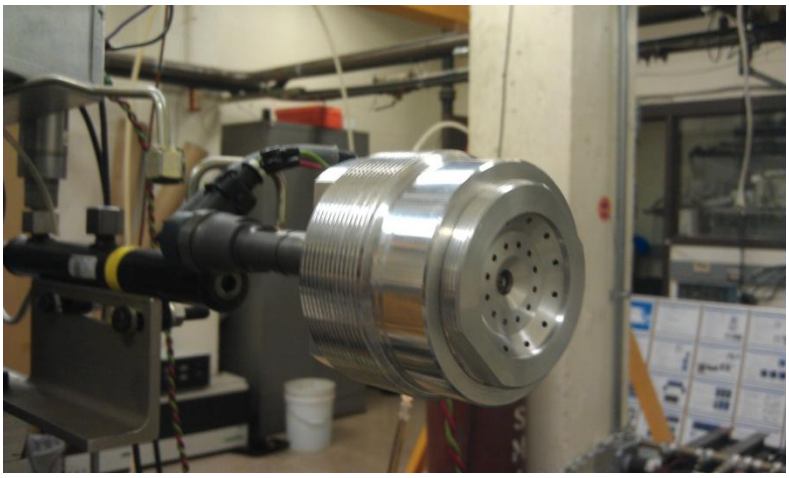

Figure 3.3 Isometric view of the swirl-producing adapter fit on the MVCO injector

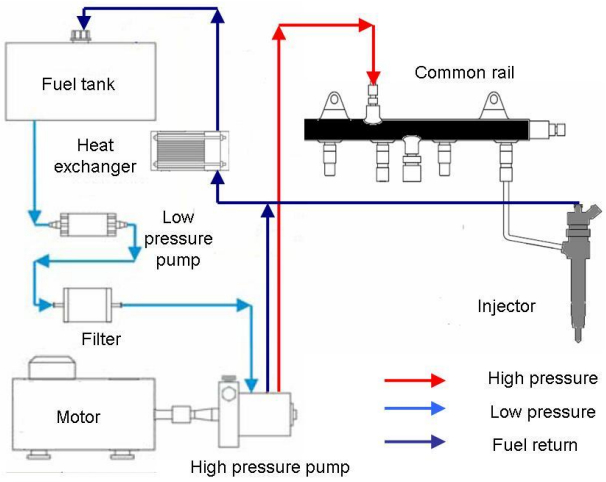

Figure 3.4 Experimental Setup – Fuel Injection System

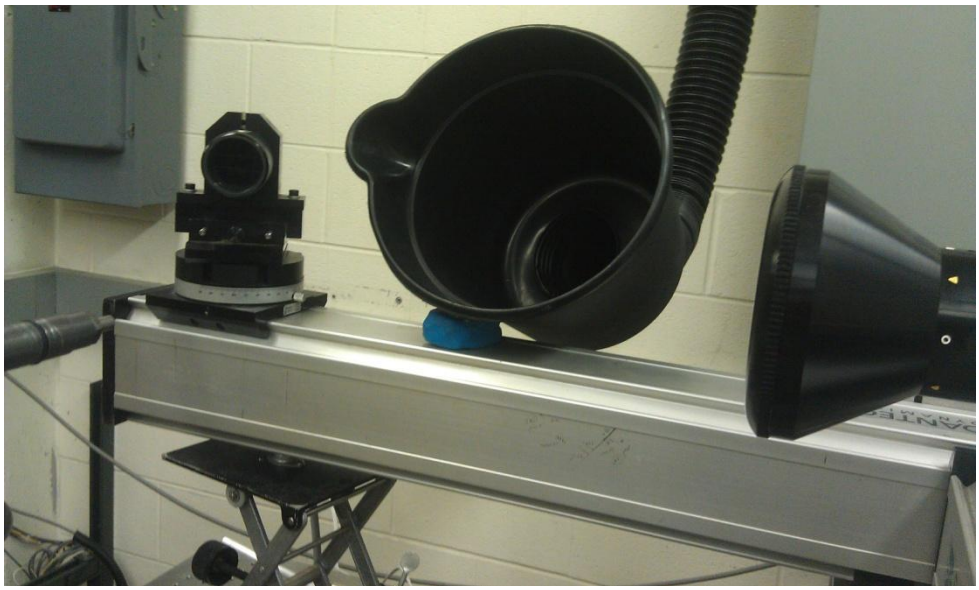

Figure 3.5 Exhaust collection device

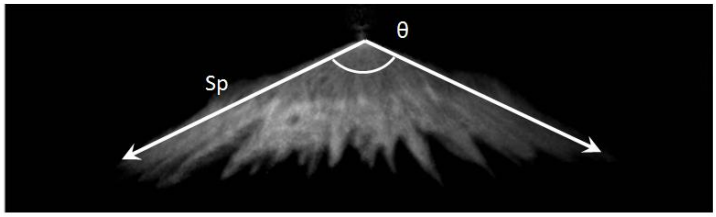

Figure 3.6 Spray characteristics representation

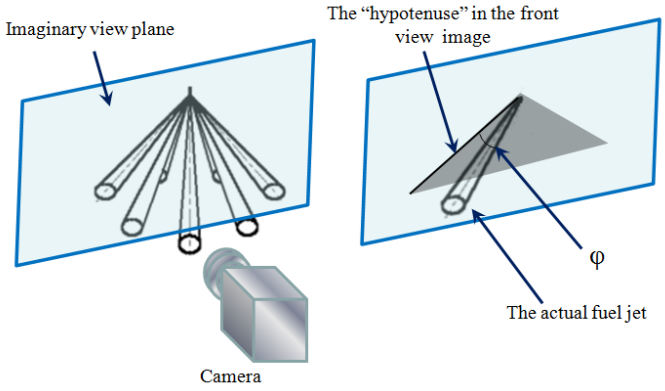

Figure 3.7 Determination of the spray penetration Sp

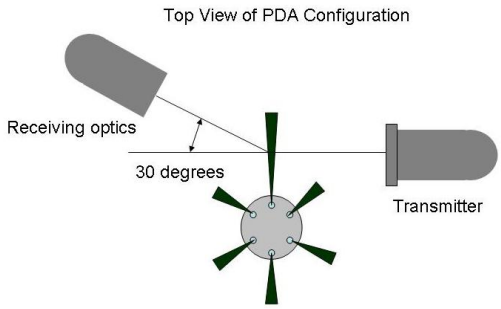

Figure 3.8 PDA configuration

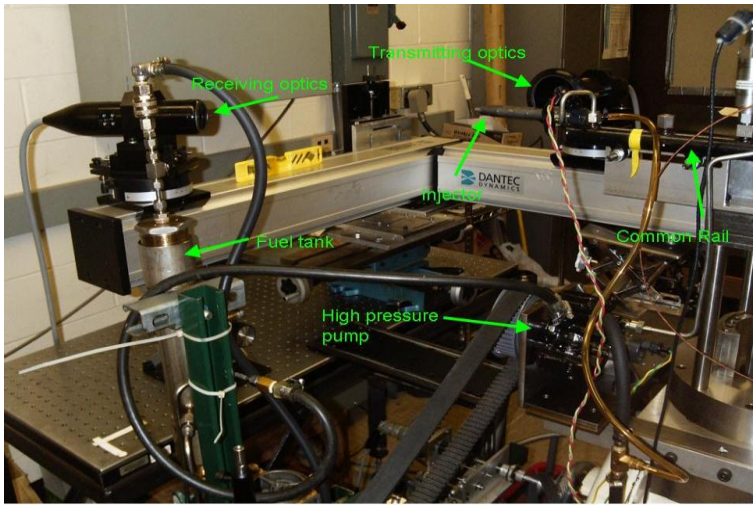

Figure 3.9 Experimental Setup

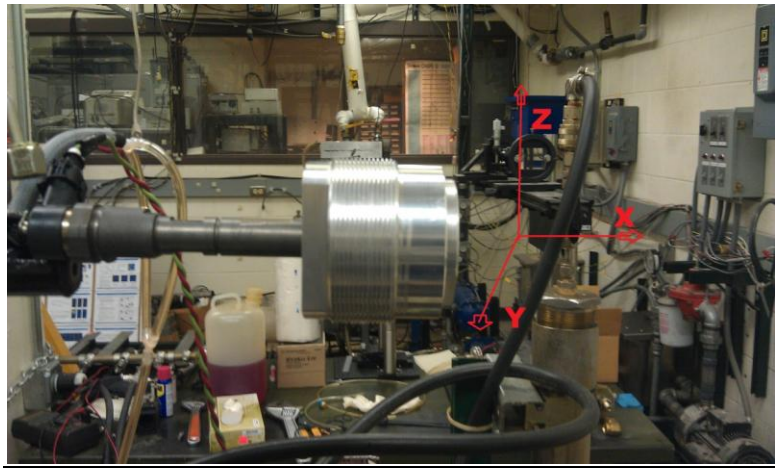

Figure 3.10 Orientation of the injector setup for the PDA measurement indicating the direction of axes

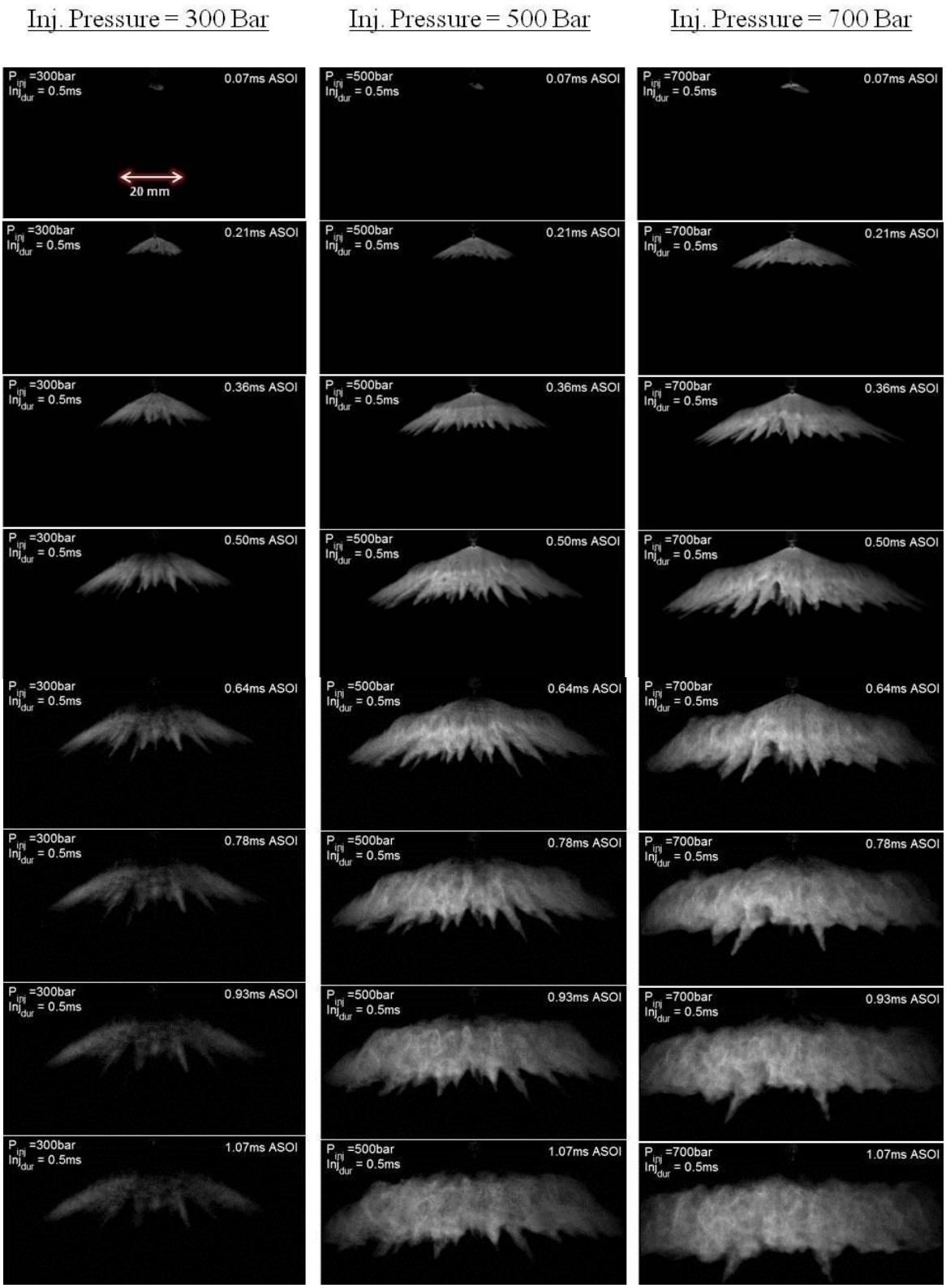

Figure 4.1 MVCO Injector Spray Evolution (Side view)

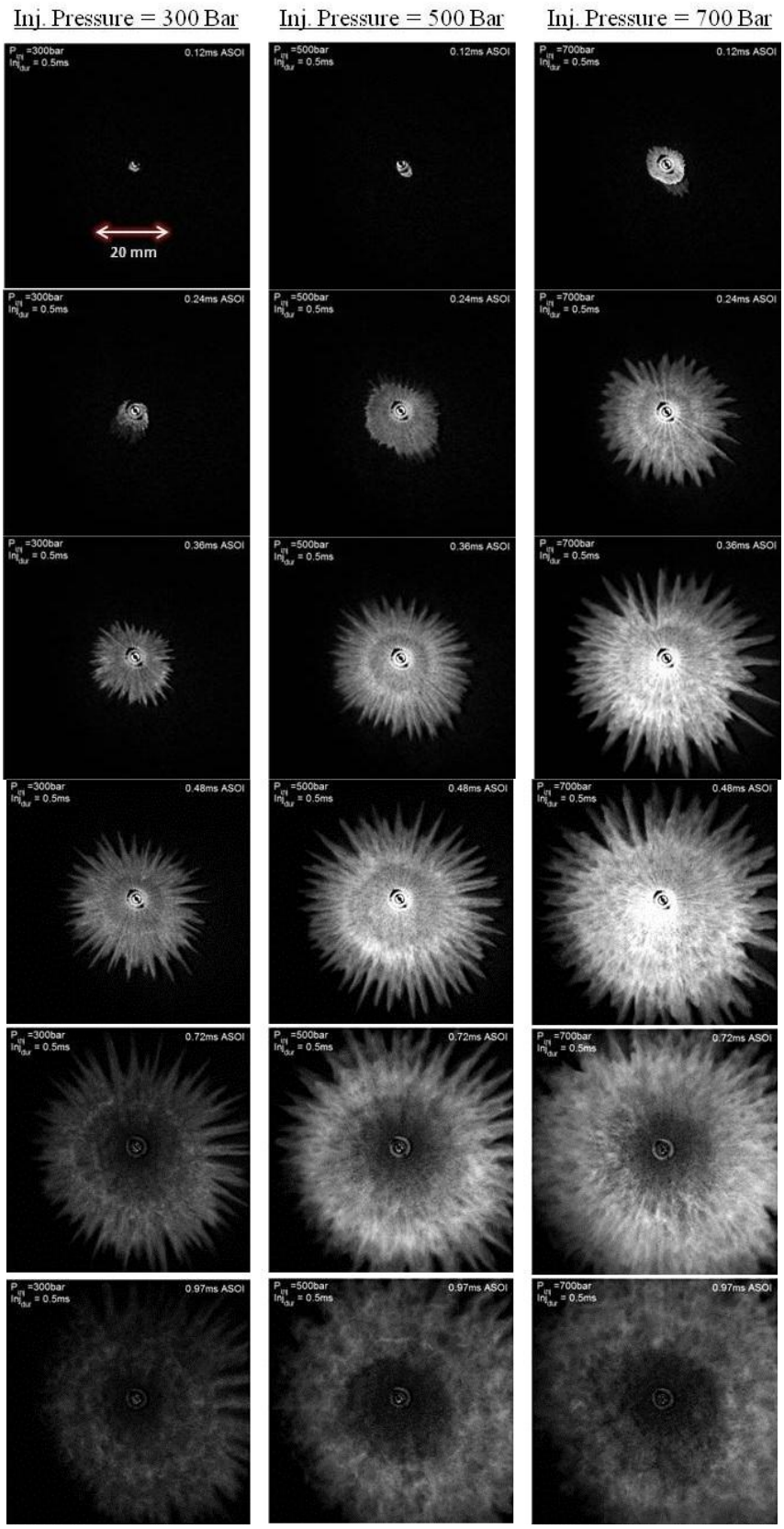

Figure 4.2 MVCO Injector Spray Evolution (Bottom View)

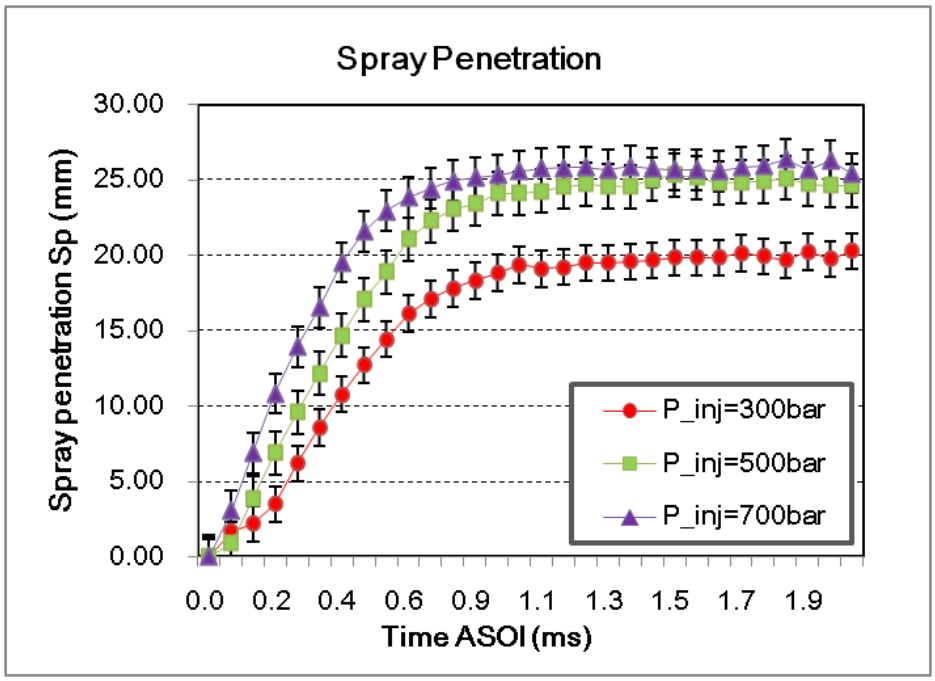

Figure 4.3 Spray Penetration Length at different injection pressures

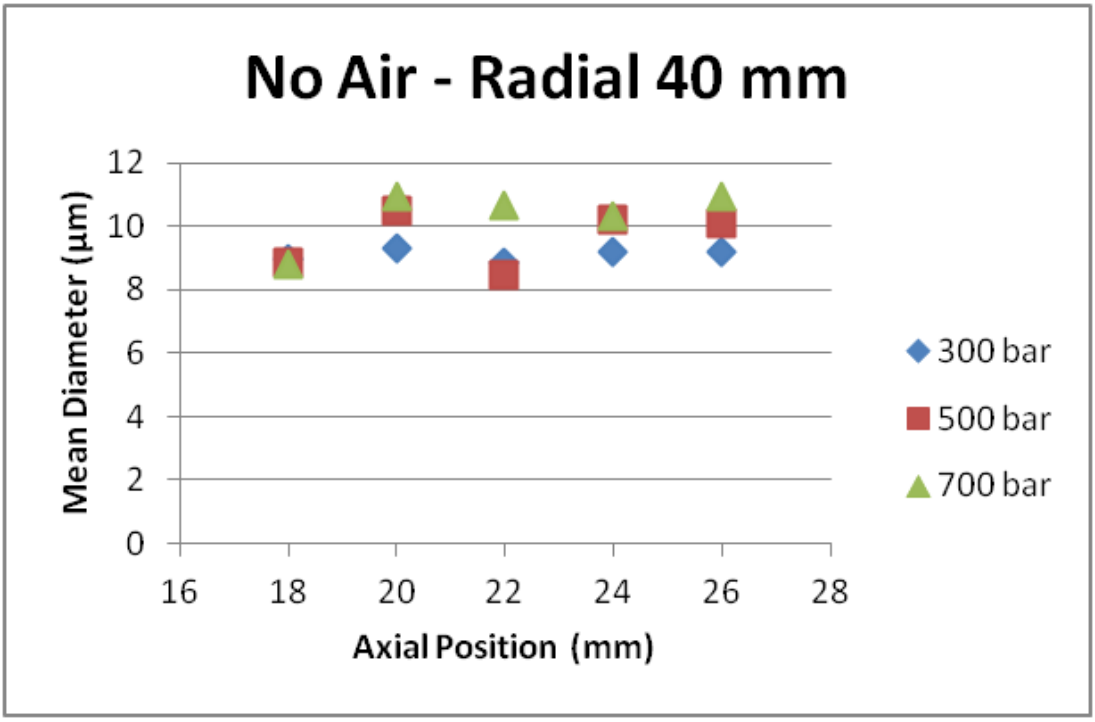

(a)

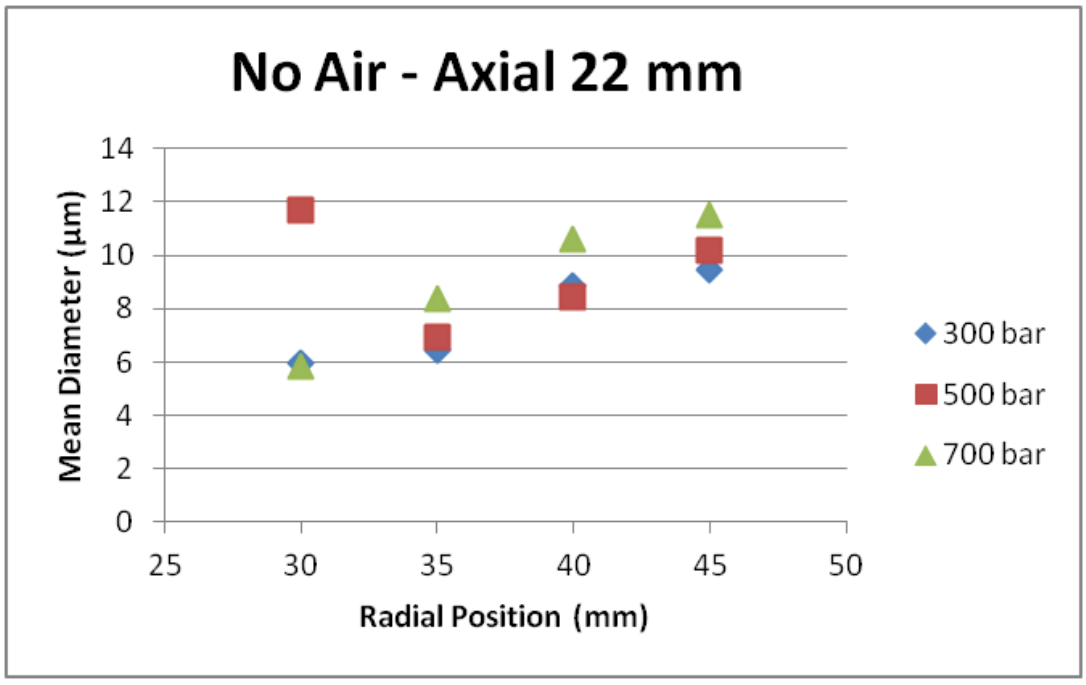

(b)

Figure 4.4 Mean droplet diameter (a) Axial trend at radial position of 40 mm (b) Radial trend at axial position of 22 mm

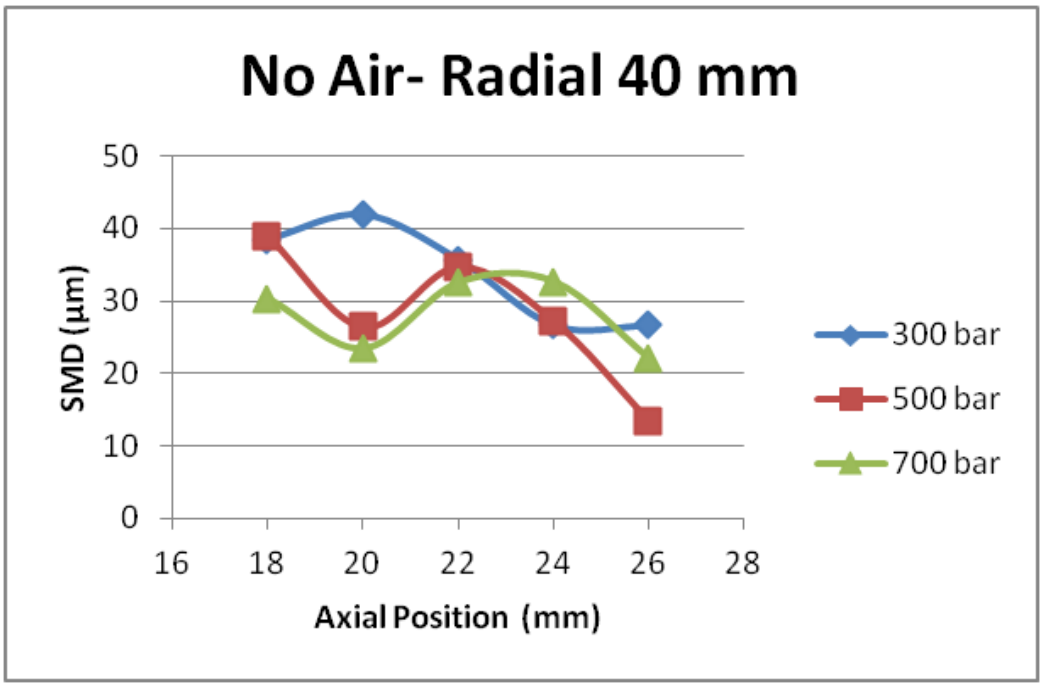

(a)

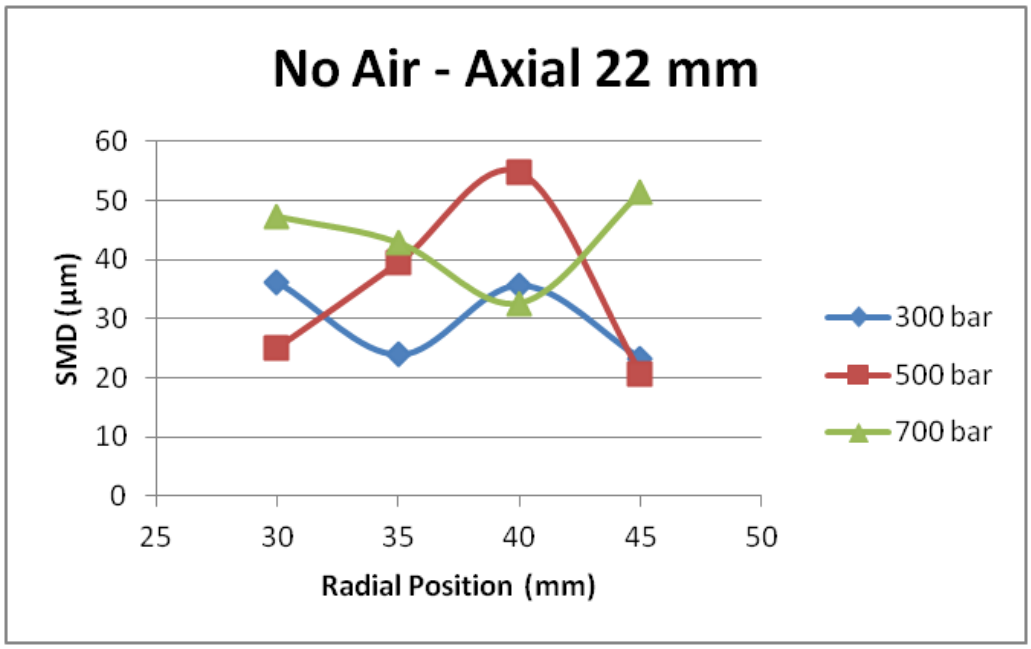

(b)

Figure 4.5 Sauter Mean Diameter (SMD) (a) Axial trend at radial position of 40 mm (b) Radial trend at axial position of 22 mm

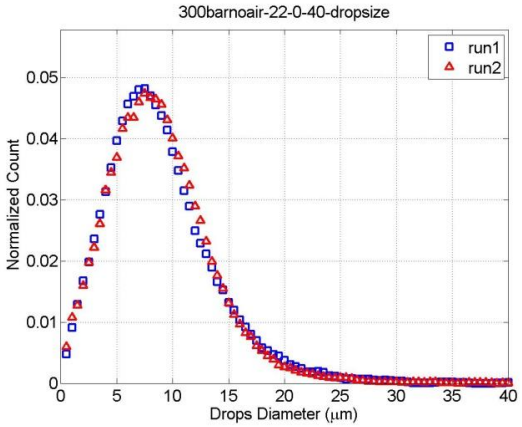

(a)

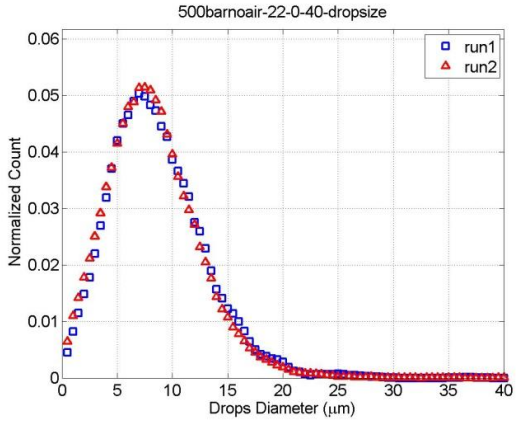

(b)

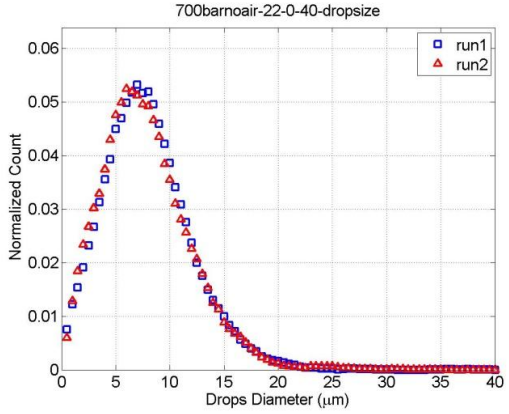

(c)

Figure 4.6 PDF of the droplet size at axial 22 mm, radial 40 mm at injection pressure (a) 300 bar (b) 500 bar (c) 700 bar

300 bar - No air

<--- Radial Position (mm) --->

	45	40	35	30	0	30	35	40	45
45					23.336				
40					35.6612				
35					24.022				
30					36.171				
0	23.336	35.6612	24.022	36.171		36.171	24.022	35.6612	23.336
30					36.171				
35					24.022				
40					35.6612				
45					23.336				

500 bar - No air

<--- Radial Position (mm) --->

	45	40	35	30	0	30	35	40	45
45					20.5429				
40					54.7294				
35					39.5298				
30					25.0761				
0	20.5429	54.7294	39.5298	25.0761		25.0761	39.5298	54.7294	20.5429
30					25.0761				
35					39.5298				
40					54.7294				
45					20.5429				

700 bar - No air

<--- Radial Position (mm) --->

	45	40	35	30	0	30	35	40	45
45					51.392				
40					32.5868				
35					42.7956				
30					47.2183				
0	51.392	32.5868	42.7956	47.2183		47.2183	42.7956	32.5868	51.392
30					47.2183				
35					42.7956				
40					32.5868				
45					51.392				

Figure 4.7 SMD Distribution at axial position of 22 mm at injection pressure 300 bar (top), 500 bar (middle) and 700 bar (bottom)

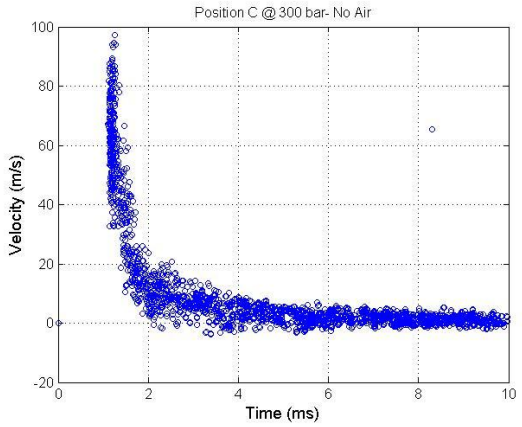

(a)

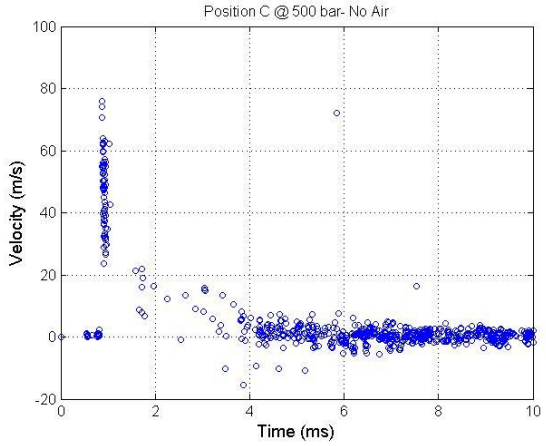

(b)

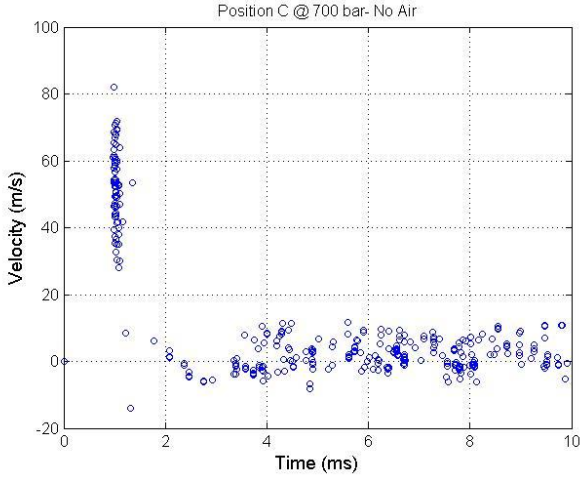

(c)

Figure 4.8 Droplet Velocities - Position C, injection pressure (a) 300 bar (b) 500 bar (c) 700 bar

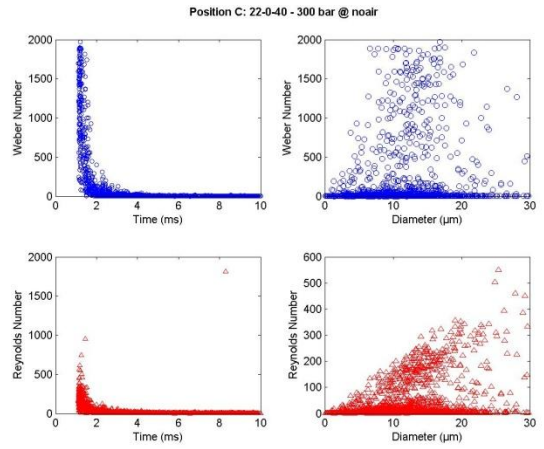

(a)

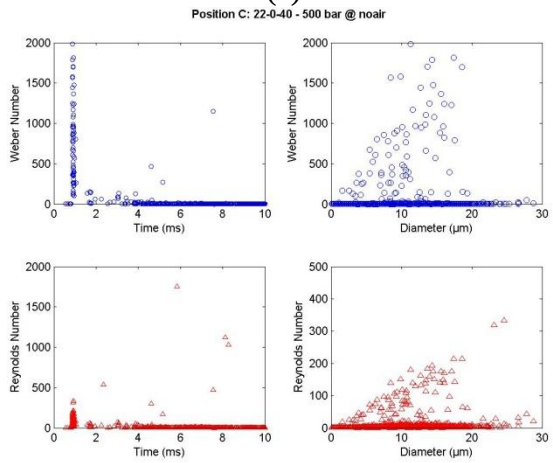

(b)

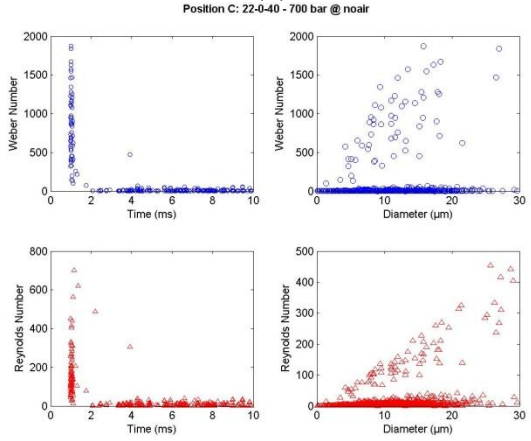

(c)

Figure 4.9 Weber No. and Reynolds No. at Position C at injection pressure (a) 300 bar (b) 500 bar (c) 700 bar

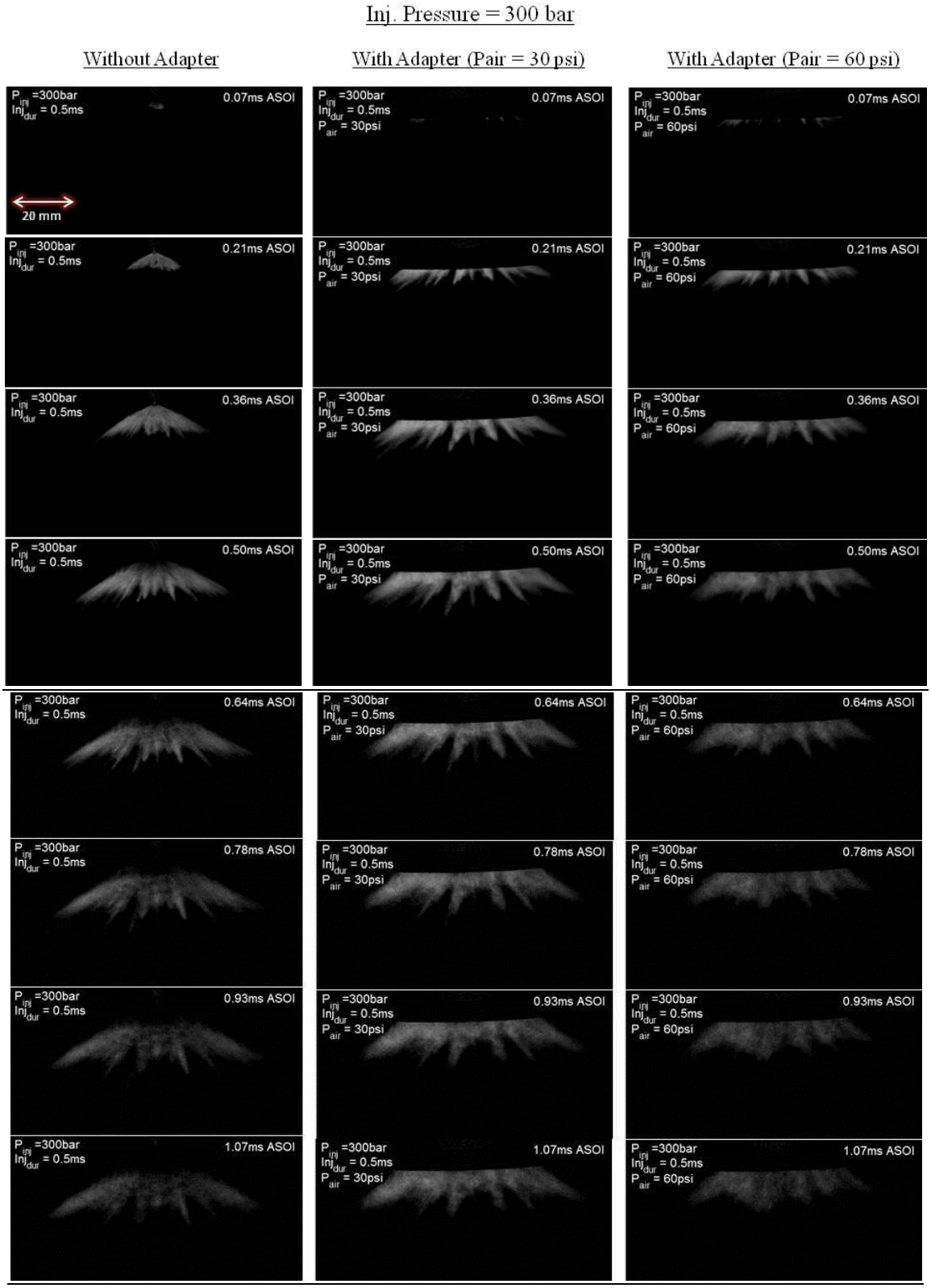

Figure 4.10 MVCO Injector with Swirl Adapter - Spray Evolution comparison at Inj. Pressure = 300 bar and Pair = 30 psi & 60 psi (Side View)

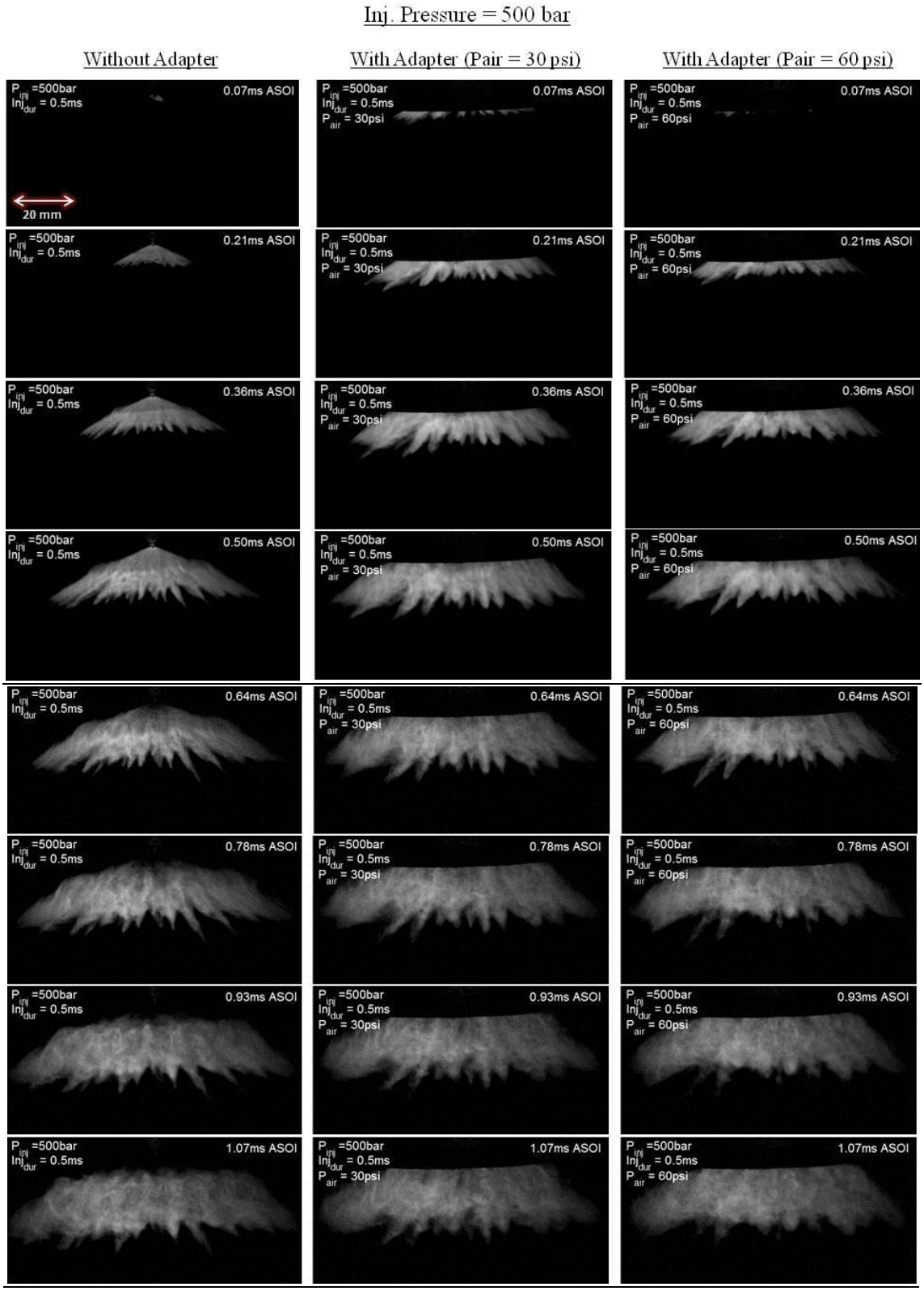

Figure 4.11 MVCO Injector with Swirl Adapter - Spray Evolution comparison at Inj. Pressure = 500 bar and Pair = 30 psi & 60 psi (Side View)

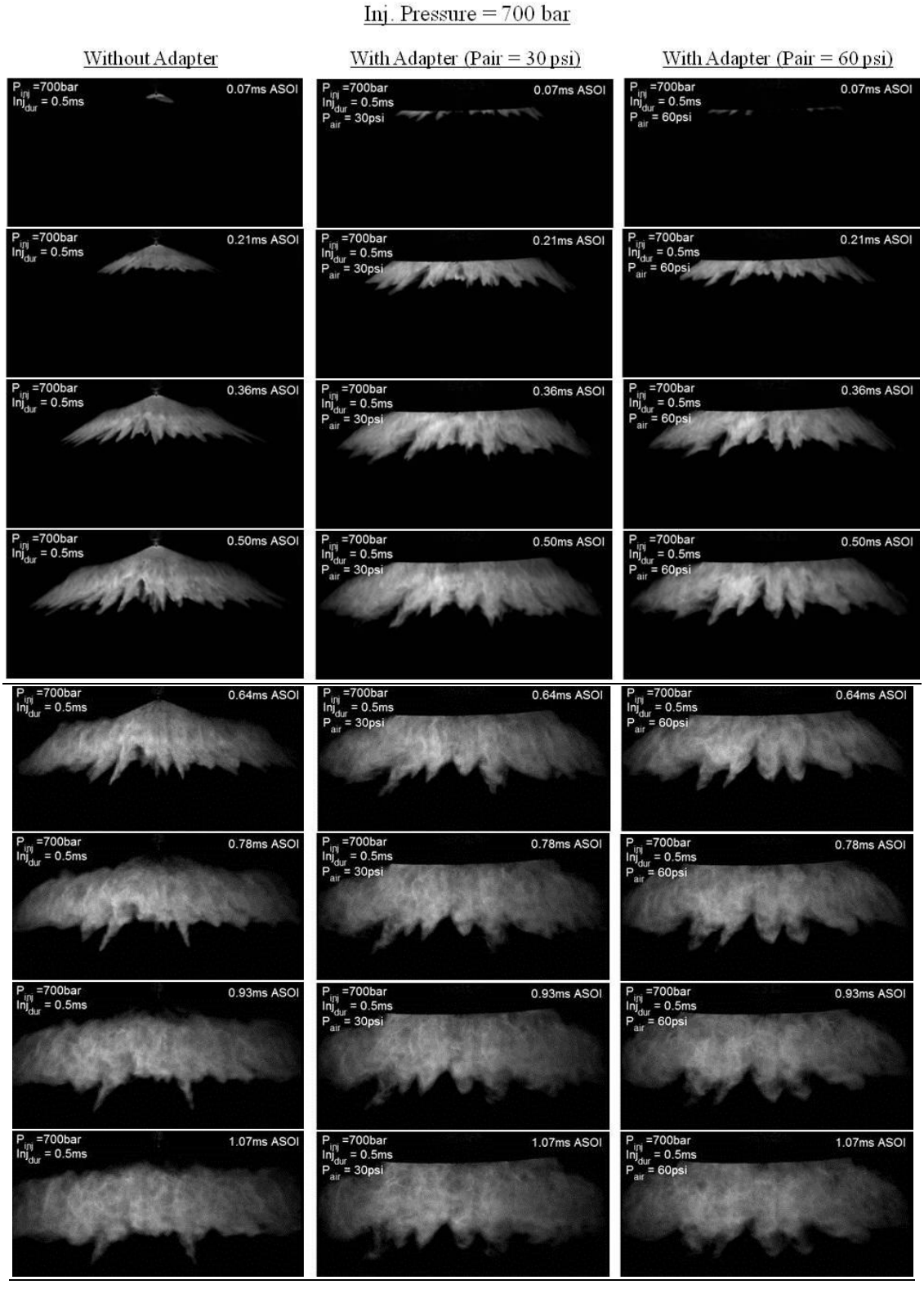

Figure 4.12 MVCO Injector with Swirl Adapter - Spray Evolution comparison at Inj. Pressure = 700 bar and Pair = 30 psi & 60 psi (Side View)

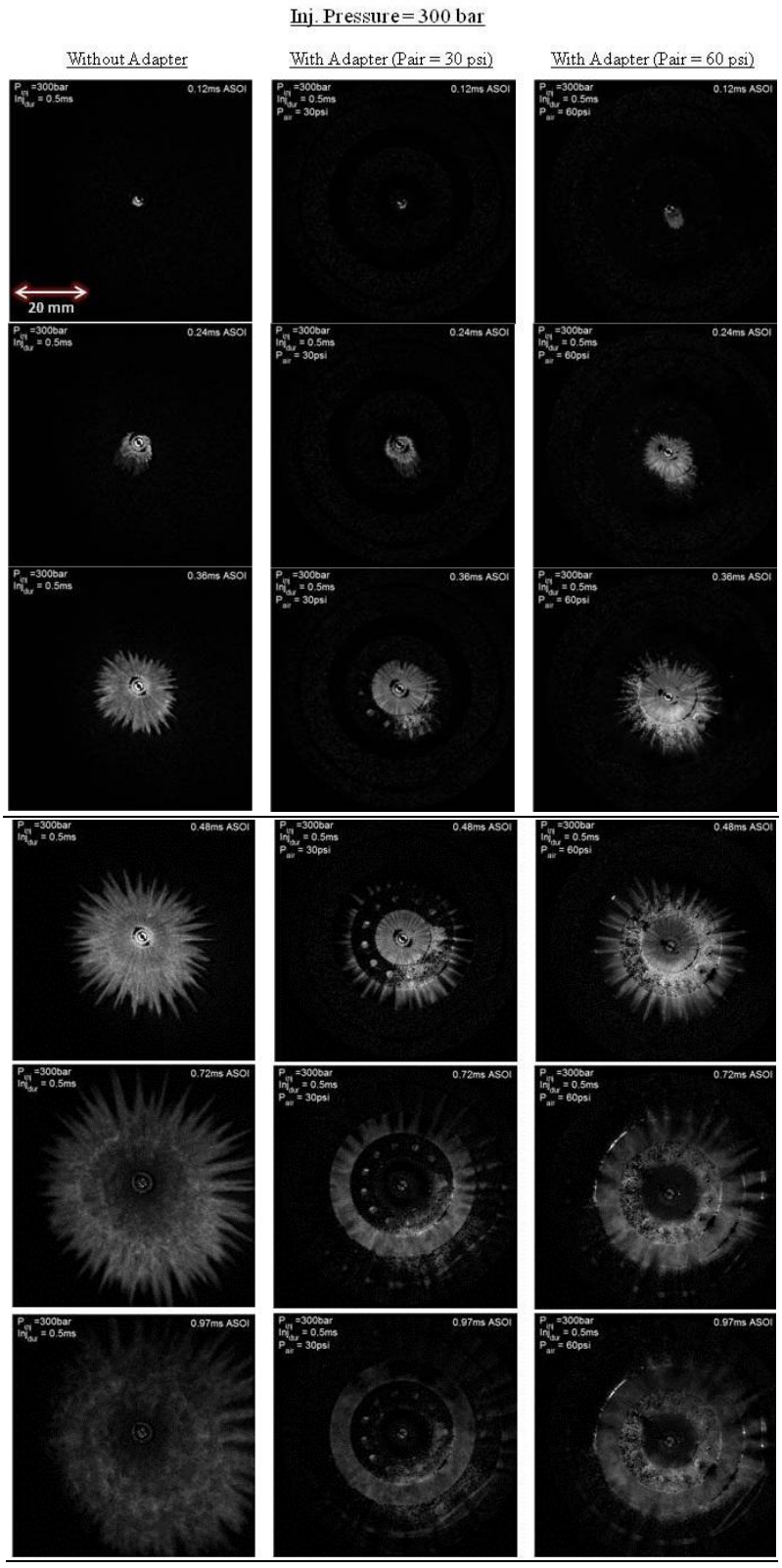

Figure 4.13 MVCO Injector with Swirl Adapter - Spray Evolution comparison at Inj. Pressure = 300 bar and Pair = 30 psi & 60 psi (Bottom View)

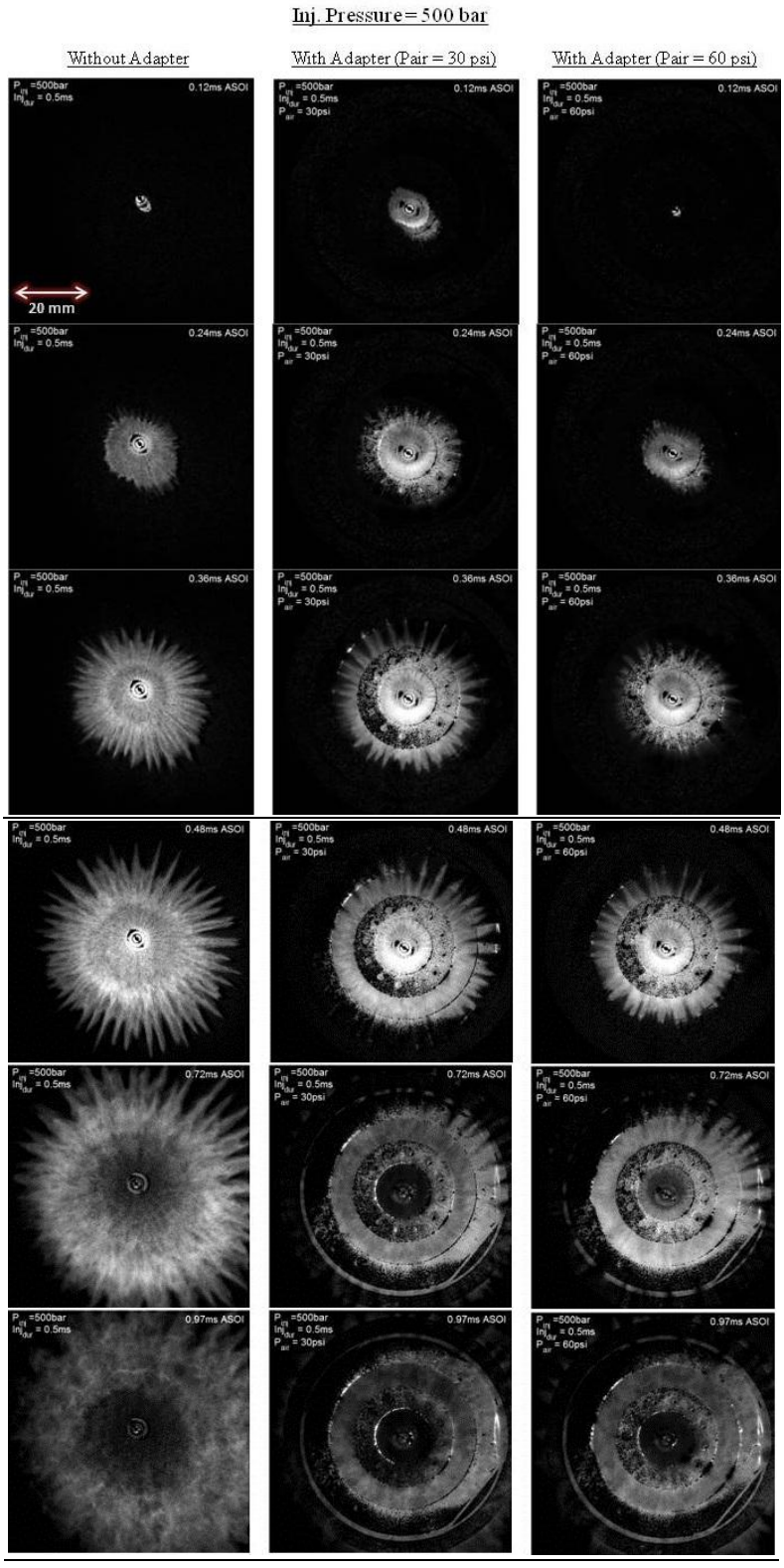

Figure 4.14 MVCO Injector with Swirl Adapter - Spray Evolution comparison at Inj. Pressure = 500 bar and Pair = 30 psi & 60 psi (Bottom View)

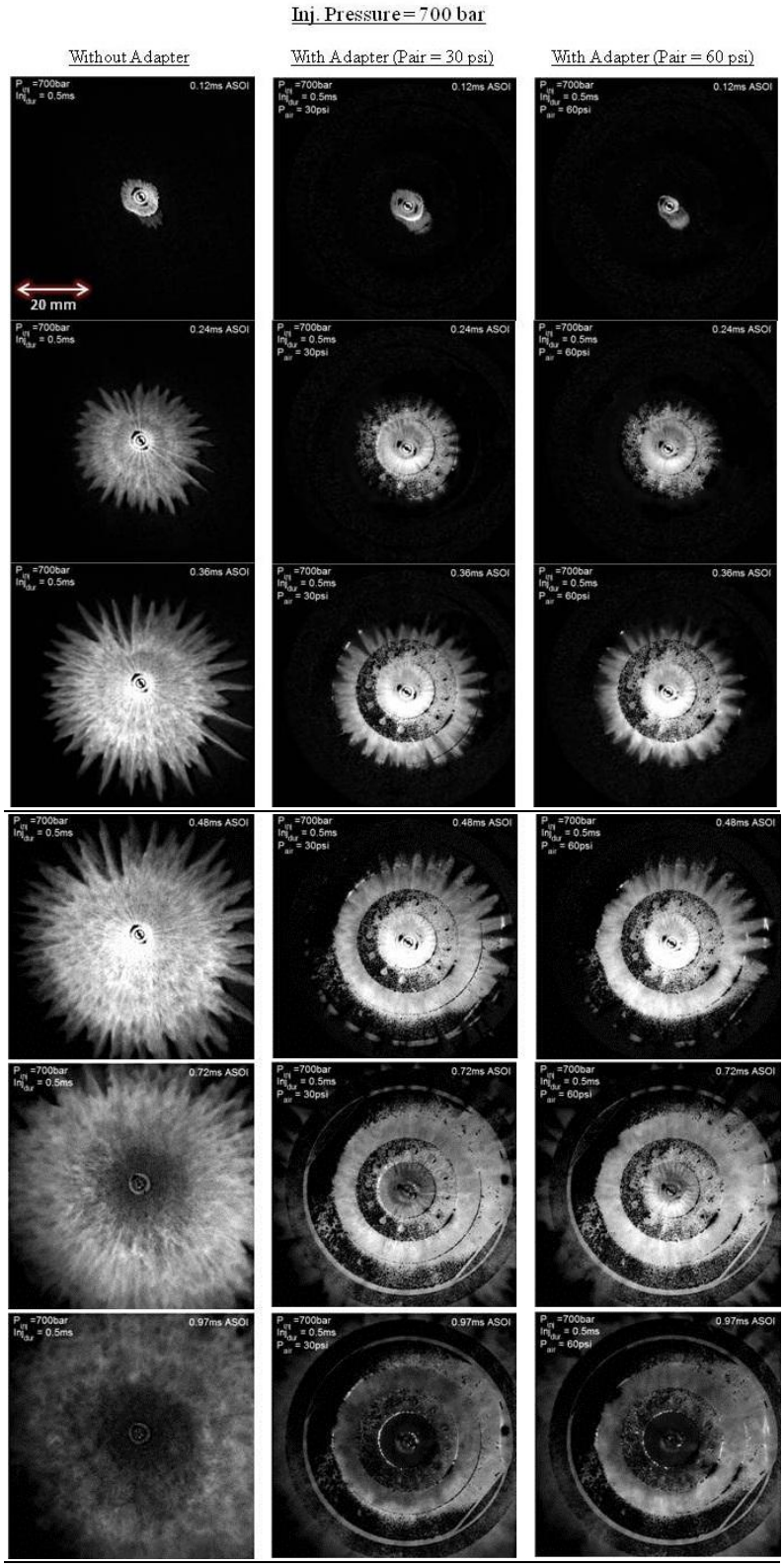

Figure 4.15 MVCO Injector with Swirl Adapter - Spray Evolution comparison at Inj. Pressure = 700 bar and Pair = 30 psi & 60 psi (Bottom View)

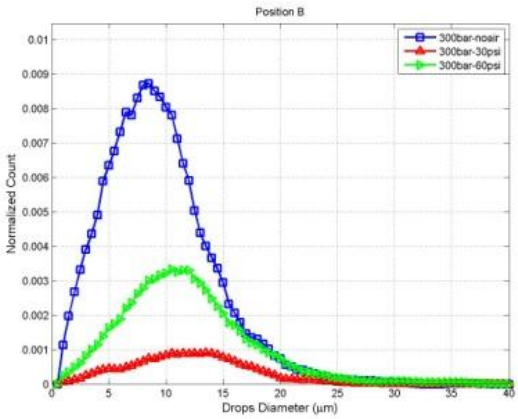

(a)

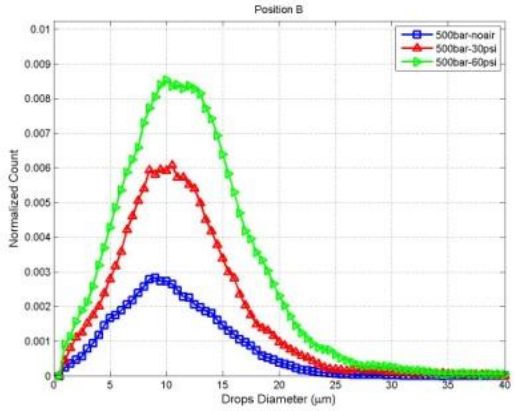

(b)

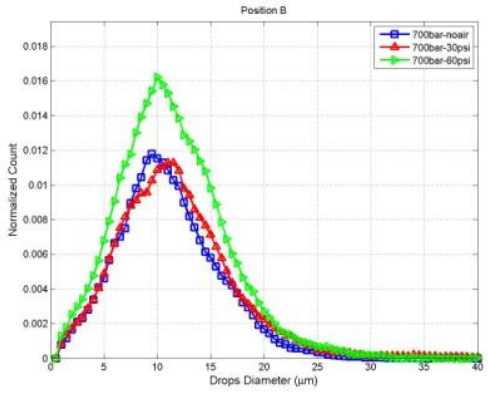

(c)

Figure 4.16 Drop size PDF at various inlet air pressures at injection pressure (a) 300 bar (b) 500 bar (c) 700 bar

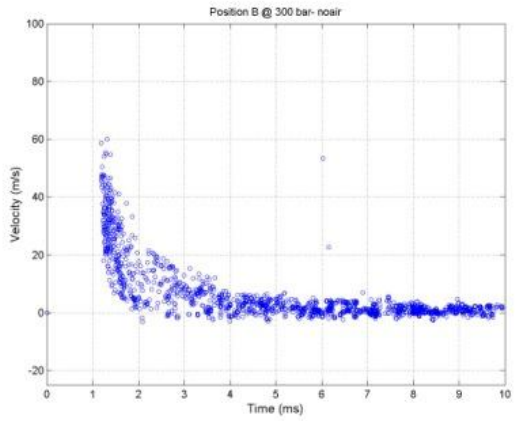

(a)

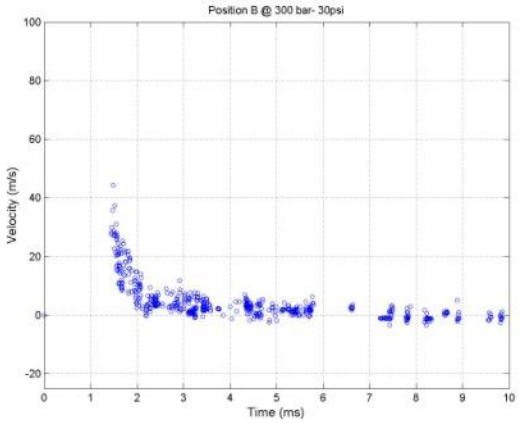

(b)

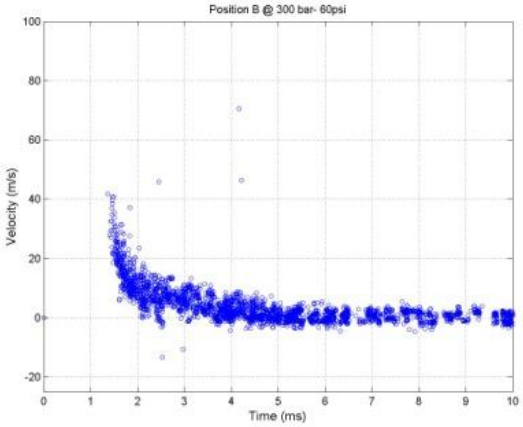

(c)

Figure 4.17 Droplet Velocities at Position B at injection pressure 300 bar with inlet air pressure (a) 0 psi (b) 30 psi (c) 60 psi

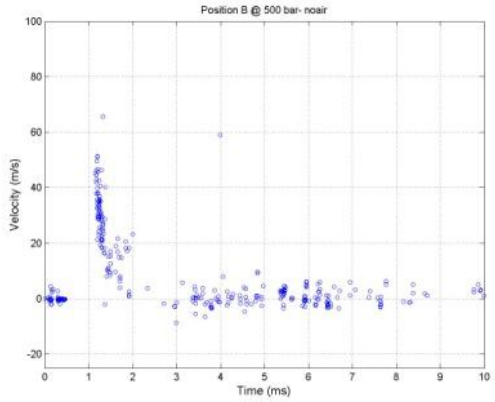

(a)

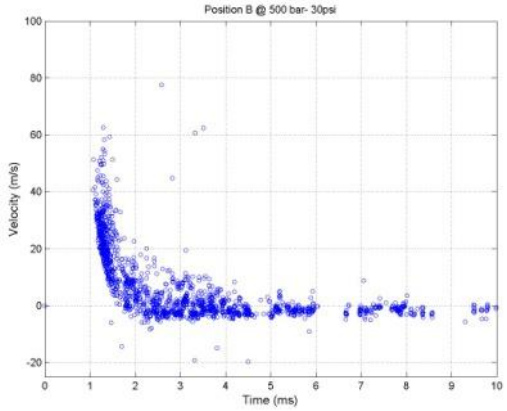

(b)

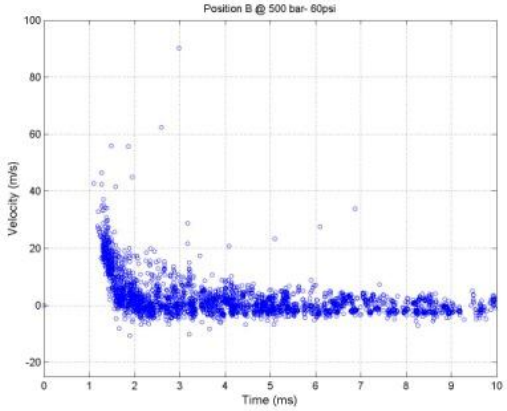

(c)

Figure 4.18 Droplet Velocities at Position B at injection pressure 500 bar with inlet air pressure (a) 0 psi (b) 30 psi (c) 60 psi

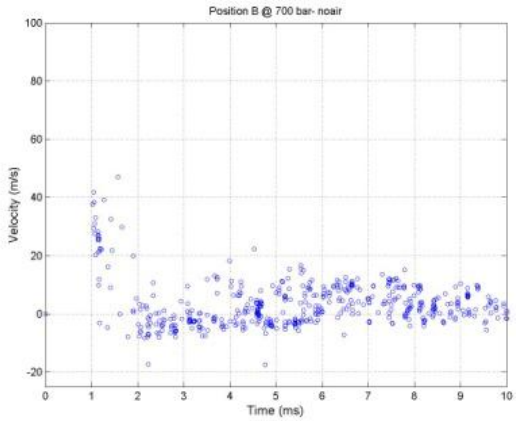

(a)

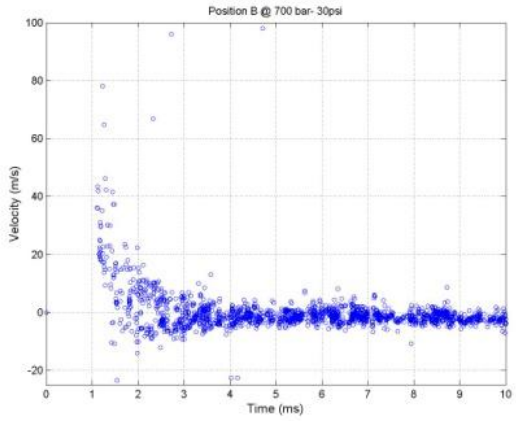

(b)

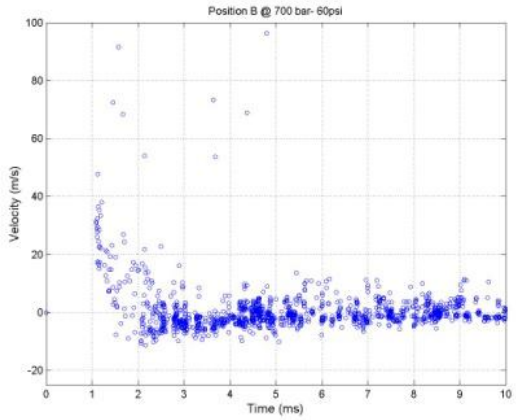

(c)

Figure 4.19 Droplet Velocities at Position B at injection pressure 500 bar with inlet air pressure (a) 0 psi (b) 30 psi (c) 60 psi

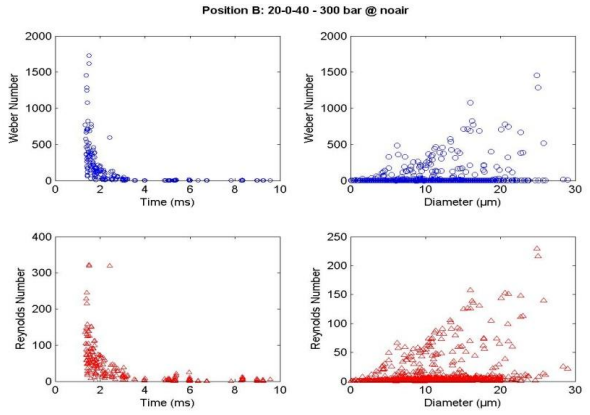

(a)

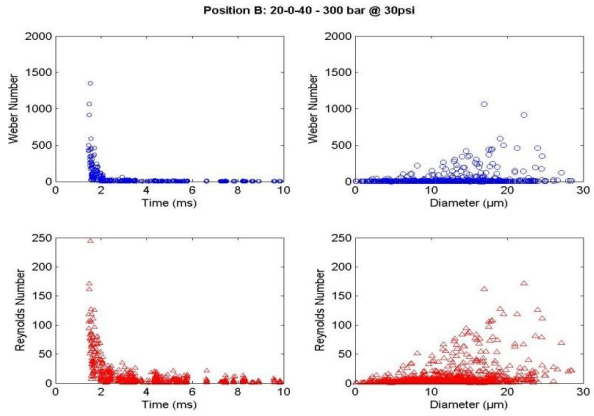

(b)

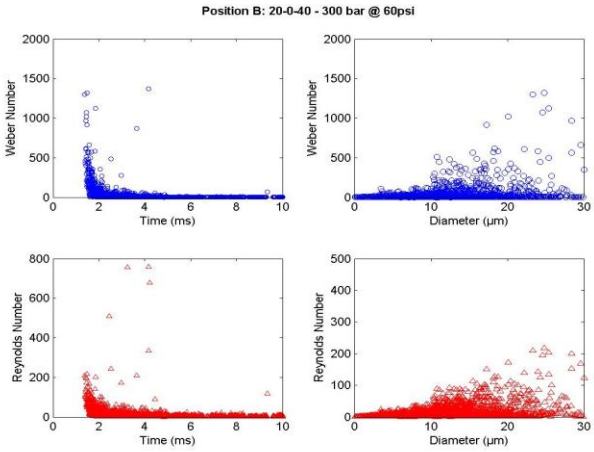

(c)

Figure 4.20 Weber Number (blue) and Reynolds Number (red) at Position B at Pinj = 300 bar (a) 0 psi (b) 30 psi (c) 60 psi

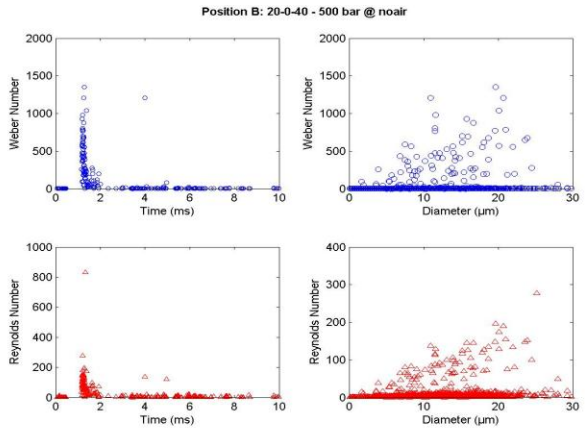

(a)

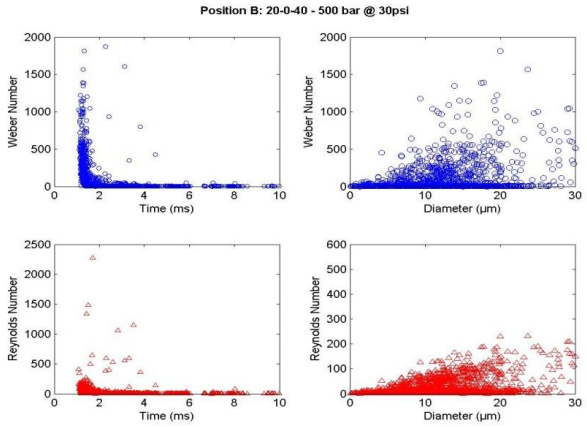

(b)

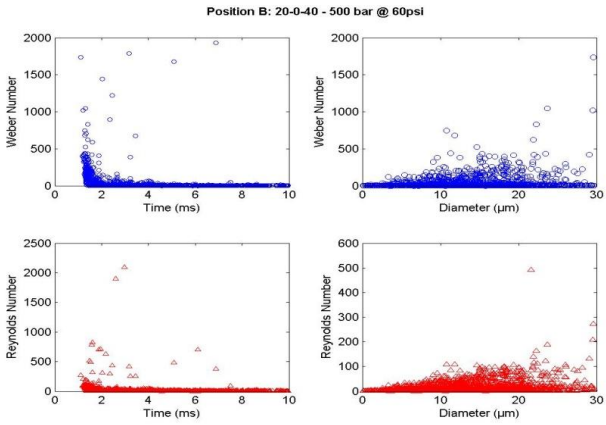

(c)

Figure 4.21 Weber Number (blue) and Reynolds Number (red) at Position B at Pinj = 500 bar (a) 0 psi (b) 30 psi (c) 60 psi

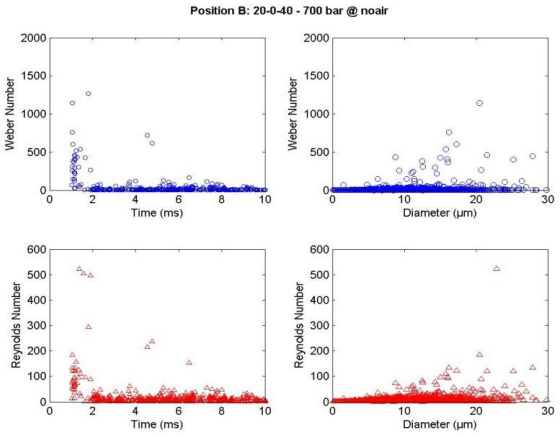

(a)

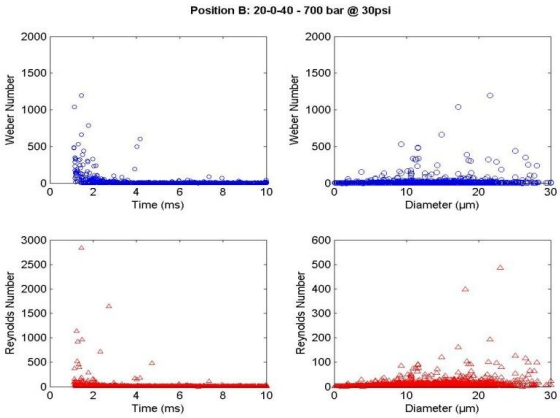

(b)

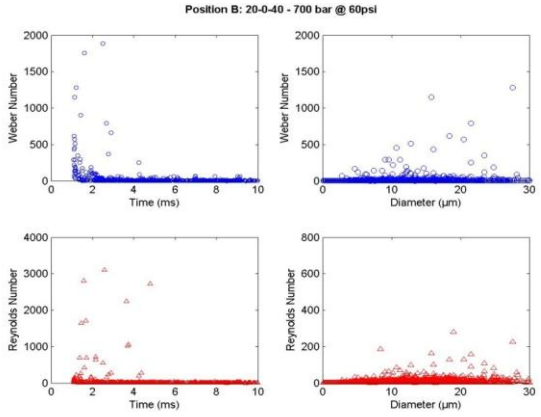

(c)

Figure 4.22 Weber Number (blue) and Reynolds Number (red) at Position B at Pinj = 700 bar (a) 0 psi (b) 30 psi (c) 60 psi

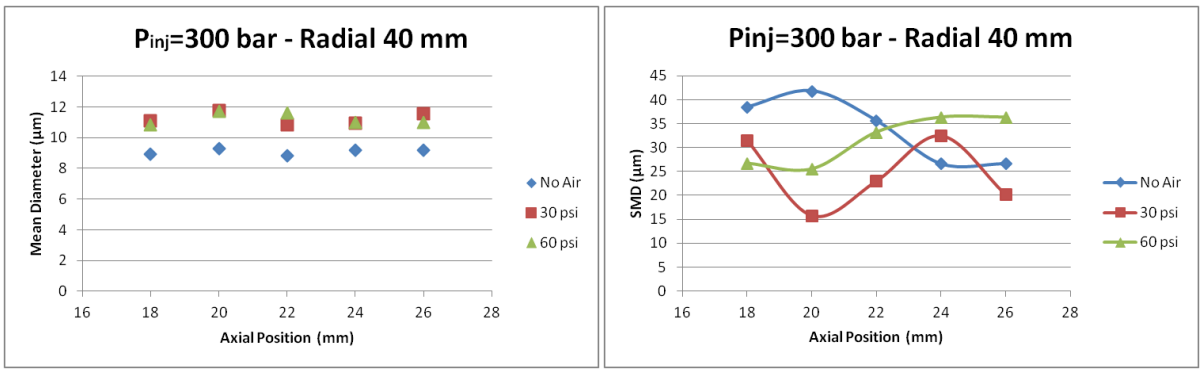

(a)

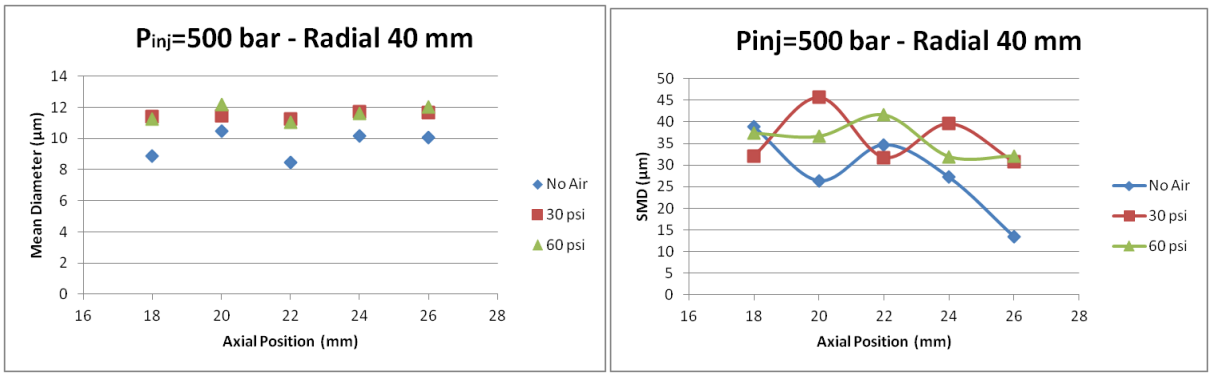

(b)

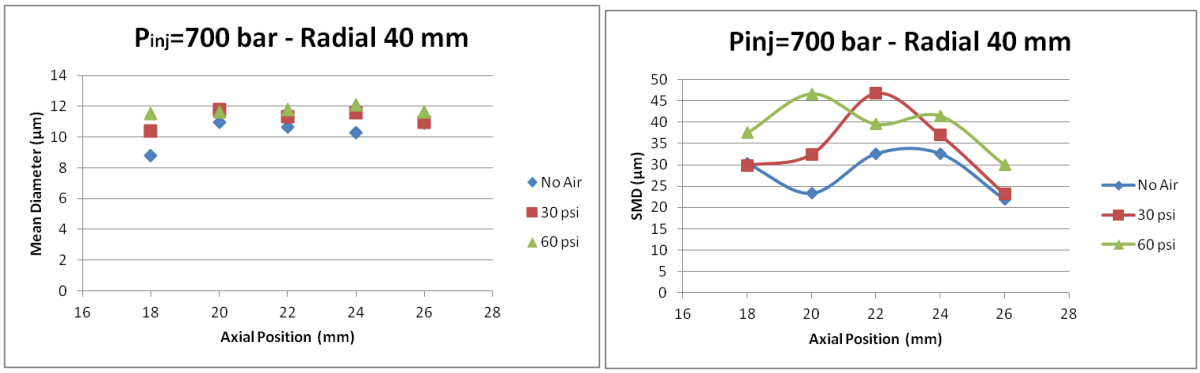

(c)

Figure 4.23 Mean diameter (left) and SMD (right) trend (showing air impact) with Axial and radial positions – (a) Pinj = 300 bar (b) Pinj = 500 bar (c) Pinj = 700 bar

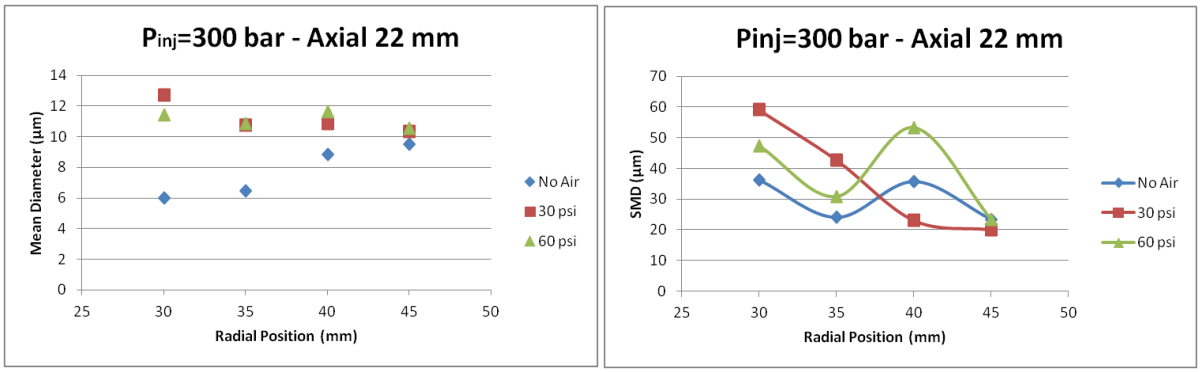

(a)

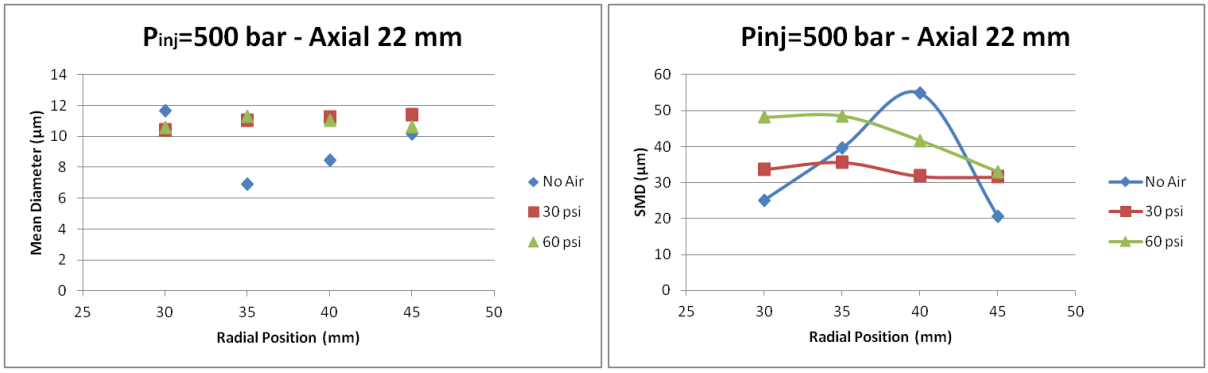

(b)

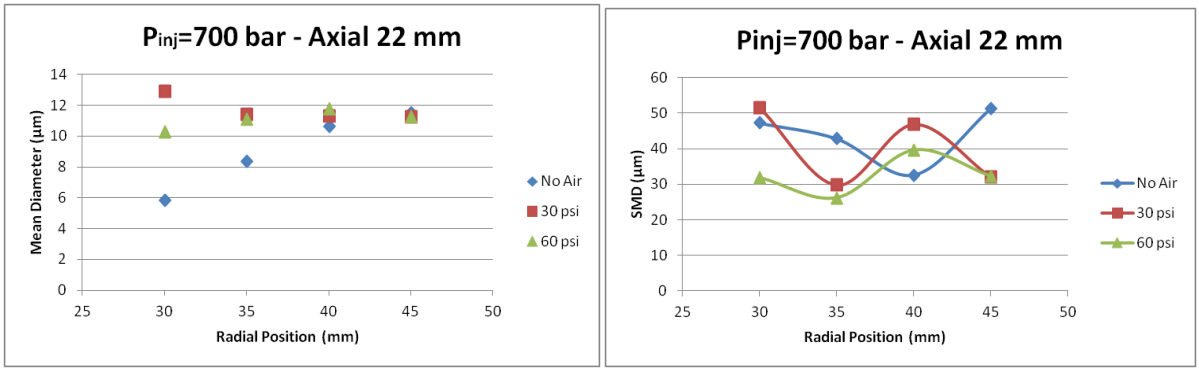

(c)

Figure 4.24 Mean Diameter (left) and SMD (right) trends (showing air impact) with Axial and radial positions – (a) Pinj = 300 bar (b) Pinj = 500 bar (c) Pinj = 700 bar

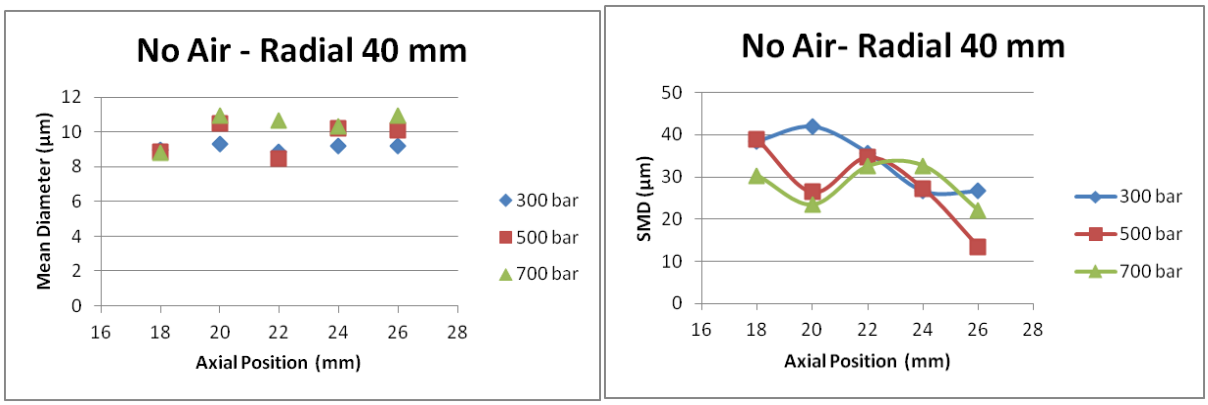

(a)

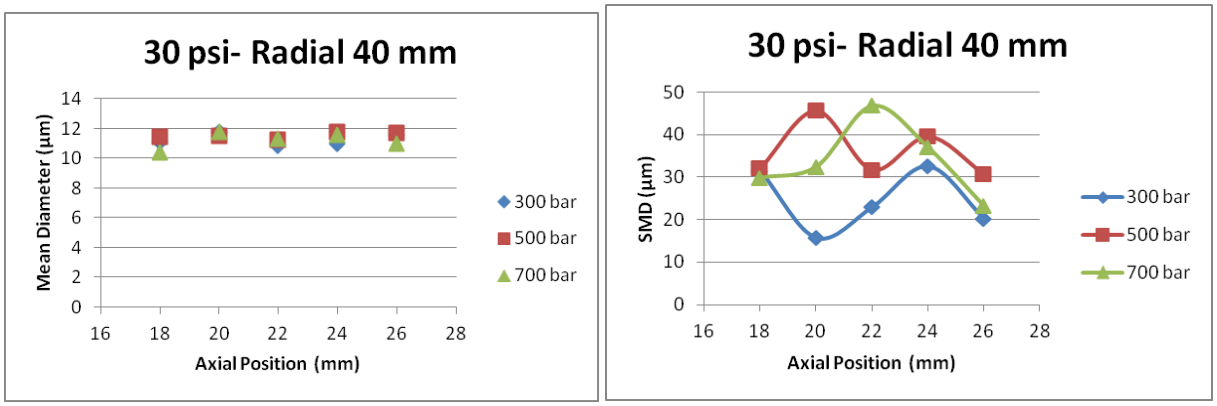

(b)

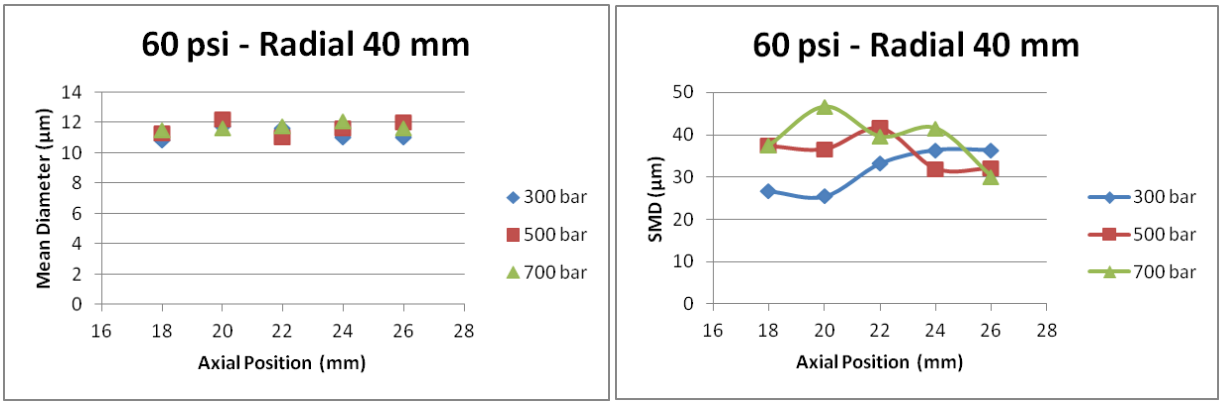

(c)

Figure 4.25 Mean diameter (left) and SMD (right) trend (showing Pinj impact) with Axial and radial positions – (a) No air (b) Pair = 30 psi (c) Pair = 60 psi

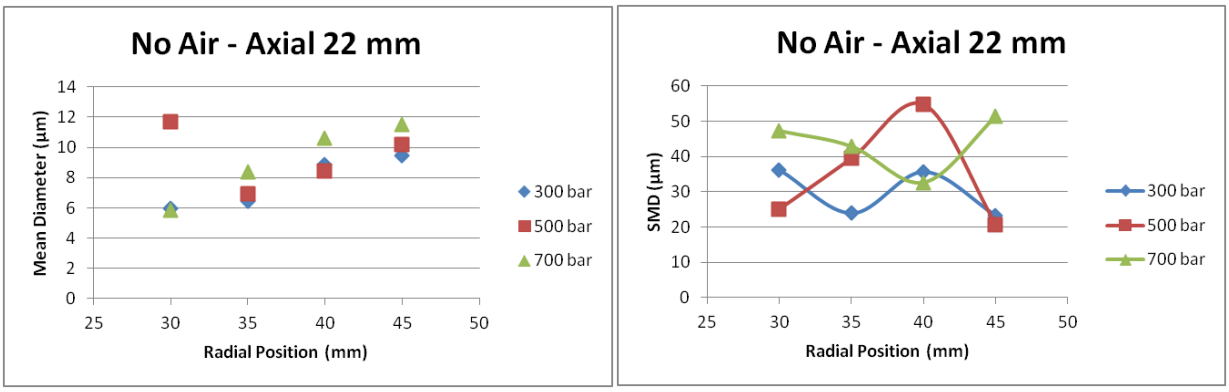

(a)

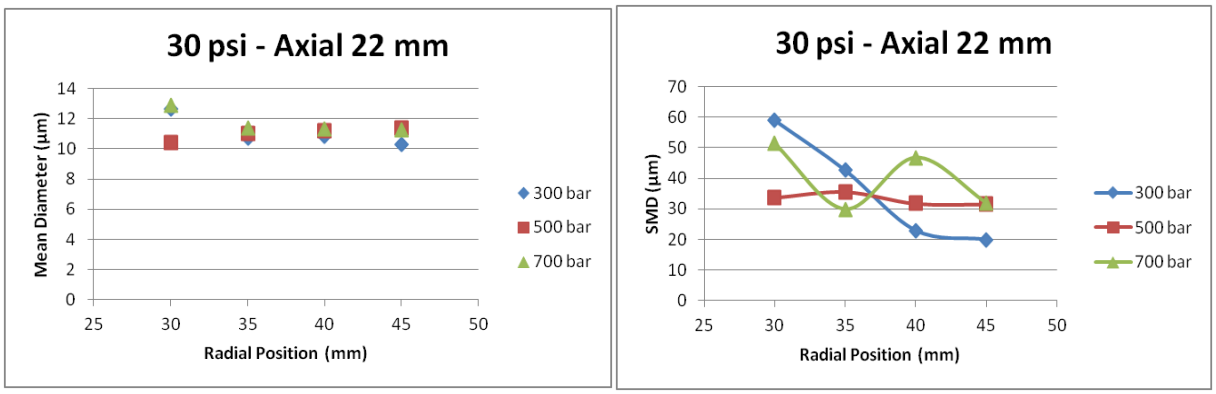

(b)

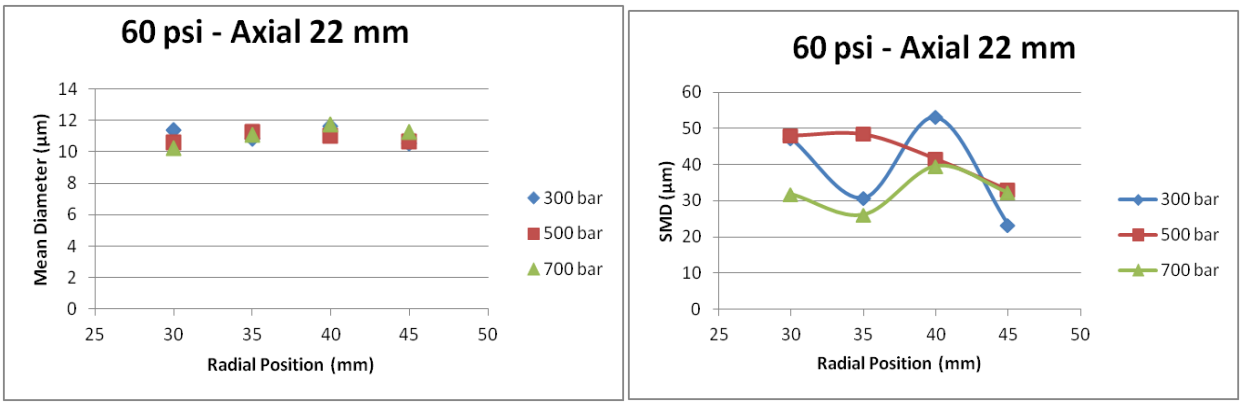

(c)

Figure 4.26 Mean Diameter (left) and SMD (right) trend (showing injection pressure impact) with axial and radial positions – (a) No air (b) Pair = 30 psi (c) Pair = 60 psi

300 bar - No air	<--- Radial Position (mm) --->								
	45	40	35	30	0	30	35	40	45
45					23.3				
40					35.7				
35					24				
30					36.2				
0	23.3	35.7	24	36.2		36.2	24	35.7	23.3
30					36.2				
35					24				
40					35.7				
45					23.3				

300 bar - 30 psi	<--- Radial Position (mm) --->								
	45	40	35	30	0	30	35	40	45
45					20				
40					23				
35					42.7				
30					59				
0	20	23	42.7	59		59	42.7	23	20
30					59				
35					42.7				
40					23				
45					20				

300 bar - 60 psi	<--- Radial Position (mm) --->								
	45	40	35	30	0	30	35	40	45
45					23.3				
40					53.2				
35					53.2				
30					47.3				
0	23.3	53.2	30.8	47.3		47.3	30.8	53.2	23.3
30					47.3				
35					30.8				
40					53.2				
45					23.3				

(a)

500 bar - No air	<--- Radial Position (mm) --->								
	45	40	35	30	0	30	35	40	45
45					20.5				
40					54.7				
35					39.5				
30					25.1				
0	20.5	54.7	39.5	25.1		25.1	39.5	54.7	20.5
30					25.1				
35					39.5				
40					54.7				
45					20.5				

500 bar - 30 psi	<--- Radial Position (mm) --->								
	45	40	35	30	0	30	35	40	45
45					31.5				
40					31.8				
35					35.5				
30					33.6				
0	31.5	31.8	35.5	33.6		33.6	35.5	31.8	31.5
30					33.6				
35					35.5				
40					31.8				
45					31.5				

500 bar - 60 psi	<--- Radial Position (mm) --->								
	45	40	35	30	0	30	35	40	45
45					33				
40					41.6				
35					48.5				
30					48.1				
0	33	41.6	48.5	48.1		48.1	48.5	41.6	33
30					48.1				
35					48.5				
40					41.6				
45					33				

(b)

700 bar - No air	<--- Radial Position (mm) --->								
	45	40	35	30	0	30	35	40	45
45					51.4				
40					32.6				
35					42.8				
30					47.2				
0	51.4	32.6	42.8	47.2		47.2	42.8	32.6	51.4
30					47.2				
35					42.8				
40					32.6				
45					51.4				

700 bar - 30 psi	<--- Radial Position (mm) --->								
	45	40	35	30	0	30	35	40	45
45					32				
40					46.8				
35					29.8				
30					51				
0	32	46.8	29.8	51		51	29.8	46.8	32
30					51				
35					29.8				
40					46.8				
45					32				

500 bar - 60 psi	<--- Radial Position (mm) --->								
	45	40	35	30	0	30	35	40	45
45					32.2				
40					39.6				
35					26.2				
30					31.8				
0	39.6	39.6	26.2	31.8		31.8	26.2	39.6	39.6
30					31.8				
35					26.2				
40					39.6				
45					32.2				

(c)

Figure 4.27 SMD Distribution at axial position of 22 mm – (a) Pinj = 300 bar, Pair = 0 psi, 30 psi, 60 psi (b) Pinj = 500 bar, Pair = 0 psi, 30 psi, 60 psi (c) Pinj = 700 bar, Pair = 0 psi, 30 psi, 60 psi

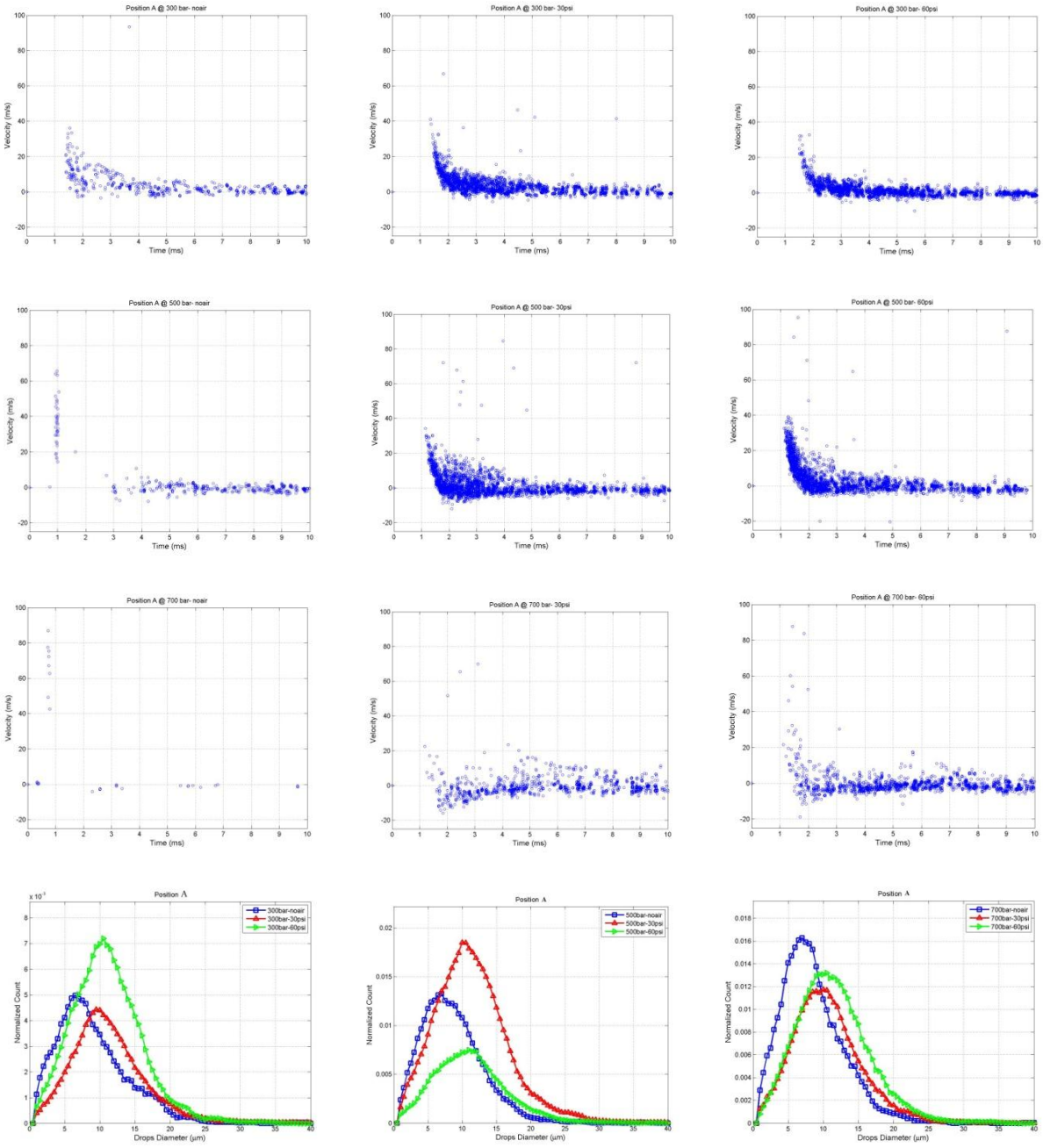

Figure 4.28 Position A (18-0-40) – Velocity and Drop size PDF at Pinj = 300 bar, 500 bar, 700 bar and Pair = 0 psi, 30 psi, 60 psi

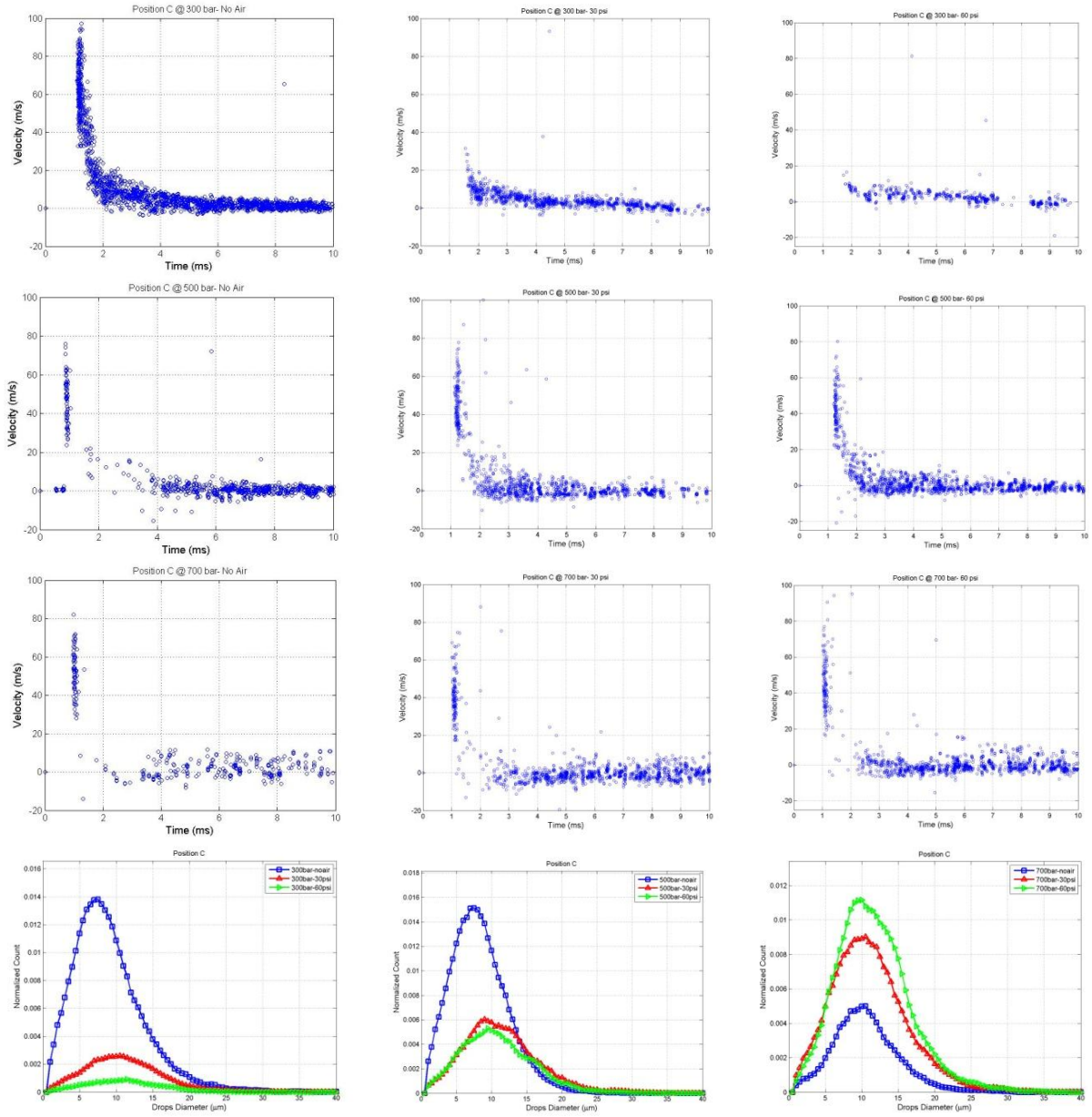

Figure 4.29 Position C (22-0-40) – Velocity and DropSize PDF at Pinj = 300 bar, 500 bar, 700 bar and Pair = 0 psi, 30 psi, 60 psi

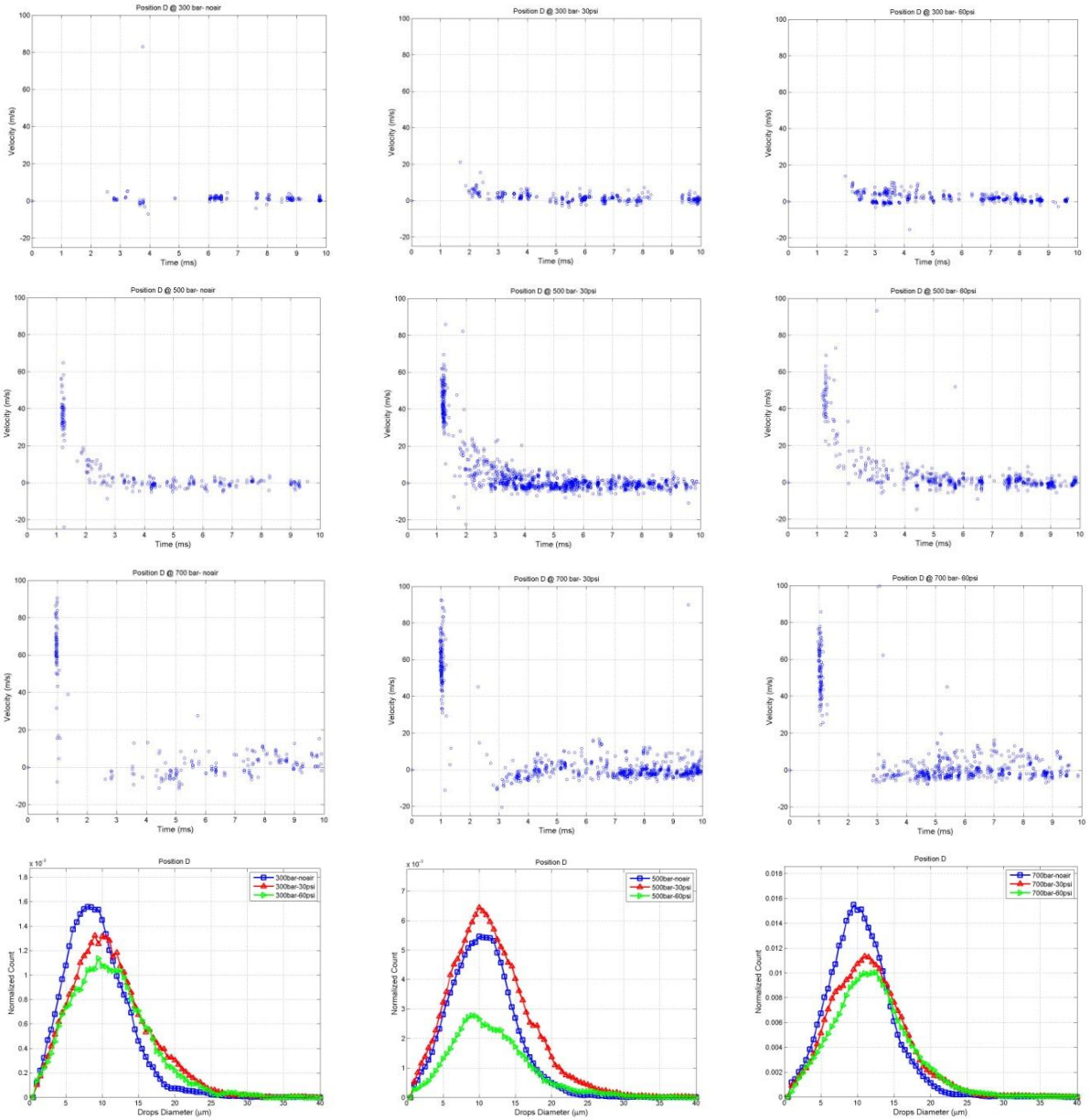

Figure 4.30 Position D (24-0-40) – Velocity and DropSize PDF at Pinj = 300 bar, 500 bar, 700 bar and Pair = 0 psi, 30 psi, 60 psi

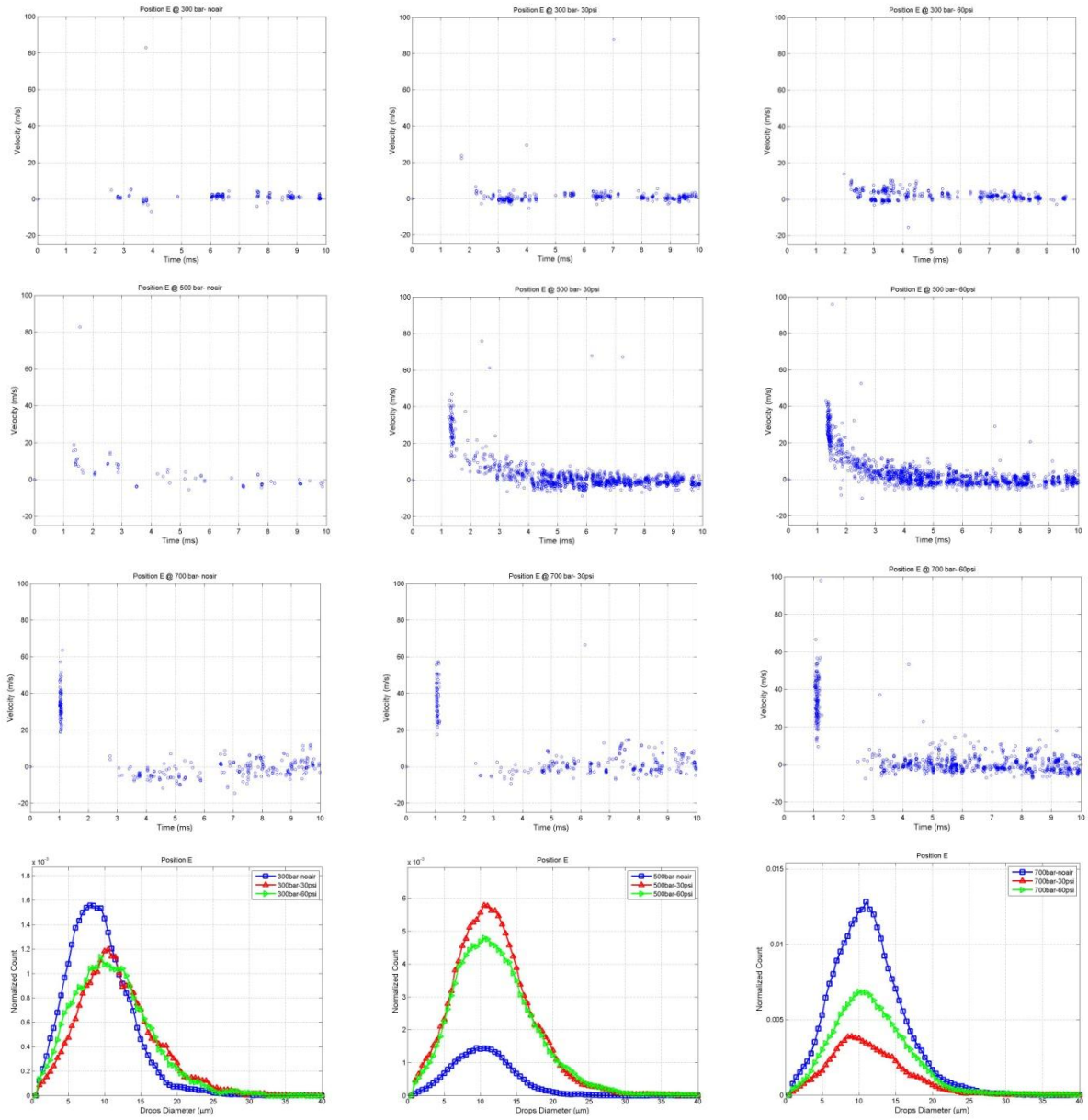

Figure 4.31 Position E (26-0-40) – Velocity and DropSize PDF at Pinj = 300 bar, 500 bar, 700 bar and Pair = 0 psi, 30 psi, 60 psi

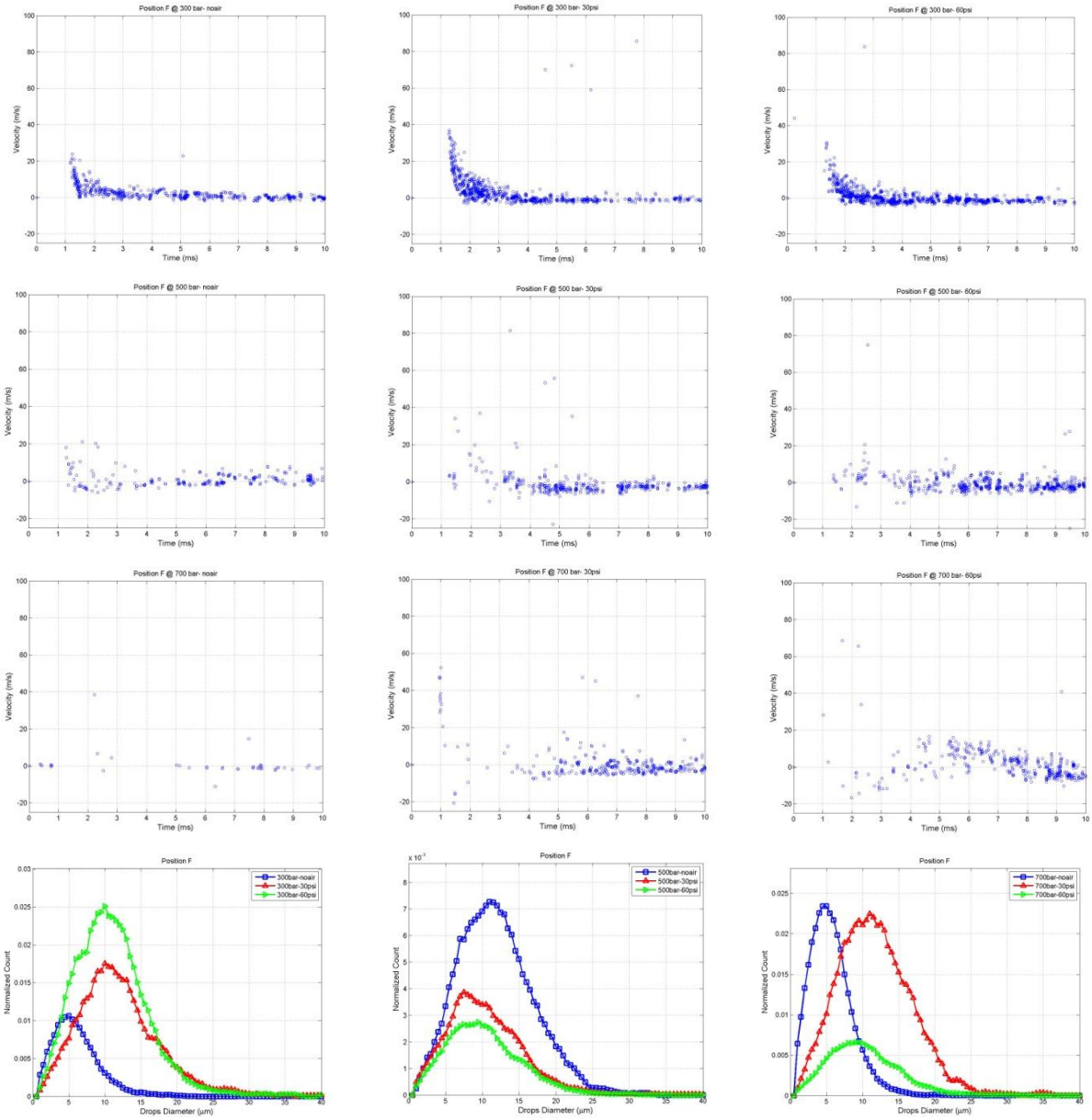

Figure 4.32 Position F (22-0-30) – Velocity and DropSize PDF at Pinj = 300 bar, 500 bar, 700 bar and Pair = 0 psi, 30 psi, 60 psi

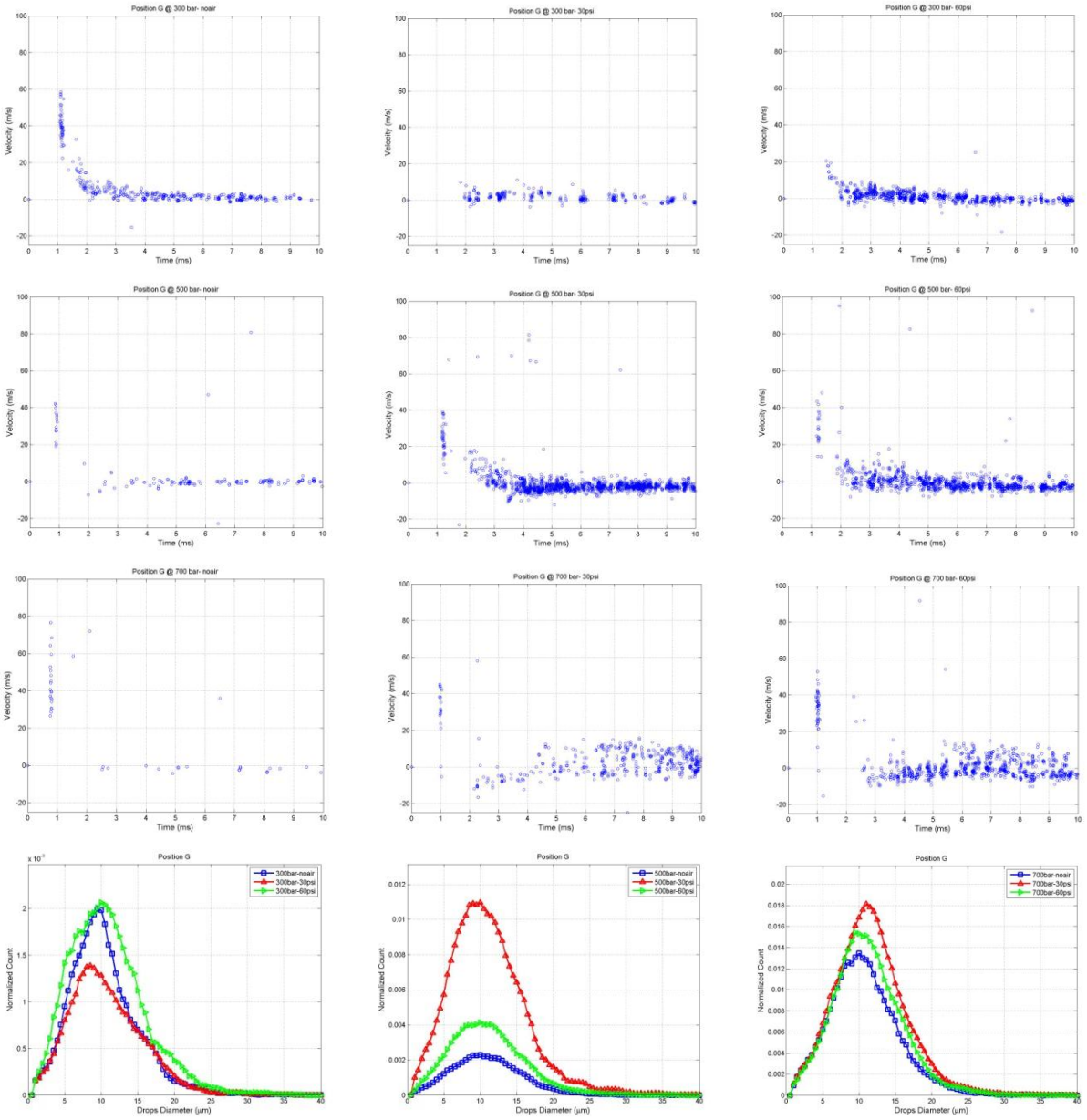

Figure 4.33 Position G (22-0-35) – Velocity and DropSize PDF at Pinj = 300 bar, 500 bar, 700 bar and Pair = 0 psi, 30 psi, 60 psi

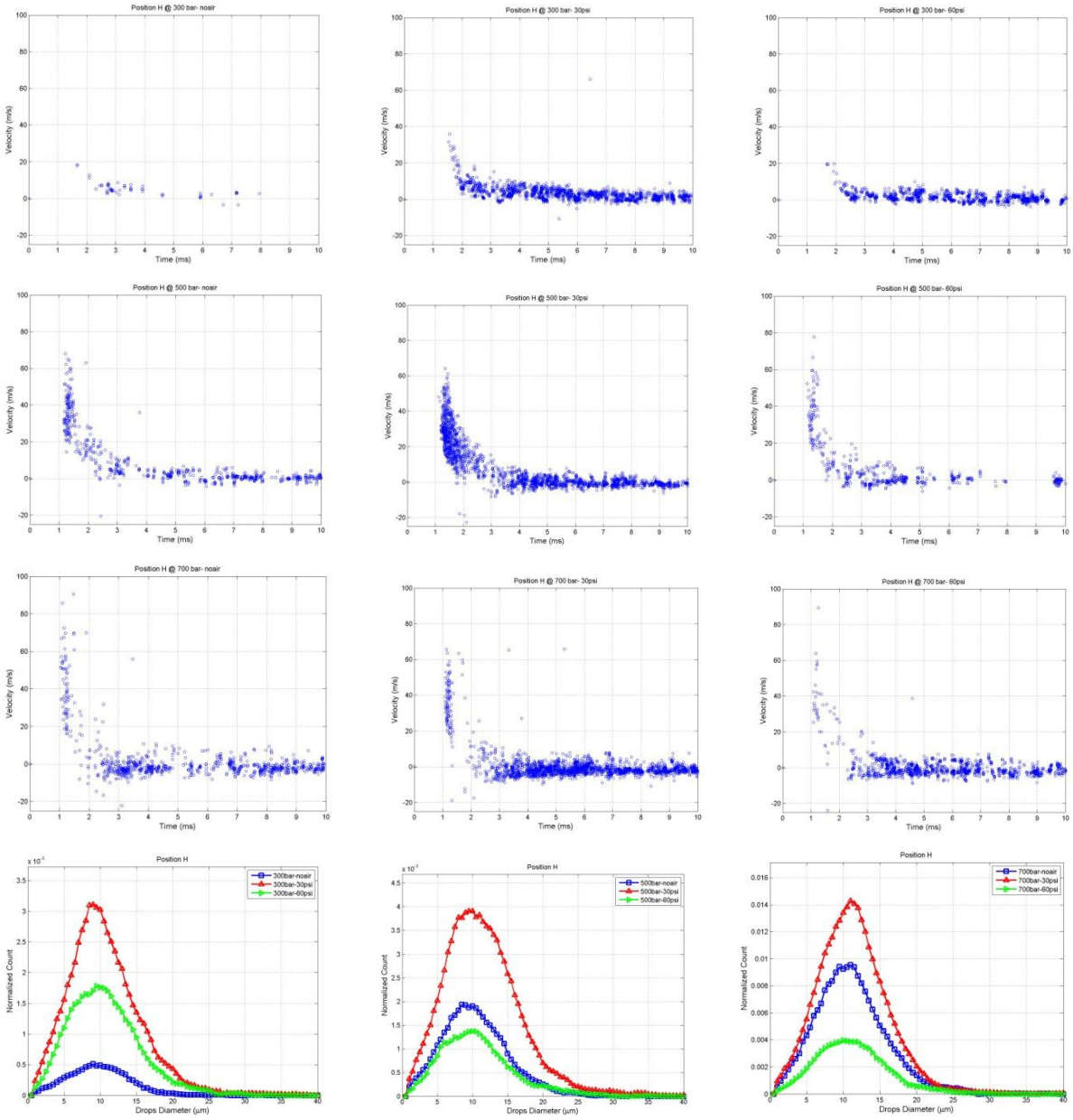

Figure 4.34 Position H (22-0-45) – Velocity and DropSize PDF at Pinj = 300 bar, 500 bar, 700 bar and Pair = 0 psi, 30 psi, 60 psi

References

1. Steven G. Chalk, James F. Miller, Fred W. Wagner, “Challenges for fuel cells in transport applications”, Journal of Power Sources 86 _2000. 40–51
2. Gaines L, Vyas A, Anderson J., “Estimation of fuel use by idling commercial trucks”, Transp Res Rec 2006;1983:91–8.
3. Inyong Kang, Joongmyeon Bae, “Autothermal reforming study of diesel for fuel cell application”, Journal of Power Sources 159 (2006) 1283–1290
4. Lim H. “Study of exhaust emissions from idling heavy-duty diesel trucks and commercially available idle-reducing devices.”, US Environmental Protection Agency, EPA420-R-02-025. Office of Air and Radiation, Ariel Rios Building, 1200 Pennsylvania Avenue, NW, Washington, DC, 2002.
5. Nicholas Lutsey, Christie-Joy Brodricka, Timothy Lipman, “Analysis of potential fuel consumption and emissions reductions from fuel cell auxiliary power units (APUs) in long-haul trucks”, Energy 32 (2007) 2428–2438.
6. André L. Boehman & Olivier Le Corre, “Combustion of Syngas in Internal Combustion Engines”, Combust. Sci. and Tech., 180: 1193–1206, 2008.
7. V. A. Kirillov, N. A. Kuzin, V. V. Kireenkov, Yu. I. Amosov, V. A. Burtsev, V. K. Emel’yanov, V. A. Sobyanin, and V. N. Parmon, “Use of Syngas as an Auto Fuel Additive: State of the Art and Prospects”. ISSN 0040_5795, Theoretical Foundations of Chemical Engineering, 2011, Vol. 45, No. 2, pp. 127–140.
8. Jia, M., Hou, D., Li, J., Xie, M., Liu, H., “A Micro-Variable Circular Orifice Fuel Injector for HCCI-Conventional Engine Combustion – Part I Numerical Simulation of Cavitation” SAE Technical Paper 2007-01-0249

9. Hou, D., Zhang, H., Kalish, Y., Lee, C., Cheng, W. “Adaptive PCCI Combustion Using Micro-Variable Circular-Orifice (MVCO) Fuel Injector – Key Enabling Technologies for High Efficiency Clean Diesel Engines” SAE Technical Paper 2009-01-1528
10. Hou, D., Li, J., Jia, M., Wang, Z., Shuai, S., Wang, J., “A Micro-Variable Circular Orifice (MVCO) Fuel Injector for Zoned Low Temperature Combustion” DOE 2006 DEER Conference, Detroit, Michigan, August 20-24.
11. Hou, D., A Mixed-Mode Fuel Injector with a Micro Variable Circular Orifice. PCT/IB2005/051474, 2005.
12. Hou, D., China Patent No. ZL 2005 10200039.9.
13. X. Karatzas, M. Nilsson, J. Dawody, B. Lindström, L. J. Pettersson, “Characterization and optimization of an autothermal diesel and jet fuel reformer for 5 kWe mobile fuel cell applications”. Chem. Eng. J. 156 (2010) 366-379.
14. Xanthias Karatzas, “Rhodium diesel-reforming catalysts for fuel cell applications”. Thesis, KTH – Royal Institute of Technology, Stockholm, Sweden 2011
15. D.-J. Liu, M. Krumpelt, H.-T. Chien, S.H. Sheen, “Catalysts and Fuel Mixing for Diesel Reformer in Fuel Cell Auxiliary Power Unit”. Argonne National Laboratory
16. Yolanda R. Hicks, Randy J. Locke, Chia H. Yen, “Optical Evaluation of Fuel Injection and Mixing Processes in a 10 kW Fuel Reformer”. AIAA 2006-2975
17. Kibum Kim, Jaewoo Chung, Kihyung Lee, wansoo Lee, “Investigation of the Swirl Effect on Diffusion Flame in a Direct-Injection (DI) Diesel Engine Using Image Processing Technology”. Energy & Fuels 2008, 22, 3687–3694

18. Yehia A. Eldrainy, Khalid M. Saqr, Hossam S. Aly, Tholudin Mat Lazim, Mohammad Nazri Mohd Jaafar, "Large eddy simulation and preliminary modeling of the flow downstream a variable geometry swirler for gas turbine combustors". International Communications in Heat and Mass Transfer 38 (2011) 1104–1109
19. A. Datta, "Influence of inlet flow conditions on the performance of a swirl-stabilized combustor burning liquid fuel spray". INTERNATIONAL JOURNAL OF ENERGY RESEARCH *Int. J. Energy Res*. 2000; 24:373, 390
20. Lou, Di-ming; Yang, Rang; Tan, Pi-qiang; Hu, Zhi-yuan; Yao, Di, "Performance and Emission Characteristics of Diesel Engine Fueled with Emulsified Diesel". Tongji University, Shanghai, China
21. B. Lindstro¨m, J.A.J. Karlsson, P. Ekdunge, L. De Verdier, B. Ha¨ggendal, J. Dawody, M. Nilsson, L.J. Pettersson, "Diesel fuel reformer for automotive fuel cell applications". International Journal of Hydrogen Energy, 34(2009)3367 – 3381
22. J. Benajes, R. Payri, S. Molina, V. Soare; "Investigation of the Influence of Injection Rate Shaping on the Spray Characteristics in a Diesel Common Rail System Equipped with a Piston Amplifier"; Transactions of the ASME, Vol. 127, November 2005.
23. Hongjun Xu, Kun Yang, Zhenming Liu, Dongjia Zhou; "Test Investigation of the Influence of Injection Rate Shaping on the Spray Characteristics in High-pressure Common Rail System"; The Ninth International Conference on Electronic Measurement & Instruments, 2009.
24. Amy Peterson, Shriram Subramaniyam, and Ming-Chia Lai, Optimization of Swirler-Venturi Mixer Geometry for Fuel Reformer Application, 3rd International Energy Conversion Engineering Conference, 2005.

25. Hyun Kyu Suh, Chang Sik Lee, “Effect of cavitation in nozzle orifice on the diesel fuel atomization characteristics”. International Journal of Heat and Fluid Flow 29 (2008) 1001–1009.
26. R. Payri, F.J. Salvador, J. Gimeno, J. de la Morena, “Effects of nozzle geometry on direct injection diesel engine combustion process”, Applied Thermal Engineering 29 (2009) 2051–2060.
27. F. Payri, J. M. Desantes, J. V. Pastor, “LDV measurements of the flow inside the combustion chamber of a 4-valve D.I. diesel engine with axisymmetric piston-bowls”, Experiments in Fluids 22 (1996) 118-128.
28. J. Benajes, R. Payri, S. Molina, V. Soare, “Investigation of the Influence of Injection Rate Shaping on the Spray Characteristics in a Diesel Common Rail System Equipped with a Piston Amplifier”, Transactions of the ASME, Vol. 127, NOVEMBER 2005.
29. Rangshu Xu, Rui Lin, SuoGang Zhang, Tingchu Zhou, Minli Bai, “Numerical Simulation of Spray Process of Fuel Nozzle”, Advanced Materials Research Vols. 308-310 (2011) pp 47-52.
30. Dennis L. Siebers, “Scaling Liquid-Phase Fuel Penetration in Diesel Sprays Based on Mixing-Limited Vaporization”, SAE TECHNICAL PAPER SERIES 1999-01-0528.
31. F. Payri, V. Bermu´dez, R. Payri, F.J. Salvador, “The influence of cavitation on the internal flow and the spray characteristics in diesel injection nozzles”, Fuel 83 (2004) 419–431.
32. J. Kostas, D. Honnery, J. Soria, “Time resolved measurements of the initial stages of fuel spray penetration”, Fuel 88 (2009) 2225–2237.

33. Kibum Kim, Jaewoo Chung, Kihyung Lee, and Kwansoo Lee, "Investigation of the Swirl Effect on Diffusion Flame in a Direct-Injection (DI) Diesel Engine Using Image Processing Technology, *Energy & Fuels* **2008,** *22,* 3687–3694.
34. Xanthias Karatzasa, Kjell Janssonb, Jazaer Dawodyc, Roberto Lanzaa, Lars J. Petterssona, "Microemulsion and incipient wetness prepared Rh-based catalyst for diesel reforming", Catalysis Today 175 (2011) 515– 523.
35. Daniel R. Palo, Robert A. Dagle and Jamie D. Holladay, "Methanol Steam Reforming for Hydrogen Production, Chem. Rev. **2007,** 107, 3992-4021.
36. A. Cutillo, S. Specchia, M. Antonini, G. Saracco, V. Specchia, "Diesel fuel processor for PEM fuel cells: Two possible alternatives (ATR versus SR)", Journal of Power Sources 154 (2006) 379–385.
37. Chien-Pei Mao, John Short, Phil Buelow Mark Caples, Randy Siders and Derrick Clausen, "Innovative Injection and Mixing Systems for Diesel Fuel Reforming", SECA 6th Annual Workshop, Pacific Grove, California, 2005.
38. J. M. Meacham, M. J. Varady, F. L. Degertekin, and A. G. Fedorov, "Droplet formation and ejection from a micromachined ultrasonic droplet generator: Visualization and scaling", Phys. Fluids 17, 100605 (2005)
39. C. Ayrault, J.-S. Chang, G.D. Harvel, D. Ewing, H. Hirata and S. Matsumoto, "Reforming of Diesel Fuel by a Recirculation type Pulsed Voltage Electrohydrodynamic Atomization", 2011 IEEE International Conference on Dielectric Liquids
40. Inyong Kang, Joongmyeon Bae, Sangho Yoon, Youngsung Yoo, Performance improvement of diesel autothermal reformer by applying ultrasonic injector for effective fuel delivery", Journal of Power Sources 172 (2007) 845–852

41. Mark J. Varady and Andrei G. Fedorov, “Fuel Reformation and Hydrogen Generation with Direct Droplet Impingement Reactors: Model Formulation and Validation”, Ind. Eng. Chem. Res. 2011, 50, 9502–9513
42. R. Kapulla, S.B. Najera, “Operation conditions of a phase Doppler anemometer: drop size measurements with laser beam power, photomultiplier voltage, signal gain and signal-to-noise ratio as parameters”, Meas. Sci. Tech. Vol. 17 (2006), 221-227
43. Seoksu Moon, Yuhei Matsumoto, Keiya Nishida, Jian Gao; “Gas entrainment characteristics of diesel spray injected by a group-hole nozzle”; Fuel 89 (2010) 3287-3299.
44. Su Han Park, Hyung Jun Kim, Chang Sik Lee; “Macroscopic spray characteristics and breakup performance of dimethyl ether (DME) fuel at high fuel temperatures and ambient conditions”; Fuel 89 (2010) 3001-3011.
45. N Mitroglou, J M Nouri, M Gavaises, C Arcoumanis; “Spray Characteristics of a multi-hole injector for direct-injection gasoline engines”; Int. J. Engine Res. Vol. 7 (IMechE 2006).
46. R. J. H. Klein-Douwel, P. J. M. Frijters, L. M. T. Somers, W. A. de Boer, R. S. G. Baert; “Macroscopic diesel fuel spray shadowgraphy using high speed digital imaging in a high pressure cell”; Fuel 86 (2007) 1994-2007.
47. Sazhin SS, Feng G, Heikal MR; “A model for fuel spray penetration”; Fuel 2001;80:2171–80.
48. Desantes JM, Payri R, Salvador FJ, Gil A.; “Development and validation of a theoretical model for diesel spray penetration”, Fuel 85 (2006) 910–917.

49. Delacourt E, Desmet B, Besson B.; “Characterisation of very high pressure diesel sprays using digital imaging techniques”, Fuel 84 (2005) 859–867.

50. Z. Liu, R. D. Reitz; “An Analysis of the distortion and breakup mechanism of high speed liquid drops”, Int. J. Multiphase Flow (1997) Vol. 23, No. 4 pp. 631-650.